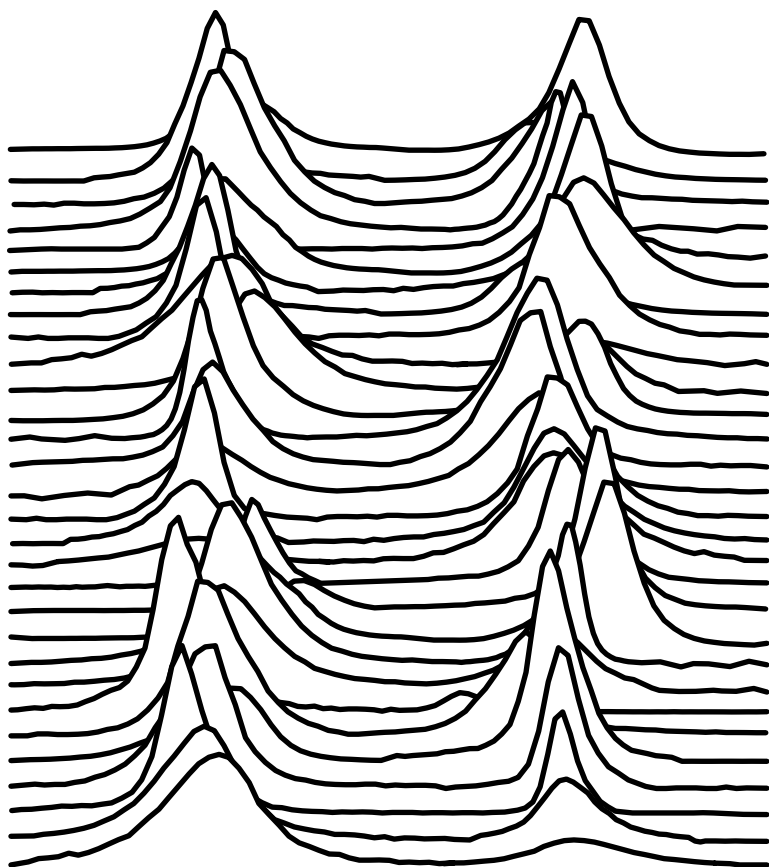


SPIN-WAVE DYNAMICS DRIVEN BY SPIN-ORBIT TORQUE



BORIS DIVINSKIY
MÜNSTER
2020

Angewandte Physik

Spin-wave dynamics driven by spin-orbit torque

Inaugural-Dissertation
zur Erlangung des Doktorgrades
der Naturwissenschaften im Fachbereich Physik
der Mathematisch-Naturwissenschaftlichen Fakultät
der Westfälischen Wilhelms-Universität Münster

vorgelegt von
Boris Divinskiy
aus Gelendschik, Russland
2020

Dekan: Prof. Dr. Michael Rohlfing
Erster Gutachter: Prof. Dr. Sergej O. Demokritov
Zweiter Gutachter: Prof. Dr. Carsten Fallnich
Tag der mündlichen Prüfung:
Tag der Promotion:

Abstract

Magnonics is an emerging subfield of modern magnetism that investigates spin waves (magnons) in terms of their potential applications as nanoscale signal carriers. Magnonics has made significant progress over the past decade. Nevertheless, there are still several major obstacles hindering the implementation of technologically competitive magnonic devices. First, the existing spin wave excitation methods are characterized by low energy efficiency at the nanoscale. Second, spin waves propagating in thin magnetic films experience large propagation losses. The advent of spin-orbit torque (SOT) phenomena has opened new horizons for magnonics, since SOT provides the means to overcome the described obstacles. However, recent intense studies of SOT have revealed new unexpected difficulties and challenges associated with the emergence of complex nonlinear processes in nonequilibrium magnetic systems. This thesis is devoted to finding routes to resolve these issues limiting the progress in the field of SOT-driven magnonics. The obtained results are expected to accelerate new developments in this field and enable the implementation of spin-wave-based devices that will be more attractive for real-world applications.

Zusammenfassung

Die Magnonik ist neu entstehendes Teilgebiet des modernen Magnetismus, die Spinwellen (Magnonen) im Hinblick auf ihre möglichen Anwendungen als nanoskalige Signalträger untersucht. Die Magnonik weist einige bedeutende Fortschritte über das letzte Jahrzehnt auf. Dennoch gibt es immer noch einige große Hindernisse, die die Implementierung der technologisch wettbewerbsfähigen Magnonik-Geräten behindern. Erstens zeichnen sich die existierende Spinwellen-Anregungsmethoden durch eine geringe Energieeffizienz im Nanobereich aus. Zweitens weisen Spinwellen, die sich in dünnen magnetischen Filmen ausbreiten, große Ausbreitungsverluste auf. Die Entdeckung des Phänomens des Spin-Bahn-Drehmoments (SBD) hat der Magnonik neue Horizonte eröffnet, da die Benutzung der SBD-Phänomene das Mittel zur Überwindung der beschriebenen Hindernisse bietet. Jüngste intensive Studien zu SBD haben jedoch neue unerwartete Schwierigkeiten und Herausforderungen aufgezeigt, die mit der Entstehung komplexer nichtlinearer Prozesse in Nichtgleichgewichts-Magnetsystemen verbunden sind. Diese Arbeit widmet sich der Suche nach Wegen zur Lösung dieser Probleme, die den Fortschritt auf dem Gebiet der SBD-gesteuerten Magnonik einschränken. Die erzielten Ergebnisse sollen neue Entwicklungen auf diesem Gebiet beschleunigen und die Implementierung von Spinwellen-basierten Geräten ermöglichen, die für technologisch-relevanten Anwendungen attraktiver sind.

Contents

1	Introduction	1
2	Background	4
2.1	Magnetization dynamics in ferromagnets	4
2.2	Spin waves in extended thin films	8
2.3	Spin waves in waveguides	11
2.3.1	Longitudinally magnetized waveguide	11
2.3.2	Transversally magnetized waveguide	12
2.4	Magnons	13
2.5	Nonlinear magnetization dynamics	14
2.5.1	Nonlinear frequency shift	15
2.5.2	Nonlinear damping	16
2.6	Spin Hall effect	17
2.7	Spin-orbit torque	18
2.8	SOT oscillators	20
3	Methods	23
3.1	Brillouin light scattering spectroscopy	23
3.1.1	Principles of BLS	23
3.1.2	Micro-focus BLS	26
3.2	Micromagnetic simulations	28
4	Effects of the SOT on a magnon gas	29
4.1	Spectral and thermodynamic characteristics of a magnon gas driven by the SOT	29
4.1.1	Motivation	29
4.1.2	Studied system	30
4.1.3	Results and discussion	31
4.1.4	Conclusions	37
4.2	Instability of SOT-driven magnon condensates	37
4.2.1	Motivation	37

4.2.2	Studied system	38
4.2.3	Results and discussion	39
4.2.4	Conclusions	42
5	Tailored PMA as a way to control nonlinear damping	44
5.1	Case of large PMA	44
5.1.1	Motivation	44
5.1.2	Studied system	45
5.1.3	Results and discussion	47
5.1.4	Conclusions	53
5.2	Case of moderate PMA comparable with the dipolar anisotropy	54
5.2.1	Motivation	54
5.2.2	Studied system	54
5.2.3	Results and discussion	55
5.2.4	Conclusions	60
6	Excitation and amplification of spin waves by the SOT	61
6.1	Motivation	61
6.2	Studied system	61
6.3	Results and discussion	62
6.4	Conclusions	67
7	Summary and outlook	68
References		71
List of publications		88
Acknowledgment		89
Lebenslauf		90

Commonly used acronyms

Notation in text	Meaning
SOT	Spin-orbit torque
SHE	Spin-Hall effect
PMA	Perpendicular magnetic anisotropy
LLG	Landau-Lifshitz-Gilbert equation
FMR	Ferromagnetic resonance
BEC	Bose-Einstein condensation
BLS	Brillouin light scattering
Py	Permaloy ($\text{Ni}_{80}\text{Fe}_{20}$)
CoNi	Cobalt-nickel multilayer

Commonly used symbols

Notation in text	Meaning
\mathbf{H}	Magnetic field
\mathbf{M}	Magnetization
\mathbf{m}	Dynamic magnetization
M_s	Saturation magnetization
f	Frequency
\mathbf{k}	Wavevector
I	Current
I_C	Critical current
α	Gilbert damping

The CGS (Gaussian) units for magnetic properties are used throughout the thesis.

Chapter 1

Introduction

Spin waves - or their quanta called magnons - are the lowest-energy collective excitations above the ground state of magnetically ordered materials [1, 2]. From a semi-classical point of view, a spin wave can be visualized as a phase-coherent precession of spins that propagates through the magnetic medium in a form of a wave (Figures 1.1(a) and (b)) [3]. The existence of such waves was predicted by Bloch in 1930 [4]. Ferromagnetic resonance, discovered by Griffiths in 1946 [5], was the first direct observation of spin waves and served as the starting point for the experimental studies of these waves. Research in this area was particularly intense in the 60s-80s and led to the development of a wide range of spin-wave-based devices for analogue signal processing that found applications in many areas of microwave technologies [6–10].

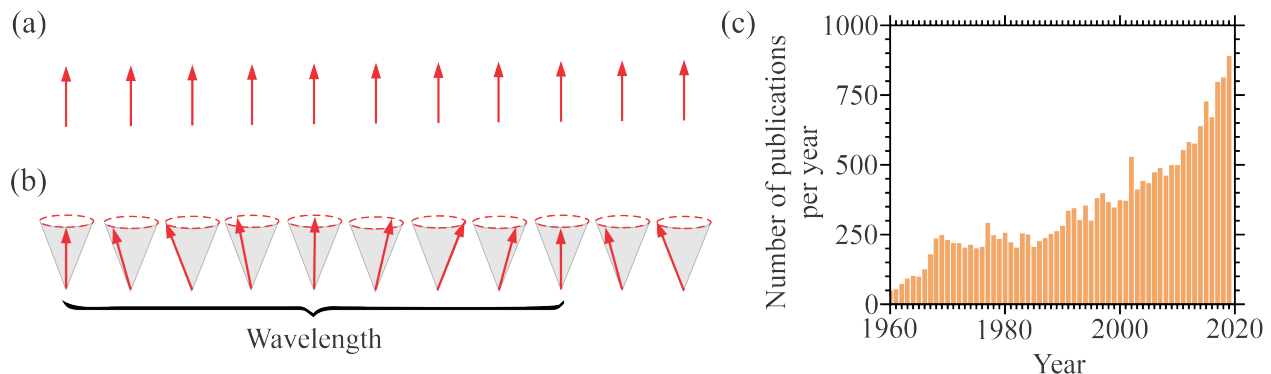


Figure 1.1 (a) In the ground state of a ferromagnet, all spin are parallel. (b) The lowest-energy excitations above the ground state are spin waves (magnons). (c) Evolution of the number of publications per year with the keywords "spin waves" and "magnons".

However, interest in spin waves does not diminish over time, but only grows both within the scientific community and industry (Figure 1.1(c)). Nowadays, spin waves are considered as potential data carriers in novel computing devices as an alternative to electrons in conventional microelectronics [11, 12]. The main advantages offered by spin waves are:

- **Wave-based computing** Information can be encoded not only in the amplitude, but also in the phase of a spin wave, which provides an additional degree of freedom in data processing and paves the way for non-conventional, non-Boolean computing algorithms [13].
- **Wide frequency range** The maximum clock rate of a computing element is determined by the wave frequency. Typically, spin wave spectrum starts at GHz frequencies, which are used in modern communication technologies, and extends into the very promising THz range [14–16].
- **Short wavelengths** The wavelength of the used wave defines the minimum size of a wave-based computing device. Despite microwave frequencies, spin waves have very short wavelengths down to a few nanometers [17–20].
- **Tunability** Spin wave characteristics can be tuned on a broad scale by a choice of the magnetic material, the direction and strength of the external magnetic field, the geometry of the sample, etc. [21]
- **Nonlinearity** There exists a great variety of nonlinear spin-wave effects [22–25], which provide additional opportunities for data processing.

The emerging field of science that aims to utilize spin waves to transmit and process information at the nanoscale is known as magnonics [26–31]. Many building blocks of spin-wave circuitry have already been proposed and experimentally demonstrated: spin-wave logic gates [32–35] and majority gates [36,37], a magnon transistor [38], magnonic directional couplers [39–41] and units for beyond-Moore computing [42–45], just to name a few.

Despite the fact that the demonstrated magnonic devices benefit from numerous advantages provided by spin waves, they suffer from two major drawbacks. The first Achilles heel is the lack of an energy efficient method for excitation of spin waves on the nanoscale [13]. In conventional macroscopic-scale devices, spin waves are created by microwave fields produced by microstrip or coplanar waveguides [46,47]. However, reducing the size of the spin-wave antenna inevitably leads to large conversion losses, which makes the traditional inductive mechanism very inefficient [13,48]. The second drawback is associated with the fact that nanoscale magnetic systems are characterized by relatively large magnetic damping [49,50]. As a consequence, spin wave propagating in nanometer-thick films have short decay lengths, which imposes limitations on the functionality of magnonic nanosystems.

To bring magnonic devices closer to the real-world technical applications, one needs to find a way to overcome these drawbacks. At the moment, the most promising approach is based on the utilization of the so-called spin-orbit torque (SOT) [51–53]. The SOT provides the ability to reduce magnetic damping in spatially extended regions [54], which may enable decay-free

propagation of spin waves in magnetic nanosystems. Moreover, the SOT can completely compensates magnetic damping, resulting in the onset of magnetic auto-oscillations [55], which can be used for the high-efficiency generation of coherent propagating spin waves on the nanoscale.

Since the SOT phenomenon has the potential to address the main challenges associated with the downscaling of magnonic devices, it has become the subject of intense research in the recent years [54–67]. Several important milestones have already been achieved, including the implementation of SOT-driven nano-oscillators [68, 69] and a nearly tenfold increase in the spin-wave decay length by using the SOT [70]. However, despite significant progress, there are still many challenges and open questions in the field of SOT-driven magnonics [71]. Among them are:

- *Which magnons are predominantly affected by the SOT?*
- *Is it possible to eliminate detrimental nonlinear effects?*
- *How can one convert spatially localized auto-oscillations into propagating spin waves?*

These questions are of crucial importance for the further developments in spin-orbit-torque magnonics, and this thesis is devoted to finding answers to them.

Chapter 2

Background

2.1 Magnetization dynamics in ferromagnets

Fundamentally, ferromagnetic materials contain atoms with net magnetic moments $\boldsymbol{\mu}$ that strongly interact with each other. However, to describe dynamical processes in such materials, it is convenient to ignore the atomic nature of matter and characterize the state of the ferromagnet by a continuous vector field. The vector field is called the magnetization \mathbf{M} and is defined as the magnetic moment per unit volume

$$\mathbf{M} = \frac{\sum_{\delta V} \boldsymbol{\mu}}{\delta V},$$

where $\sum_{\delta V} \boldsymbol{\mu}$ is the total magnetic moment of a mesoscopic volume δV . The length of the magnetization vector \mathbf{M} is assumed to be constant thorough the material and is called the saturation magnetization M_s . The described continuum approach is referred to as micromagnetism [72]. The micromagnetic theory has two main limitations of its applicability. First, it is valid only when the characteristic scale of the investigated dynamic processes is much larger than the interatomic distances. Second, the temperature of the ferromagnet should be far below a certain critical temperature, called the Curie temperature T_C , at which thermal fluctuations completely destroy the magnetic order. The experiments presented in Chapters 4-6 were performed at room temperature $T_0 = 295$ K with two ferromagnetic materials: a nickel-iron alloy $\text{Ni}_{80}\text{Fe}_{20}$ known as permalloy (Py) and cobalt-nickel multilayers, which we will refer to as CoNi. Since both Py and CoNi have Curie temperatures that are well above T_0 , the micromagnetic approach is a good approximation for describing magnetization dynamics in these materials at room temperature.

Within the micromagnetic framework, the dynamics of the magnetization vector are governed by the phenomenological Landau-Lifshitz-Gilbert (LLG) equation [1]

$$\frac{d\mathbf{M}}{dt} = \underbrace{-\gamma(\mathbf{M} \times \mathbf{H}_{\text{eff}})}_{\text{precession}} + \underbrace{\frac{\alpha}{M_s}(\mathbf{M} \times \frac{d\mathbf{M}}{dt})}_{\text{damping}}, \quad (2.1)$$

where γ is the absolute value of the gyromagnetic ratio for the electron spin ($\gamma/2\pi = 2.8 \text{ MHz/Oe}$) and \mathbf{H}_{eff} is the effective magnetic field, which is discussed in detail below. In equilibrium, the magnetization is parallel to the effective magnetic field.¹ However, when the magnetization deviates from the equilibrium position (e.g., due to an external perturbation), it starts to precess around the effective magnetic field, as described by the first term in the right hand side of the LLG equation. This precessional motion of magnetization can be regarded as an analogue of the well-known Larmor precession of a free magnetic moment around an external magnetic field [73]. The second term of the LLG equation, which is referred to as the Gilbert torque [74], describes the relaxation of the magnetization to the equilibrium position and represents the dissipation of energy of magnetization oscillations. The physical mechanisms that determine the transfer of energy of magnetic oscillations to the lattice are numerous and rather complicated [75]. However, in many cases they can be described reasonably well by the Gilbert torque with a single damping parameter α called the Gilbert constant. The combined effect of the precessional and damping torques causes the magnetization to spiral towards the equilibrium position, as shown in Figure 2.1.

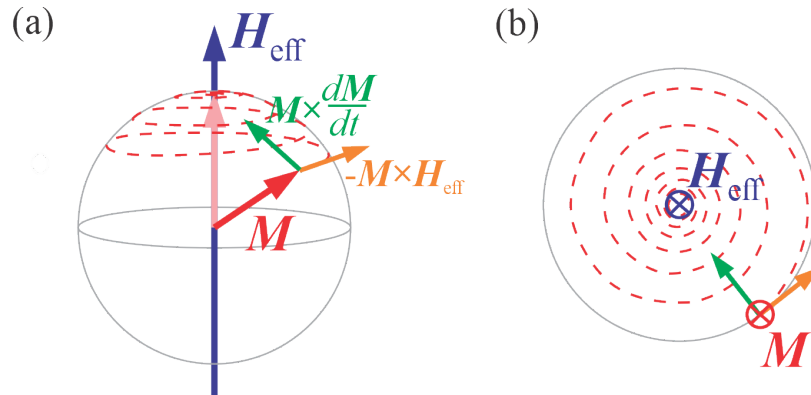


Figure 2.1 (a) Trajectory of the magnetization \mathbf{M} about the effective magnetic field \mathbf{H}_{eff} , with the drawn directions of the precessional and damping torques. Light red arrow shows the equilibrium position of the magnetization ($\mathbf{M} \parallel \mathbf{H}_{\text{eff}}$). (b) Top view of the dynamics.

The effective magnetic field \mathbf{H}_{eff} is the sum of all effective fields due to magnetic interactions existing in a specific system. In general, \mathbf{H}_{eff} depends on the magnetization \mathbf{M} and is defined as

$$\mathbf{H}_{\text{eff}}(\mathbf{M}) = -\frac{\partial E(\mathbf{M})}{\partial \mathbf{M}}, \quad (2.2)$$

¹The second term on the right-hand side of the LLG equation $\mathbf{M} \times \frac{d\mathbf{M}}{dt}$ can be rewritten as $\mathbf{M} \times (\mathbf{M} \times \mathbf{H}_{\text{eff}})$ [1]. Therefore, when $\mathbf{M} \parallel \mathbf{H}_{\text{eff}}$, both terms on the right side of Equation (2.1) are zero and the magnetization is in the equilibrium position, since no torque is exerted on it.

where $E(\mathbf{M})$ is the total magnetic energy density [1]. The most important contributions to $E(\mathbf{M})$ are:

Zeeman energy The Zeeman term describes the interaction between the external magnetic field \mathbf{H}_0 and the magnetization. The Zeeman energy density is given by

$$E_Z = -\mathbf{M} \cdot \mathbf{H}_0. \quad (2.3)$$

To minimize E_Z , the magnetization tends to align along the external magnetic field.

Dipolar energy In addition to the external magnetic field, the magnetic moments constituting the ferromagnet create their own magnetic fields. The dipolar field arising from an individual moment $\boldsymbol{\mu}_i$ is

$$\mathbf{H}_{\text{dip},i} = \frac{3(\mathbf{r} \cdot \boldsymbol{\mu}_i)\mathbf{r}}{r^5} - \frac{\boldsymbol{\mu}_i}{r^3},$$

where r is the distance to $\boldsymbol{\mu}_i$ [73]. Thus, the total energy density associated with the dipole-dipole interaction between magnetic moments of the sample can be expressed by

$$E_{\text{dip}} = -\sum_{i \neq j} \mathbf{H}_{\text{dip},i} \cdot \boldsymbol{\mu}_j = -\sum_{i \neq j} \left(\frac{3(\mathbf{r}_{ij} \cdot \boldsymbol{\mu}_i)(\mathbf{r}_{ij} \cdot \boldsymbol{\mu}_j)}{r_{ij}^5} - \frac{(\boldsymbol{\mu}_i \cdot \boldsymbol{\mu}_j)}{r_{ij}^3} \right). \quad (2.4)$$

As can be seen from Equation 2.4, the dipole-dipole interaction is a long-range interaction, since E_{dip} decreases with distance as $1/r_{ij}^3$. Moreover, this interaction is anisotropic, because E_{dip} depends not only on the distance separating two moments, but also on the their orientation relative to a vector connecting them \mathbf{r}_{ij} .

In a uniformly magnetized and infinite sample, magnetic fields produced by all magnetic moments in a ferromagnetic body compensate each other and therefore the total static dipolar field is zero. However, if a sample is finite or the magnetization distribution is nonuniform, the discontinuity of the magnetization results in a non-zero dipolar field. This field can be viewed as arising from fictitious magnetic charges at the surfaces of the sample (Figure 2.2). The dipolar field inside the sample is called the demagnetizing field \mathbf{H}_{dem} , whereas the field outside is called the stray field \mathbf{H}_s . These fields can be found by solving the Maxwell's equation. In case of a ferromagnetic ellipsoid (note that an infinitely extended film is the limiting case of an ellipsoid), the demagnetizing field can be expressed by a simple analytical formula

$$\mathbf{H}_{\text{dem}} = -\overset{\leftrightarrow}{N}\mathbf{M}, \quad (2.5)$$

where $\overset{\leftrightarrow}{N}$ is the demagnetizing tensor [1]. As follows from Equation 2.5, \mathbf{H}_{dem} is oriented opposite to the magnetization \mathbf{M} , trying to suppress the overall magnetization of the system. An important consequence of this fact is that for ferromagnetic films the dipolar energy is minimized for the magnetization directed in the plane of the film. This tendency of the magnetization to be in-plane is called the dipolar or shape anisotropy.

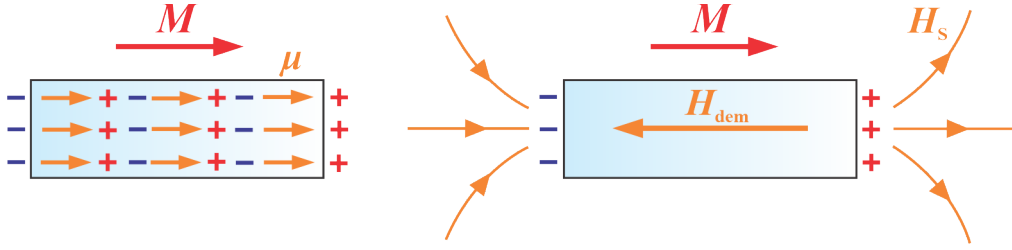


Figure 2.2 In analogy with an electric dipole, a magnetic moment μ can be imagined as a pair of opposing charges. Inside the ferromagnetic body these fictitious magnetic charges compensate each other. However, uncompensated magnetic charges exist on the surfaces of the ferromagnetic sample and produce the dipolar field. The dipolar field inside the sample is called the demagnetizing field \mathbf{H}_{dem} because it is directed opposite to the magnetization \mathbf{M} . The field outside the sample is called the stray field \mathbf{H}_s and it loops around in space.

Exchange energy The exchange interaction is a quantum mechanical phenomena that is responsible for the magnetic ordering of ferromagnetic materials, as it favors the parallel alignment of neighboring magnetic moments. Loosely speaking, the exchange interaction originates from the Pauli exclusion principle and the electrostatic Coulomb interaction [3]. In the micromagnetic approximation, the exchange energy density can be written as

$$E_{\text{exch}} = \frac{A_{\text{ex}}}{4\pi M_s^2} [(\nabla M_x)^2 + (\nabla M_y)^2 + (\nabla M_z)^2], \quad (2.6)$$

where A_{ex} is the exchange stiffness constant, which is a positive quantity for ferromagnets [72]. Therefore, the exchange energy is minimum when the magnetization is uniform within ferromagnetic materials (all the derivatives in Equation 2.6 vanish). The corresponding effective field is

$$\mathbf{H}_{\text{exch}} = \frac{A_{\text{ex}}}{2\pi M_s^2} \nabla^2 \mathbf{M} = l_{\text{ex}}^2 \nabla^2 \mathbf{M}.$$

Here, $l_{\text{ex}} = \sqrt{A_{\text{ex}}/2\pi M_s^2}$ is the exchange length. The exchange length is the characteristic scale on which the exchange interaction is dominant, and the magnetization is uniform. Typically, l_{ex} does not exceed ten nanometers (e.g., $l_{\text{ex}} \approx 5 \text{ nm}$ for Py [76]), which reflects the fact that the exchange interaction is an inherently short range interaction unlike the dipolar interaction. At length scales larger than l_{ex} , the dipolar interaction dominates and the sample can be divided into magnetic domains with different magnetization orientations.

Anisotropy energy In the presence of magnetic anisotropy, the magnetization tends to orient along a certain preferred direction. There are many physical mechanisms that may result in the magnetic anisotropy. For example, as mentioned above, the dipole-dipole interaction results in the shape anisotropy in ferromagnetic films. Apart from the shape anisotropy, in certain sandwich structures, which consists of alternating magnetic layers of subnanometer thickness (such as CoNi studied in this thesis), surfaces and interfaces may induce the so-called perpendicular magnetic anisotropy (PMA). The PMA energy density

can be represented phenomenologically by

$$E_{\text{PMA}} = -\frac{K_a}{M_s^2}(\mathbf{e} \cdot \mathbf{M})^2,$$

where $K_a > 0$ is the anisotropy constant, and \mathbf{e} is the unit vector normal to the film plane [73]. Clearly, E_{PMA} is minimized when the magnetization aligns along the surface normal. The effective anisotropy field is

$$\mathbf{H}_{\text{PMA}} = \tilde{H}_a(\mathbf{e} \cdot \mathbf{M})\mathbf{e}, \quad (2.7)$$

where $\tilde{H}_a = \frac{2K_a}{M_s^2}$. Note that, in multilayer systems with PMA, there is a competition between the shape anisotropy and PMA. If PMA is larger than the shape anisotropy, the magnetization is oriented out-of-plane. Otherwise, the magnetization lies in-plane due to the dominance of the shape anisotropy.

Thus, the total total effective field $\mathbf{H}_{\text{eff}}(\mathbf{M})$ in Equation 2.1 can be written in the form

$$\mathbf{H}_{\text{eff}}(\mathbf{M}) = \mathbf{H}_0 + \mathbf{H}_{\text{dip}} + \mathbf{H}_{\text{exch}} + \mathbf{H}_{\text{PMA}} = \mathbf{H}_0 - \overset{\leftrightarrow}{N}\mathbf{M} + l_{\text{ex}}^2 \nabla^2 \mathbf{M} + \tilde{H}_a(\mathbf{e} \cdot \mathbf{M})\mathbf{e}.$$

There are many other magnetic interactions (e.g., the Dzyaloschinskii-Moriya interaction, the magnetoelastic interaction, etc.) that can also contribute to \mathbf{H}_{eff} . However, we do not consider them, since they are not relevant to the systems studied in this thesis.

2.2 Spin waves in extended thin films

In the framework of the continuum approach described above, spin waves are regarded as wave-like solutions of the LLG equation. Since spin waves are usually studied in thin magnetic films, let us consider an infinitely extended ferromagnetic film with PMA of a thickness d (Figure 2.2(a)). The film is magnetized to saturation by the in-plane external magnetic field \mathbf{H}_0 . We seek the solution of the LLG equation in the form

$$\mathbf{M}(\mathbf{r}, t) = M_z \mathbf{e}_z + \mathbf{m}(\mathbf{r}, t),$$

where M_z is the component directed along the external magnetic field \mathbf{H}_0 , and $\mathbf{m}(\mathbf{r}, t) \propto \exp[i(2\pi f(\mathbf{k})t - \mathbf{k} \cdot \mathbf{r})]$ is the so-called dynamical magnetization that is assumed to be of plane-wave form. The dispersion function $f(\mathbf{k})$ relates the spin-wave frequency to the wavevector. Knowing the spin-wave dispersion is of crucial importance because it determines many properties of spin waves. For example, the group velocity of spin waves, which represents the direction and velocity of the spin-wave energy flow, is defined as the gradient of the dispersion function $\mathbf{v}_g(\mathbf{k}) = 2\pi \nabla_{\mathbf{k}} f(\mathbf{k})$.

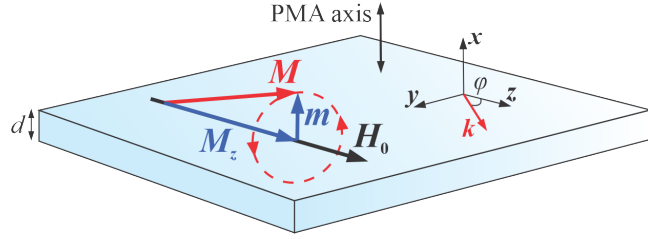


Figure 2.3 Schematic of an infinitely extended film with PMA of a thickness d . The in-plane external magnetic field \mathbf{H}_0 and the static components of the magnetization M_z are aligned parallel to the z -axis; \mathbf{m} is the dynamic magnetization. Note that, in general case, the magnetization precession trajectory is elliptical. The angle between the spin-wave wavevector \mathbf{k} and \mathbf{H}_0 is φ .

Because the effective field \mathbf{H}_{eff} is a function of \mathbf{M} and the product of these quantities appears in the right-hand side part of Equation 2.1, the LLG equation is an inherently non-linear equation. Therefore, as a rule, it is not possible to find a simple analytical formula for $f(\mathbf{k})$. However, if one assumes that the angle of magnetization precession is small, i.e., $||\mathbf{m}|| \ll M_z \approx M_s$, Equation 2.1 can be linearized by neglecting the terms quadratic in \mathbf{m} . In this case, the dispersion relation can be found by solving the system of equations consisting of the linearized LLG equation, Maxwell equations and proper boundary conditions. Since the involved math is quite tedious, we omit the details of derivation and present only the final result for the spin-wave dispersion in an in-plane magnetized extended film [77–79]

$$f(k) = \gamma/2\pi\sqrt{(H_0 + 4\pi M_s l_{\text{ex}}^2 k^2)(H_0 + 4\pi M_s l_{\text{ex}}^2 k^2 + 4\pi M_s(F - F^a))} \quad (2.8)$$

with

$$\begin{aligned} F &= 1 - P \cos^2 \varphi + 4\pi M_s \frac{P(1 - P) \sin^2 \varphi}{H_0 + 4\pi M_s l_{\text{ex}}^2 k^2}, \\ F^a &= \tilde{H}_a (1 + \frac{P 4\pi M_s \sin^2 \varphi}{H_0 + 4\pi M_s l_{\text{ex}}^2 k^2}), \\ P &= 1 - \frac{1 - \exp(-kd)}{kd}, \end{aligned}$$

where $k = \sqrt{k_x^2 + k_y^2}$, and φ is the angle between the wavevector \mathbf{k} and the direction of the external magnetic field \mathbf{H}_0 . We note that Equation 2.8 is valid under two conditions: the spin-wave wavelength is much larger than the thickness of the film (i.e., $kd \ll 1$) and the distribution of the dynamic magnetization across the film thickness is uniform.

A representative spin wave dispersion for a Py film is shown in Figure 2.4. The spectrum was calculated by using Equation 2.8 with the following parameters: $d = 5 \text{ nm}$, $4\pi M_s = 10 \text{ kG}$, $l_{\text{ex}} = 5 \text{ nm}$, $H_0 = 1000 \text{ Oe}$, and $\tilde{H}_a = 0$ because usually Py films do not exhibit PMA. Curves in Figure 2.4 are two limiting cases: $\mathbf{k} \parallel \mathbf{H}_0$ (corresponds to $\varphi = 0$ in Equation 2.8) and $\mathbf{k} \parallel \mathbf{H}_0$ ($\varphi = 90^\circ$). The shaded area is the spin-wave manifold corresponding to the intermediate values of $\varphi \in (0, 90^\circ)$. Spin waves propagating perpendicular to the direction of

the external field are usually referred to as the Damon-Eshbach (DE) waves [80]. Spin waves propagating along \mathbf{H}_0 are called Backward-Volume (BV) waves [1], as they can have negative group velocities because of the negative slope of their dispersion curves at small wavevectors (Figure 2.4(b)).

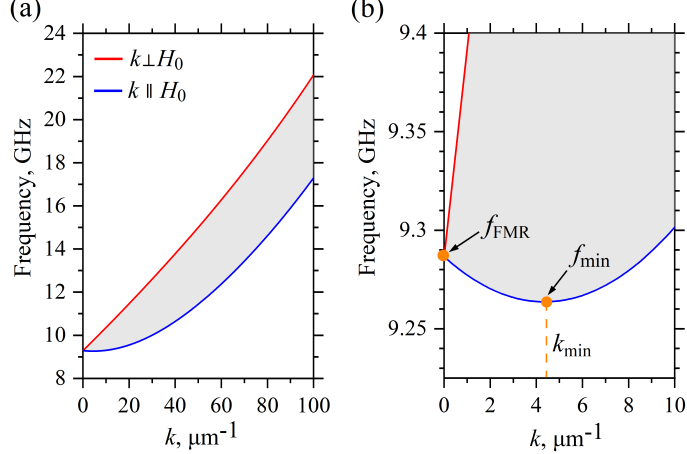


Figure 2.4 (a) Spin-wave spectrum for a 5-nm thick Py film magnetized in-plane by $H_0 = 1000$ Oe. (b) Zoom near the bottom of the spectrum.

In contrast to the dispersion relation of photons or acoustic phonons, the spin-wave dispersion has an energy gap, i.e., the spin-wave frequency is nonzero at $k = 0$. The spin-wave mode at $k = 0$ is called the ferromagnetic resonance (FMR) mode, and it corresponds to uniform precession of the magnetization with a spatially constant phase (i.e., to a spin wave with an infinite wavelength). According to Equation 2.8, the FMR frequency is given by

$$f_{\text{FMR}} = \gamma/2\pi\sqrt{H_0(H_0 + (4\pi - N^a)M_s)}, \quad (2.9)$$

where $N^a = \tilde{H}_a/M_s$. As a first approximation, the FMR frequency is proportional to H_0 due to the Zeeman interaction. The term $(4\pi - N^a)M_s = 4\pi M_s - \tilde{H}_a$ describes contributions of the dipolar anisotropy ($4\pi M_s$, where the factor 4π comes from a component of the demagnetizing tensor $\overset{\leftrightarrow}{N}$, see Equation 2.5) and PMA (\tilde{H}_a , see Equation 2.7).

For short wavelengths (for large k), the exchange interaction dominates and the dispersion relation exhibits a quadratic behaviour $f(k) \propto k^2$, independent of φ , the angle between \mathbf{k} and \mathbf{H}_0 (see Figure 2.4(a)). In contrast, for long wavelengths (for small k), the dipolar interaction becomes dominant, and $f(k) \propto \sqrt{H_0(H_0 + 4\pi M_s(F - F^a))}$, where the factors F and F^a strongly depend on φ . Thus, the inherent anisotropy of the dipole-dipole interaction results in anisotropic spin-wave dispersion.

For $\mathbf{k} \parallel \mathbf{H}_0$ the dipole contribution decreases with increasing wavevector. The competition between the dipole and exchange interactions results in a minimum of the spin-wave dispersion at non-zero wavevector k_{min} (Figure 2.4(b)). As we will see below, the existence

of the minimal frequency f_{\min} at non-zero wavevector has important consequences for the spin-wave dynamics. It should be also emphasized that this lowest-frequency mode is doubly degenerated, since there are two minima: at $k_z = k_{\min}$ ($\varphi = 0$, see Figure 2.3) and $k_z = -k_{\min}$ ($\varphi = 180^\circ$).

2.3 Spin waves in waveguides

In the previous section, we have considered spin waves in extended ferromagnetic films. However, waveguiding structures capable of directional propagation of spin waves are of crucial importance for magnonics devices. Therefore, spin waves are often studied in waveguides in the form of narrow strips [47]. In this section, we briefly outline the key features of spin waves in such structures.

2.3.1 Longitudinally magnetized waveguide

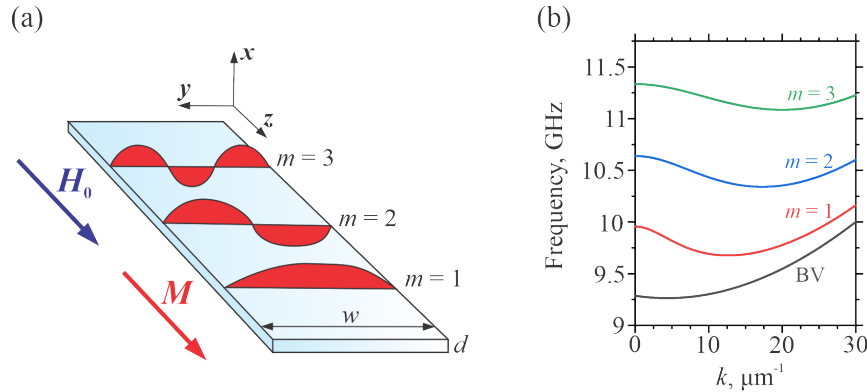


Figure 2.5 (a) Schematic of the longitudinally magnetized waveguide and of transverse profiles of the dynamic magnetization for the first three normal waveguide modes. (b) Dispersion curves for a Py waveguide with the width $w = 0.5 \mu\text{m}$ and the thickness $d = 5 \text{ nm}$ magnetized along its long axis by the external field $H_0 = 1000 \text{ Oe}$. For comparison the dispersion curve for the BV mode in an Py extended film is shown.

First, we consider the case of a ferromagnetic stripe of a width w magnetized along its length (Figure 2.5 (a)). If the stripe is long enough, the fictitious magnetic charges are located at a great distance and the generated static demagnetizing field is vanishingly small (if one neglect the areas close to the waveguide ends, of course). Thus, the effective field inside the stripe is homogeneous and is equal to the external magnetic field. Note that in the extended film, both in-plane components of wavevector \mathbf{k} can change continuously. However, in the case of the stripe, the wavevector component perpendicular to the waveguide axis k_y is quantized, which corresponds to the formation of standing waves in the y direction. The discrete values of k_y can be expressed as $k_y = \pi m / w$, where $m = 1, 2, 3, \dots$ is the index of normal waveguide

modes [47]. For a given value of m , the dispersion of the corresponding mode can be obtained by substituting the expression for the total wavevector $\mathbf{k} = k_z \mathbf{e}_z + \pi m / d \mathbf{e}_y$ in Equation 2.8.

Figure 2.5(b) shows the dispersion curves for a Py waveguide with the width $w = 0.5$ μm and the thickness $d = 5$ nm magnetized by the external field $H_0 = 1000$ Oe. As can be seen from the data, dispersion curves for the normal waveguide modes are shifted to larger frequencies with respect to that of the BV mode in the unconfined film. This is not surprising, since all waveguide modes are characterized by a non-zero component of the wavevector k_y perpendicular to H_0 , while for the unconfined BV spin wave $k_y = 0$ by definition. The exchange energy is known to increase with the increase of the total wavevector, which makes the dispersion curves shift to larger frequencies with the increase of the mode number.

2.3.2 Transversally magnetized waveguide

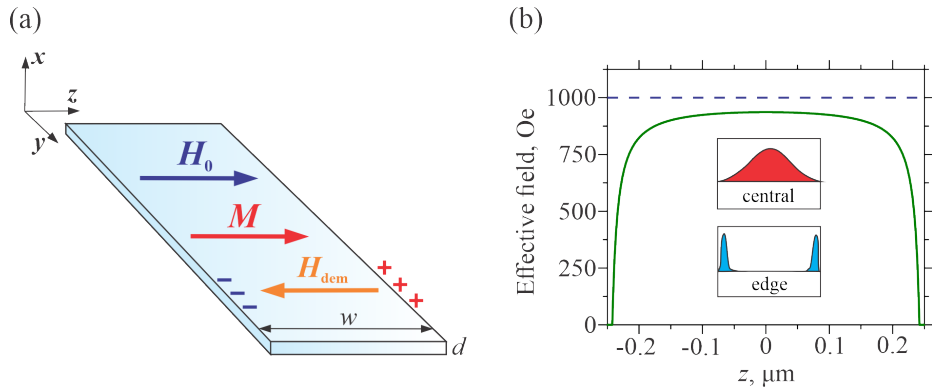


Figure 2.6 (a) Schematic of the transversely magnetized waveguide. (b) Calculated distribution of the internal effective magnetic field across the width of a Py waveguide with the width $w = 0.5$ μm and the thickness $d = 5$ nm magnetized by the external field $H_0 = 1000$ Oe. Horizontal dashed line marks the value of the external magnetic field. Insets show the transverse profiles of the dynamic magnetization for the first central mode and the first edge mode.

Now we consider a more complex case of a transversely magnetized stripe (Figure 2.6(a)). In contrast to a longitudinally magnetized waveguide, in this geometry the static demagnetizing field \mathbf{H}_{dem} is not zero due to the magnetic charges that are formed at the lateral edges of the waveguide. According to [81], the z -component of the demagnetizing field can be calculated as

$$H_{\text{dem},z}(z) = -N^{\text{dem}}(z)M_s, \quad (2.10)$$

where $N^{\text{dem}}(z)$ is the coordinate-dependent component of the demagnetizing tensor $\overset{\leftrightarrow}{N}$ (see Equation 2.5)

$$N^{\text{dem}}(z) = \frac{1}{\pi} \left[\arctan\left(\frac{d}{2z+w}\right) - \arctan\left(\frac{d}{2z-w}\right) \right].$$

Due to the demagnetizing effects, the effective field inside such a waveguide $H_{\text{eff},z}(z) = H_0 + H_{\text{dem},z}(z) = H_0 - N^{\text{dem}}(z)M_s$ is smaller than the applied external field H_0 . Figure 2.6(a) shows the distribution of $H_{\text{eff},z}(z)$ calculated for the Py waveguide the width $w = 0.5 \mu\text{m}$ and the thickness $d = 5 \text{ nm}$ magnetized by the external field $H_0 = 1000 \text{ Oe}$. As can be seen from the data, the effective field varies over the width of the strip and substantially decreases near the edges, creating the so-called spin-wave wells, where spin waves can be localized.

Two types of the normal spin wave modes exist in the transversally magnetized waveguide [82]. These modes are characterized by different frequencies and different distributions of the dynamic magnetization across the waveguide width (see insets in Figure 2.6(b)). The first type is central modes. As the name implies, central modes are spread over the entire width of the waveguide. The second type is edge modes, which are localized in the areas of the reduced effective field. Therefore, the typical frequencies of the edge modes are lower than that of the central modes. We note that, due to the significant inhomogeneity of the effective field, there are no simple analytical models that can describe the central and the edge modes with good accuracy. As a rule, micromagnetic simulation should be used for the analysis of their properties.

2.4 Magnons

So far, we have considered spin waves only in the context of the phenomenological LLG equation. However, the semi-classical continuum model provides only a limited view of properties of spin waves. To understand many phenomena involving spin waves, it is more convenient to describe them using the "corpuscular language". According to the general principle of corpuscule-wave duality, spin waves can be regarded as flows of quasiparticles with energy $\epsilon = hf$ and quasimomentum $\mathbf{p} = \hbar\mathbf{k}$, where $h = 2\pi\hbar$ is the Planck constant. These quasiparticles are called magnons and represent quanta of spin waves. The spin-wave dispersion relation $f(\mathbf{k})$ defines the dependence $\epsilon(\mathbf{p})$ for magnons. Within such an approach, any processes of the excitation or damping of coherent spin waves can be regarded as a creation or annihilation of magnons that have distinct values of f and \mathbf{k} . It can be shown, that the density of magnons corresponding to a specific spin-wave mode is $N_f \propto \mathbf{m}_f^2$, i.e., it is proportional to the squared dynamical magnetization (amplitude) \mathbf{m}_f of the mode [1]. This relation serves as a link between the continuum and quantum approaches. In the rest of the thesis, we use terms "spin waves" and "magnons" interchangeably.

Apart from coherent magnons that can be created by various methods of external excitation, in ferromagnets at any temperature $T > 0$, there exist noncoherent magnons excited by thermal fluctuations in the lattice. The distribution of such magnons over the energies is determined by the magnon spectral density $\rho(f) = D(f)n(f)$, where $D(f)$ is the density

of magnons states, which can be found from the spin-wave dispersion relation, and $n(f)$ is the distribution function, which defines the number of magnons in a state with energy hf . From the rigorous quantum theory of spin waves [83], it follows that magnons are quasiparticles with spin equal to unity, i.e., they are boson. Thus, magnons obey the Bose-Einstein statistics and their distribution function is

$$n(f) = \frac{1}{e^{\frac{hf-\mu}{k_B T}} - 1}, \quad (2.11)$$

where k_B is the Boltzmann constant and μ is the chemical potential. The density of magnons in the magnetic system is then given by

$$N = \int_{f_{\min}}^{\infty} \rho(f) df = \int_{f_{\min}}^{\infty} D(f)n(f) df,$$

where f_{\min} is the minimum magnon frequency (see Figure 2.4(b)).

As is known from statistical physics [84], if the total number of quasiparticles in the system is not fixed, the chemical potential of the system $\mu = 0$ at the thermodynamic equilibrium. Since magnons can be freely created and annihilated due to the energy exchange with the lattice, their chemical potential is zero. However, one can increase the chemical potential of the magnons gas by using methods of external excitation, which break the equilibrium with the lattice. As it can be seen from Equation 2.11, μ cannot be larger than the minimum energy of magnons hf_{\min} , otherwise $n(f)$ becomes negative. Thus, at a given temperature T , the condition $\mu = hf_{\min}$ corresponds to the critical magnon density $N_C(T)$. If one creates a system with the density of magnons larger than $N_C(T)$, the part of the external pumped magnons accumulate in the lowest-frequency magnon state with hf_{\min} forming a macroscopic coherent quantum state. This phenomena is called Bose-Einstein condensation (BEC) [85,86]. The BEC of magnons was achieved for the first time in 2006 in insulatic magnetic films at room temerature by means of parametric pumping [87]. Since then, the study of magnon BEC has remained an active research area due to many unusual and interesting effects related to it [88–96].

2.5 Nonlinear magnetization dynamics

At low levels of excitation or low temperatures, magnons behave as an ideal gas of quasiparticles. However, at high levels of excitation or high temperatures, magnons start to interact with each other, which results in a wide variety of nonlinear phenomena: parametric and kinetic instabilities of spin waves [1, 24, 25], formation of various spin-wave solitions [22,97], spin wave chaos [98], etc. In this section, we discuss two nonlinear effects that are

especially important for understanding the results of this thesis.

2.5.1 Nonlinear frequency shift

In the linear approximation, the spin-wave frequencies are independent of the precession amplitude. However, this is not the case in the nonlinear regime. To illustrate this, let us consider the FMR frequency. The expression for the "linear" FMR frequency (Equation 2.9) was derived in the limit of $\|\mathbf{m}\| \ll M_z \approx M_s$. In more general case, f_{FMR} can be expressed as

$$f_{\text{FMR}} = \gamma/2\pi\sqrt{H_0(H_0 + (4\pi - N^a)M_z)}. \quad (2.12)$$

which differs from Equation 2.9 by the substitution of M_z for the saturation magnetization M_s . Since in the micromagnetic approximation the total length of the magnetization vector remains equal to M_s , $M_z = \sqrt{M_s^2 - \mathbf{m}^2}$. Therefore, as the precession amplitude increases (or in other words, as the number of magnons increases), the z -component of the magnetization decreases (Figure 2.7) resulting in a change of f_{FMR} - the nonlinear frequency shift.

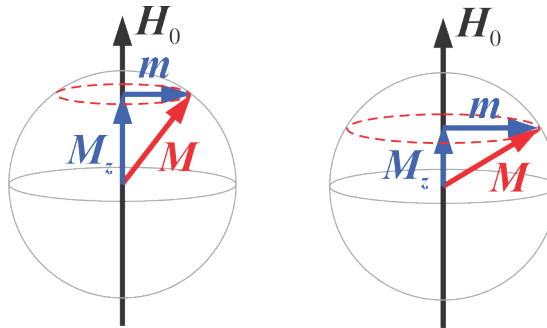


Figure 2.7 Origin of the nonlinear frequency shift: with the increase of the precession amplitude, M_z decreases resulting in a change of the spin-wave frequency.

One can distinguish three cases:

- If the dipolar anisotropy is larger than PMA ($4\pi - N^a > 0$ in Equation 2.12), the FMR frequency decreases with increasing amplitude, i.e., the nonlinear frequency shift is negative ("red"). For example, in in-plane magnetized Py films, the nonlinear frequency shift is always negative.
- If the shape anisotropy and PMA compensate each other ($4\pi - N^a \approx 0$), the spin-wave frequency does not depend on the amplitude. In this case, the FMR frequency is determined solely by the Zeeman interaction $f_{\text{FMR}} = \gamma H_0/2\pi$.
- If PMA is larger than the dipolar anisotropy ($4\pi - N^a < 0$), the FMR decreases with increasing amplitude, i.e., the nonlinear frequency shift is positive ("blue").

2.5.2 Nonlinear damping

Another consequence of the nonlinearity of magnetization dynamics (or, to put it more precisely, of the LLG equation) is an emergence of the coupling between different spin-wave modes, which are independent in the linear approximation. This coupling results in a variety of nonlinear effects. The most important of them is the parametric excitation of secondary spin-wave modes by the excited dominant mode, when the amplitude of the latter exceeds certain threshold value. Again, we illustrate this effect on an example of the FMR mode. It is well-known from the early 50s, that if one excites the FMR mode by a microwave field and gradually increases the amplitude of the latter, the amplitude of the FMR will stop to grow after a certain value of the applied microwave power [99, 100]. The effect can be understood as follows: when the amplitude of the FMR mode exceeds the critical value, it becomes unstable and two FMR magnons with $k = 0$ create a pair of magnons with opposite wavevectors $k, -k$ and equal frequencies due to the four-magnon scattering (Figure 2.8) [101, 102]. As a result, the energy of the dominant mode (in the considered case, the FMR mode) is redistributed over the spin-wave spectrum. This relaxation mechanism can be described as amplitude-dependent nonlinear damping [103–105].

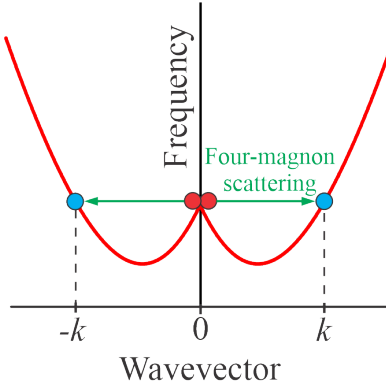


Figure 2.8 Illustration of the four-magnon scattering: two FMR magnons (red circles) with $k = 0$ create a pair of magnons with oppositely directed wavevectors and equal frequencies (blue circles). Curves are schematic dispersion branches of the BV spin waves.

We note that the four-magnon scattering depicted in Figure 2.8 is a resonant process, i.e., it conserves the total energy and momentum. However, in strongly nonequilibrium magnetic system, there also exist non-resonant processes [106–109], which cannot be described in terms of energy- and momentum-conserving magnon-magnon interactions. As we will see below, the nonlinear damping caused by resonant and non-resonant processes imposes strict limitations on the operation and efficiency of magnetic nanodevices.

2.6 Spin Hall effect

In the previous sections, we have reviewed the basics of spin-wave physics. In the remaining part of this chapter, we consider the main aspects of magnetization dynamics in the presence of the so-called spin-orbit torque, and we start our discussion with the concept of a pure spin current.

In a conventional charge current, spin “up” and “down” electrons flow together, resulting in a net flow of charge without the simultaneous transfer of spin (Figure 2.9(a)). However, if one somehow makes ”up” and ”down” electrons to flow in the opposite directions, the so-called pure spin current will be created - a flow of spin not accompanied by directional transfer of electrical charge (Figure 2.9(b)) [110].

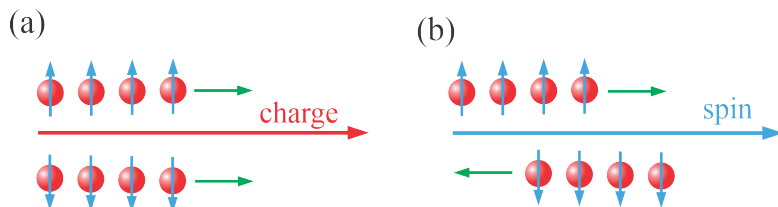


Figure 2.9 Schematic of a charge current (a) and a pure spin current (b).

Several physical mechanisms can be utilized to create pure spin currents [111]. One of them is the spin-Hall effect (SHE) [112]. The SHE originates from the spin-dependent electron scattering in nonmagnetic materials that have strong spin-orbit interaction, such as platinum (Pt), tantalum (Ta) and tungsten (W). When an electrical current I flows in the plane of a film made of such a material, electrons with opposite spins are scattered in the opposite directions (Figure 2.10(a)). This gives rise to a pure spin current I_s flowing out-of-plane, with the polarization σ , perpendicular to the direction of current. Note that by reversing the direction of the electrical current, one reverses the polarization of the pure spin current.

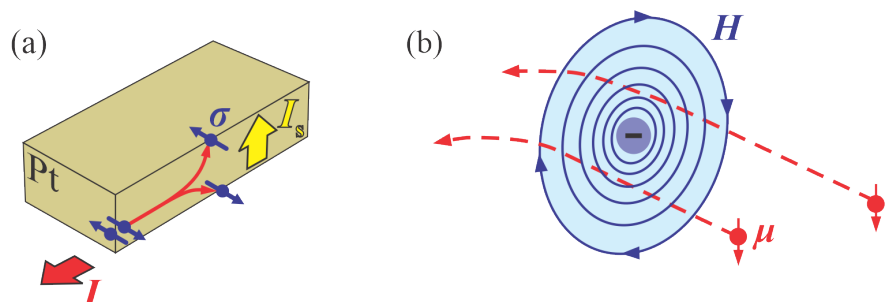


Figure 2.10 (a) Electrical current I can be converted into a pure spin current I_s due to the SHE in a film made of a material with strong spin-orbit interaction, such as Pt. (b) Schematic of a spin-dependent electron scattering from a negatively charged ion in vacuum.

The main microscopic origin of the SHE is spin-orbit interaction (SOI). To illustrate how SOI can result in a spin-dependent scattering, let us consider a simple model: a free electron in vacuum approaches a negatively charged ion with velocity \mathbf{v} (Figure 2.10(b)). In the rest frame of the electron, it experiences a magnetic field \mathbf{H} that arises from the Lorentz transformation of the electrical field \mathbf{E} of the ion. The magnetic field $\mathbf{H} \propto \mathbf{v} \times \mathbf{E} \propto \mathbf{v} \times \mathbf{r} \propto -\mathbf{L}$, where \mathbf{L} is the orbital angular momentum of the electron. The Zeeman energy (see Equation 2.3) of the electron in this effective magnetic field is $E_Z = -\boldsymbol{\mu} \cdot \mathbf{H}$. Since the spin of the electron $\mathbf{s} \propto -\boldsymbol{\mu}$, the energy $E_Z \propto -\mathbf{s} \cdot \mathbf{L}$ is called the spin-orbit energy, because it arises from the interaction between the spin and orbital momentum of the electron. Note that the effective magnetic field \mathbf{H} is inhomogeneous, it becomes weaker as the distance to the ion increases. As is known from classical electrodynamics, a gradient of the magnetic field exerts a force on the magnetic moment $\mathbf{F} = -\nabla(E_Z) = \nabla(\boldsymbol{\mu} \cdot \mathbf{H})$. Therefore, if the magnetic moment $\boldsymbol{\mu}$ of the electron is "down" and the electron approaches the ion from the right (left) side, magnetic field and magnetic moment are parallel (antiparallel) and the force \mathbf{F} pushes the electron towards increasing (decreasing field), that is towards the left, as shown in Figure 2.10(b). In contrast, electrons with magnetic moment "up" are scattered to the right, regardless of which side it approaches the ion.

The described spin-dependent scattering of electrons in vacuum is a simple explanation of the celebrated Mott scattering [113]. In 1971, Dyakonov and Perel were the first to notice that a similar effect is possible when an electrical current flows through a material with strong SOI [114]. The prediction went practically unnoticed until 1999, when Hirsch rediscovered the effect and named it the spin Hall effect due to the similarity to the normal Hall effect [115]. Since then, the SHE has been the object of intensive theoretical and experimental studies due to the fundamental importance and a host of potential applications [116].

2.7 Spin-orbit torque

If one brings a SHE layer in contact with a ferromagnetic film, the generated pure spin current I_s flows through the interface into the ferromagnet and interacts with its magnetization \mathbf{M} (Figure 2.11(a)). The effect of pure spin current on the magnetization is often described by an additional torque [117], called the spin-orbit torque (SOT), included in the LLG equation

$$\frac{d\mathbf{M}}{dt} = \underbrace{-\gamma(\mathbf{M} \times \mathbf{H}_{\text{eff}})}_{\text{precession}} + \underbrace{\frac{\alpha}{M_s}(\mathbf{M} \times \frac{d\mathbf{M}}{dt})}_{\text{damping}} + \underbrace{\frac{\beta}{M_s^2}(\mathbf{M} \times (\mathbf{M} \times \boldsymbol{\sigma}))}_{\text{spin-orbit torque}}, \quad (2.13)$$

where β is a parameter which determines the strength of the SOT. Note that $\beta \propto J/d$, where J is the density of electrical current and d is the thickness of the ferromagnetic layer.

Therefore, the effects of the SOT are considerable only in magnetic nanostructures, in which the thickness of the active magnetic layer does not exceed tens of nanometers and high current densities can be achieved ($10^{11} - 10^{12} \text{ A/m}^2$).

As can be seen from Equation 2.13, the SOT has the same form as the Gilbert damping torque, while its sign depends on the polarity of the spin current σ . For one polarization, the SOT acts in the same direction as the Gilbert torque, creating additional magnetic damping. However, for the opposite polarization, the SOT acts as an anti-damping torque, as shown in Figure 2.11(b). Thus, in the framework of Equation 2.13, the effect of the SOT on the magnetization can be described as a simple modification of magnetic damping. According to [118], the effective Gilbert constant varies linearly as a function of current

$$\alpha(I) = \alpha_0(1 - I/I_C) \quad (2.14)$$

where α_0 is the effective damping constant at $I = 0$, and $I_C \approx \alpha_0 f$ is the critical current proportional to the spin-wave frequency. When I reaches the critical value I_C , the SOT completely compensates the damping torque, and one can expect the onset of magnetization auto-oscillations², i.e., the steady state precession of the magnetization around the effective magnetic field (Figure 2.11(c)). Note that according to Equation 2.14, the spin-wave mode with smallest frequency in the magnetic system is the first to enter the auto-oscillation regime due to the smallest critical current.

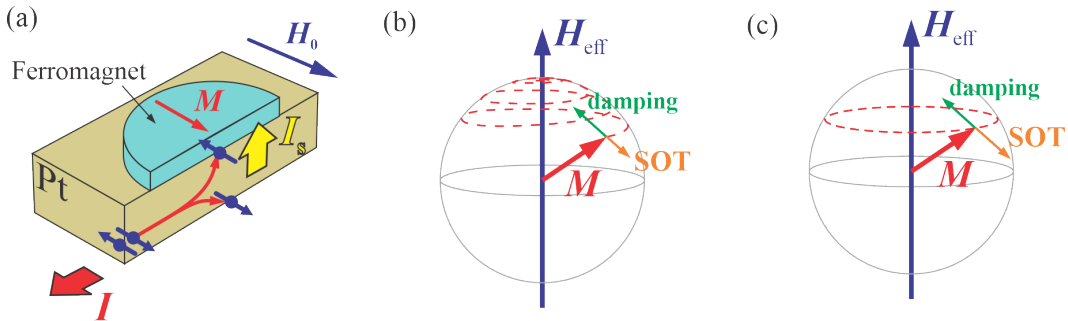


Figure 2.11 (a) Illustration of the injection into a ferromagnetic layer of a pure spin current I_s generated due to the SHE in a Pt film. (b) The injected spin current exerts the SOT on the magnetization. Under certain conditions, the SOT counteracts the damping torque. (c) When the magnitude of the SOT reaches a certain critical value, it completely compensates the damping torque resulting in the onset of steady-state magnetization auto-oscillations.

Let us emphasize that Equation 2.13 is a deterministic equation that describes the magnetization dynamics at zero temperature. Thus, it neglects the influence of magnetic fluctuation

²Auto-oscillations can be defined as sustained oscillations in a nonlinear system, generated by an energy source that lacks any periodicity [119]. In conventional forced and parametric resonant systems, oscillations are driven by a periodic external force, which defines the amplitude and the frequency of the oscillations. In contrast, the amplitude and the frequency of auto-oscillations are determined by the properties of the nonlinear system itself.

(thermally excited magnons, see Section 2.4) always existing in ferromagnets at $T > 0$. The effects of fluctuations can be included in Equation 2.13 as an additional fluctuating thermal field [120]. By analyzing the stochastic form of Equation 2.13, another important effect of the SOT was found - namely, the SOT drives the magnetic system out of thermal equilibrium resulting in the enhancement or suppression of magnetic fluctuations, depending on the direction of current [121]. This effect of the SOT can be described in terms of the current-dependent spectral magnon density

$$\rho(f, I) = \frac{\rho_0}{1 - I/I_C}, \quad (2.15)$$

where $\rho_0 = \rho(f, 0)$ is the spectral magnon density at $I = 0$ and $I_C \approx \alpha_0 f$ is the critical current, at which the spectral magnon density is expected to diverge [122]. As follows from Equation 2.15, one can expect the strongest enhancement for the lowest-frequency magnons that exhibit the smallest critical current.

2.8 SOT oscillators

According to the simple picture based on Equation 2.14, the lowest-frequency spin-wave mode is expected to switch to the auto-oscillation regime as soon as the driving current reaches the corresponding critical value I_C . However, since the SOT not only modifies the effective magnetic damping but also enhances thermal fluctuations (Equation 2.15), the experimental demonstration of the excitation of coherent magnetic oscillations by the SOT turned out to be a nontrivial task. To understand why, let us consider a magnetic system driven by spatially uniform spin current (Figure 2.12(a)). Figure 2.12(b) shows the current dependence of the spectral magnon density at f_{\min} (the minimal spin-wave frequency) measured in such a system. According to Equation 2.15, $\rho(f_{\min}, I)$ should diverge at $I_C \approx \alpha_0 f_{\min}$ due to the complete damping compensation, and, at currents above I_C , the lowest-frequency mode can be expected to make a transition to the auto-oscillation regime. Instead, $\rho(f_{\min}, I)$ saturates when the current approaches the critical value, and starts to decrease at $I > I_C$, indicating an onset of a new relaxation process that limits the amplitude of the lowest-frequency mode. The reason is that the SOT simultaneously enhances thermal fluctuations of *all* spin-wave modes existing in the magnetic system, i.e., it lacks the mode selectivity. Consequently, the SOT brings the system in a strongly nonlinear state, where the modes become coupled (see Section 2.5.2). This results in nonlinear damping of the lowest-frequency mode (the dominant mode) preventing its transition to the auto-oscillation regime. Thus, application of spatially uniform SOT to an extended magnetic system does not result in the excitation of coherent magnetization auto-oscillations [121].

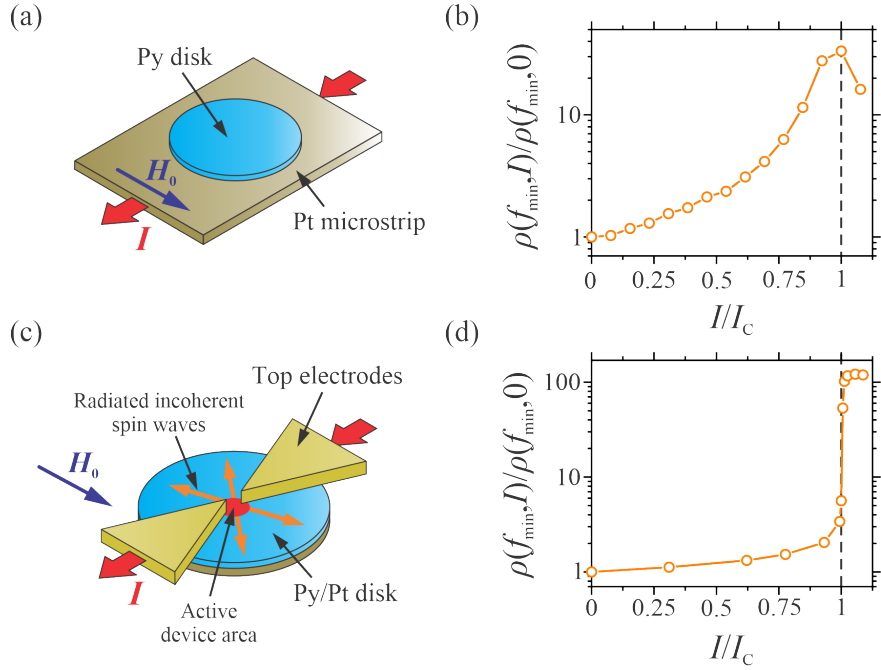


Figure 2.12 (a) Schematic of a simple SOT device driven by spatially uniform spin current. Due to the onset of nonlinear damping, coherent auto-oscillations in such a system are not possible. (b) Current dependence of the normalized spectral magnon density at f_{\min} measured in a system shown in (a). The data are adapted from [121]. (c) Schematic of a nano-gap SOT-oscillator. Due to the local injection of spin current into the area between the electrodes, the adverse effects of nonlinear damping are suppressed, and the system can make a transition to the auto-oscillation regime. (d) Current dependence of the normalized spectral magnon density at f_{\min} measured in a system shown in (c). The data are adapted from [55].

However, a way to overcome the detrimental effects of nonlinear damping was soon found. The approach is based on a local injection of spin current into a nano-scale region of an extended magnetic film (Figure 2.12(c)) [68]. In this localized active area, the SOT enhances a large number of different spin-wave modes, as discussed above. Since the high-frequency spin waves have large group velocities (see the spin-wave spectrum in Figure 2.4(a)), they quickly escape from the active region, resulting in their efficient suppression by the radiation losses. Meanwhile, the low-frequency modes have much smaller group velocities, and therefore their radiation losses are minimal. Since magnon–magnon scattering rates are proportional to the populations of the corresponding modes, the radiation of high-frequency incoherent magnons from the active area results in reduced nonlinear damping of the lowest-frequency mode. Figure 2.12(d) demonstrates the current dependence of the spectral magnon density at f_{\min} measured in the system shown in Figure 2.12(c). As can be seen from the data, $\rho(f_{\min}, I)$ rapidly increases at $I > I_C$ and becomes two orders of magnitude larger than its equilibrium value, indicating the transition of the system to the auto-oscillation regime.

The above-described approach enabled the excitation of coherent magnetic auto-oscillations by the SOT in 2012 [55]. This work initiated intense experimental and theoretical studies

of the devices known today as SOT oscillators [68, 69]. Thanks to the flexible layout and the simplicity of fabrication, a large variety of SOT oscillators with different materials and geometries has been proposed and experimentally demonstrated [123–132]. SOT oscillators exhibit good oscillation characteristics at room temperature [133–135], they are CMOS compatible [136], and it is possible to utilize arrays of SOT oscillators to perform neuromorphic computations [137, 138]. All these features make these devices very promising for a wide range of practical applications [69].

Chapter 3

Methods

3.1 Brillouin light scattering spectroscopy

There are many experimental methods to detect spin waves: inelastic neutron scattering [139], electronic microwave spectroscopy [46], time-resolved Kerr [140] and X-ray microscopies [141], magnetometry based on nitrogen-vacancy centers in diamond [142], etc. However, probably the most powerful and versatile tool is Brillouin light scattering (BLS) spectroscopy [143–145], as it allows frequency-, time-, space- and wavevector-resolved studies of spin-wave dynamics. BLS spectroscopy was used as the primary experimental tool for obtaining the results presented in Chapters 4-6, so in this section we briefly cover the basics of this technique.

3.1.1 Principles of BLS

The operation principle of the BLS technique relies upon the inelastic scattering of photons from magnons. When light interacts with a magnetic material, a photon can create (the so-called Stokes scattering process) or absorb (the anti-Stokes process) a magnon as schematically shown in Figure 3.1. Since, during these scattering processes, the total energy and momentum are conserved, the energy $h f_S$ and the momentum $\hbar \mathbf{k}_S$ of the scattered photon are given by

$$h f_S = h f_I \mp h f_M \quad \hbar \mathbf{k}_S = \hbar \mathbf{k}_I \mp \hbar \mathbf{k}_M,$$

where $h f_I$ and $\hbar \mathbf{k}_I$ are the energy and the momentum of the incident photon, $h f_M$ and $\hbar \mathbf{k}_M$ are the energy and the momentum of the created/annihilated magnon. As follows from these relations, the scattered light carries information about the probed spin wave. Thus, by measuring the frequency shift $|f_S - f_I|$, one can obtain the value of the spin-wave frequency f_M while the spin-wave wavector \mathbf{k}_M can be determined from the scattering geometry, i.e.,

the incidence and detection angle of the light.

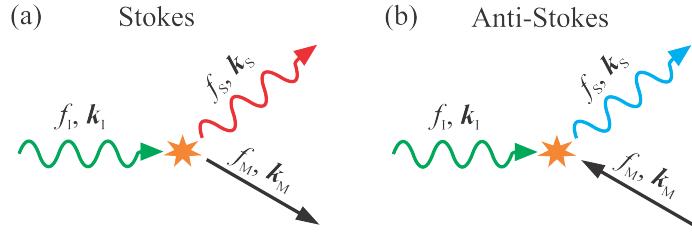


Figure 3.1 Schematic representation of the Stokes (a) and anti-Stokes (b) scattering processes.

To perform such measurements, a source of highly monochromatic light is required. In a typical BLS experiment a solid-state laser is used with a wavelength of $\lambda = 532$ nm, which corresponds to the frequency f_l of about 600 THz. However, the characteristic frequencies of magnons f_M studied in this thesis are of order of tens GHz, which are many orders of magnitude smaller than f_l . Therefore, a high-resolution spectrometer is needed to detect such small shifts in the frequency of the scattered light. Usually in such cases, a Fabry-Perot interferometer (FPI) is used as a frequency analysis tool.

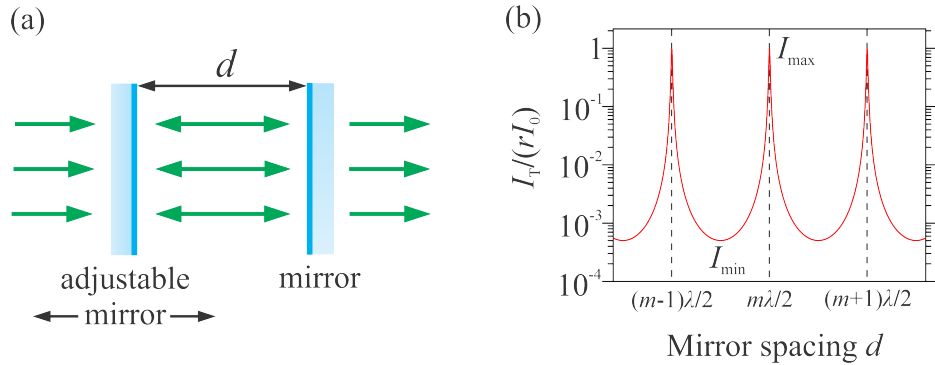


Figure 3.2 (a) Schematic of a Fabry-Perot interferometer (FPI). (b) Transmission of the FPI as a function of the distance d between the mirrors.

A simple FPI consists of two parallel highly-reflective mirrors placed at distance d from each other (Figure 3.2(a)). When monochromatic light with the wavelength λ and with the intensity I_0 is incident perpendicularly on the FPI, it undergoes interference due to multiple reflections between two inner surfaces of the mirrors. As a result, the intensity of the transited light I_T depends on d and is given by

$$I_T = \frac{rI_0}{1 + (4F^2/\pi^2)\sin^2(2\pi d/\lambda)}, \quad (3.1)$$

where $r < 1$ is a parameter, which characterizes the losses in the system, and F is a quality factor called the finesse, which depends mainly on the reflection coefficient of the mirrors [143]. The dependence $I_T(d)$ is shown in Figure 3.2(b) (note the logarithmic scale). As

can be seen from the data, only light of wavelengths satisfying the interference conditions $\lambda = 2d/m$ is transmitted, where $m = 1, 2, 3..$ is an integer number. Thus, by varying the mirrors spacing d (usually it is done by means of piezoelectric transducers), one can scan the intensity of the light at different wavelengths and thus analyze its frequency spectrum.

The period between successive transmitted frequencies is called the free spectral range (FSR) and is given by $\Delta f = c/2d$, where c is the speed of light. The FSR is the maximum frequency range accessible by the interferometer before the higher transmission orders appear in the spectrum. Therefore, an unambiguous interpretation of the spectrum is possible only if the spectrum lies entirely within the FSR. It might seem that one can make the FSR arbitrary large by decreasing d . However, as follows from Equation 3.1, the FSR is related to the full width at half maximum δf of the transmission peaks through the finesse $F = \Delta f/\delta f$. The width δf determines the frequency resolution of the interferometer, i.e., the minimum frequency difference between two points in the spectrum that can be distinguished experimentally. Therefore, with decreasing d , the FSR increases but the frequency resolution deteriorates, and vice versa.

Another important parameter of the FPI is contrast, which is defined as a ratio of the maximal transmitted intensity to the minimal one, $C_{\text{FPI}} = I_{\max}/I_{\min} \approx F^2$. Due to the existing limitations on the quality of the mirrors, the finesse F cannot be made much greater than 100, and therefore $C_{\text{FPI}} \approx 10^4$. This means that, in the case of a conventional FPI, a parasitic background with the intensity 10^{-4} of the incident light exists in the spectrum. Since the typical intensity of BLS from magnons is $< 10^{-8}$ of the incident light, the contrast of a single FPI is insufficient to resolve rather weak BLS signals from magnons masked by the strong parasitic background.

As follows from these arguments, a high-resolution and high-contrast spectrometer with large FSR is required to enable the BLS measurement of the magnon spectrum. A tool satisfying these requirements was developed by Sandercock in the early 70s [146, 147] and is shown in Figure 3.3(a). It is a tandem six-pass Fabry-Perot interferometer (TFPI), which consists of two Fabry-Perot etalons FPI1 and FPI2. The first interferometer of spacing d_1 transmits $\lambda_1 = 2d_1/m_1$ for integer m_1 , while the second interferometer of spacing d_2 transmits $\lambda_2 = 2d_2/m_2$ for integer m_2 . Only if the light wavelength $\lambda = \lambda_1 = \lambda_2$, it will be transmitted through the combination of etalons. Therefore, if one independently sets the spacings d_1 and d_2 so as to transmit a given wavelength λ , the neighboring transmission peaks will not coincide and only their "ghosts" will remain in the combined (tandem) transmission (Figure 3.3(b)). The FSR of the system is thus increased by a considerable factor over that of a single FPI, while the frequency resolution δf remains the same. Typical frequency resolution of the TFPI is $\delta f \approx 100\text{MHz}$ for the FSR of 10 GHz. As can be seen from Figure 3.3(a), the beam of light passes each etalon three times before it is guided to a photon detector. In this

case, the resultant contrast of the TFPI is $C_{\text{TFPI}} = C_{\text{FPI}}^6 \approx 10^{24}$. Note that this value is a theoretical upper bound and the experimentally achievable values of C_{TFPI} are smaller than 10^{15} . Nevertheless, they are high enough to enable detection of BLS signals from magnons.

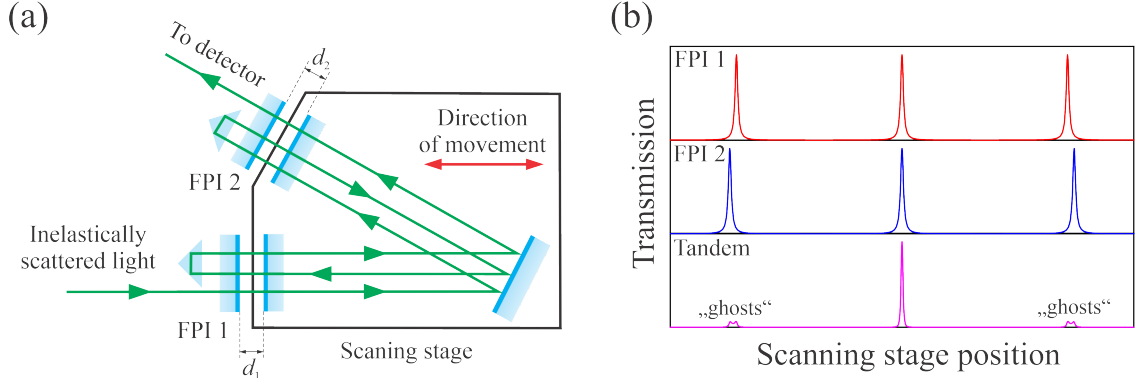


Figure 3.3 (a) Schematics of a tandem Fabry-Perot interferometer (TFPI). (b) Transmission curves of the two etalons, FPI1 and FPI2, characterized by a slightly different mirror spacing, compared with that of the tandem operation. Only ghosts peaks of neighboring orders remain in the tandem transmission.

3.1.2 Micro-focus BLS

Since the lateral dimensions of the samples studied in this thesis do not exceed a few micrometers, we utilized a variation of the BLS technique called micro-focus BLS (μ BLS) [148–150], which offers high spatial resolution at expense of wavevector resolution. The main components of the μ BLS setup are shown in Figure 3.4 (a). The probing light generated by a laser with the wavelength $\lambda = 532$ nm is focused on the sample surface into a diffraction-limited spot by using a microscope objective lens. To avoid the heating of the sample by the focused light, the laser power is usually set below 1 mW. As discussed above, the probing light interacts with magnetic oscillations in the sample, which causes the frequency change of the scattered light. The inelastically scattered light is collected by the same objective lens and sent to the TFPI for frequency analysis. The frequency-selected light transmitted by the TFPI is detected by a photon detector.

Figure 3.4(b) shows a typical BLS spectrum. The intense central peak corresponds to a reference laser beam that enters the interferometer through the strongly attenuated channel. The frequency of the reference beam marks the zero position in a BLS spectrum. The central peak is accompanied by two satellites resulting from the Stokes and anti-Stokes scattering processes. The frequency shift of the satellites is equal to the frequency of the probed magnetic oscillations. Meantime, their intensity (referred to as BLS intensity) at a given frequency is proportional to the intensity of magnetization oscillations at this frequency and at the position of the probing spot. The latter fact allows one to directly image the spatial distribution of magnetic oscillations by rastering of the probing spot over the sample surface.

To enable these spatially-resolved measurements, the sample is mounted on a piezoelectric stage. The spatial resolution of such measurements is determined by the size of the probing laser spot. We also note that by using a stroboscopic detection technique, one can perform time-resolved μ BLS measurements that allows one to investigate the magnetization dynamics in the time domain with a time resolution of about 1 ns [149].

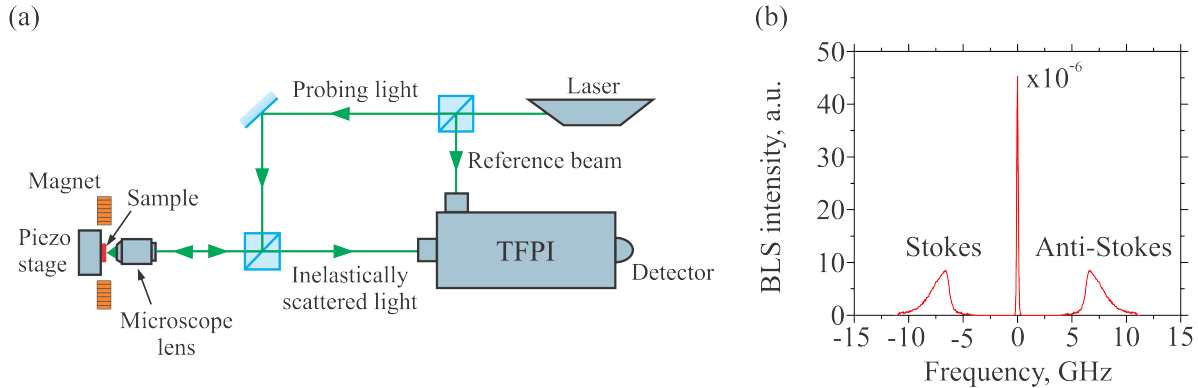


Figure 3.4 (a) Schematic of the main components of the μ BLS setup. (b) Representative BLS spectrum of thermal magnetic fluctuations measured in a 10 nm thick Py film magnetized in-plane by the external field $H_0 = 1000$ Oe.

One particular advantage of BLS over all other techniques is its unmatched sensitivity [143]. In particular, the BLS spectroscopy is capable of detecting thermally excited magnons, naturally existing in magnetic material at non-zero temperatures (see Section 2.4). BLS intensity of magnetic fluctuations is proportional to the reduced spectral density of thermal magnons

$$I_{\text{BLS}} \propto \tilde{\rho}(f) = \tilde{D}(f)n(f), \quad (3.2)$$

where $\tilde{D}(f)$ is the reduced density of states, which is calculated by integration over the wavevectors of magnons accessible to μ BLS [144]. The cutoff wavevector limiting the sensitivity of the setup can be estimated as $k_{\text{max}} \approx 15 \mu\text{m}^{-1}$ [148]. Thus, the resulting BLS signal from magnetic fluctuations contains contributions from all thermal magnons within a range of wavevectors 0 - k_{max} (Figure 3.4(b)). Let us also emphasize that the sensitivity of the μ BLS technique to a specific spin-wave mode continuously decreases with the increase of the mode wavevector [151].

3.2 Micromagnetic simulations

Although the μ BLS technique can simultaneously deliver spectral, spatial and temporal information on dynamical processes in magnetic materials, this is often not enough to unambiguously interpret the experimental data. In such cases, theoretical analysis is needed. However, since the LLG equation is a nonlinear integro-differential equation, it can be solved analytically only in a few specific cases. Therefore, numerical micromagnetic simulations are a valuable tool for gaining a better understanding of the observed phenomena [152–154].

As the name suggests, the key idea of micromagnetic simulations is to solve the LLG equation numerically. To realize this, one has to approximate the continuum theory as a discrete problem. In this thesis, we utilize the open-source software Mumax3 [155] that employs a finite difference method. Within this approach, a given geometry is divided in a regular mesh of rectangular cuboids. Consequently, field quantities are approximated by discrete values on this spatial grid and the derivatives by finite differences.

In general, micromagnetic simulations involve four stages:

- First, one has to set up material (the values of M_s , A_{ex} , α , etc.), geometric (the shape of the studied ferromagnetic body) and simulation (the cell size, the total simulation time, the type of boundary conditions, etc.) parameters. It is also necessary to define the direction and magnitude of the external static magnetic field.
- Second, the total energy of the system is minimized in order to find the equilibrium magnetization configuration.
- In the third stage, the system is perturbed from its equilibrium state. This can be done in a number of ways. For example, time- and space-dependent microwave fields can be added to the model. Magnetization dynamics can be also excited by applying the SOT.¹ However, the most straightforward method is to deflect magnetic moments from their equilibrium orientation by a certain angle.
- Finally, Mumax3 calculates the time- and space-dependent magnetization dynamics by solving Equation 2.1 over a given period of time. Once the simulation is done, the recorded data undergoes post-processing.

¹In this case, Mumax3 solves Equation 2.13 instead of the conventional LLG equation.

Chapter 4

Effects of the SOT on a magnon gas

4.1 Spectral and thermodynamic characteristics of a magnon gas driven by the SOT

4.1.1 Motivation

As discussed in Section 2.7, the SOT not only modifies the effective magnetic damping but also drives the magnetic system out of thermal equilibrium that results in either enhancement or suppression of magnetic fluctuations, depending on the direction of current. These processes can be equivalently described as generation or annihilation of a large number of incoherent magnons spread over a broad interval of frequencies. The case of excitation of incoherent magnons is particularly interesting and important, since magnetic fluctuations enhanced by the SOT strongly influence the characteristics of current-induced auto-oscillations. Therefore, two questions arise:

- *What is the distribution of magnons excited by the SOT?* The SOT is a non-selective excitation mechanism, i.e., it changes magnon populations throughout the entire spectrum. According to the theoretical considerations (Equation 2.15), the SOT efficiency decreases with increasing magnon frequency. Therefore, one can expect that the SOT overpopulates the magnon state corresponding to the minimum magnon frequency. However, it is widely believed that current-driven auto-oscillations usually involve the FMR mode of the system, which for in-plane magnetized systems is not the lowest-frequency mode [156]. For a long time, there was no experimental evidence that could unambiguously confirm one of these points of view.
- *Does the magnon distribution correspond to a quasi-equilibrium state that can be described by the effective thermodynamic characteristics?* Recent theoretical studies claimed that the SOT can drive a magnon gas into a quasi-equilibrium state described

by the Bose-Einstein statistics with non-zero chemical potential, suggesting a relation between current-driven auto-oscillations and BEC of magnons [157–159]. However, for a long time, there was no direct experimental evidence that the state of a magnon gas subjected to the SOT can be treated thermodynamically.

The answers to these two questions are important for a better understanding of the nature of SOT-driven magnetization auto-oscillations, for optimization of their oscillation characteristics for practical applications, and for establishing their connection with such a fundamental effect as magnon BEC. We address both of these questions in this section. The results presented below were published in *Nature Communications* 8, 1579 (2017).

4.1.2 Studied system

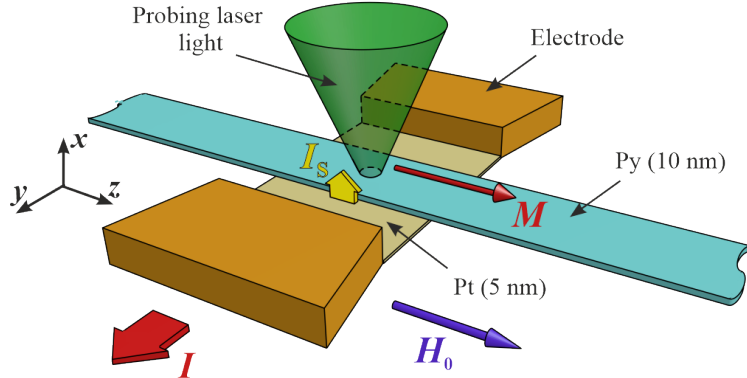


Figure 4.1 Schematic of the experiment.

Figure 4.1 shows the layout of the test devices. They consist of a 2 μm -wide and 5 nm-thick Pt strip overlaid by a 1 μm -wide, 10 nm-thick and 15 μm -long Py strip. The system is magnetized by the static magnetic field H_0 applied along the Py strip. The electric current I flowing in Pt is converted by the SHE into a spin current I_S injected into Py through the Py/Pt interface. The spin current exerts the SOT on the Py magnetization M that results in a decrease or an increase of the magnon population, depending on the direction of current.

We note that the design of the system shown in Figure 4.1 is substantially different from those utilized in the previous works on the excitation of magnetization dynamics by the SOT (see, for example, Figure 2.12 (c)). There are several key differences:

- Devices optimized for efficient excitation of auto-oscillations by the SOT were based on 5 nm-thick or even thinner ferromagnetic layers. The magnon dispersion is very flat in such thin films, resulting in a narrow frequency range accessible to BLS. Therefore, we base our test devices on a 10 nm-thick Py film whose relatively large thickness results in

a sufficiently steep dispersion spectrum of magnons, providing experimental access to the magnon states over a sufficiently broad range of frequencies.

- Because of the spectral degeneracy, all SOT oscillators studied so far did not allow one to experimentally distinguish the FMR mode from the lowest-energy mode, which is necessary to answer the questions posed in the motivation section. To overcome this difficulty, we patterned our Py film into a narrow and long wire with the magnetization directed along its axis. The quantization of magnon spectrum in the transverse direction removes the frequency degeneracy of the low-energy magnon modes, enabling us to experimentally distinguish the FMR mode from the lowest-frequency mode.
- In all SOT oscillators demonstrated up to now, the static configuration of the magnetization was not spatially uniform due to the geometrical effects and the non-uniform Oersted fields of the driving current, resulting in a complex dispersion spectrum that strongly varied with current. However, thanks to the large aspect ratio of the Py wire used in this study, the internal static magnetic field and the static magnetization are uniform in the active device area, avoiding magnon edge states that could complicate the magnon spectrum. The geometry of the sample also produces a uniform Oersted field of the driving current in the active device area, resulting in a negligible current-induced distortion of the magnon spectrum.

4.1.3 Results and discussion

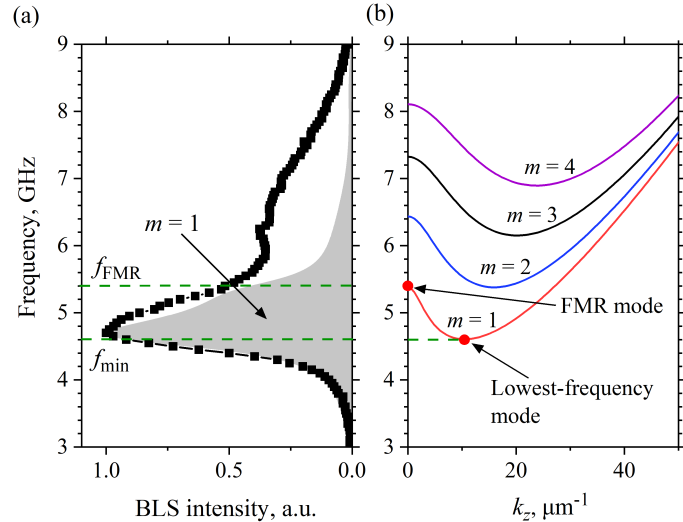


Figure 4.2 (a) BLS spectrum of magnons in the Py strip measured at $I = 0$ and $H_0 = 200$ Oe. Shaded area shows the calculated BLS response for the fundamental magnon mode $m = 1$. Horizontal dashed lines mark the frequency f_{\min} of the lowest-energy magnon state and the frequency f_{FMR} of the FMR mode. (b) Calculated dispersion of magnon modes in the Py strip. m is the mode index.

Figure 4.2(a) shows a representative BLS spectrum recorded at $H_0 = 200$ Oe and without dc current ($I = 0$) that characterizes the magnons present in Py due to thermal fluctuations at room temperature $T_0 = 295$ K. The thermal spectrum exhibits a peak with the highest intensity in the frequency range $f = 4 - 5.5$ GHz, and a shallow high-frequency tail extending to 9 GHz. To elucidate the origin of these spectral features, we calculate the spin-wave dispersion in the Py strip (Figure 4.2(b)) by using the approach described in Section 2.3.1. The magnon spectrum is quantized in the direction transverse to the Py stripe, and is continuous in longitudinal direction. The allowed transverse components are $k_x = \pi m/w$, where w is the width of the Py strip, and positive integer m is the mode index. Because of the dependence of the BLS sensitivity on the wavevector, the fundamental mode $m = 1$ provides the largest contribution to the measured BLS spectrum, producing the peak observed at $f = 4 - 5.5$ GHz, as indicated in Figure 4.2(a) by the shaded area (the BLS response was calculated by using Equation 3.2). Despite the reduced BLS sensitivity to the higher-order modes, it allows measurements of the magnon population in a broad range of frequencies up to $f = 9$ GHz. Our measurements also provide an opportunity to distinguish between the FMR mode with $k_z = 0$ and the lowest-energy finite-wavevector magnon state at frequency f_{\min} (Figure 4.2(b)), as their frequency separation of about 0.8 GHz is significantly larger than the frequency resolution of the BLS technique. We use the spectrum shown in Figure 4.2(a) as a reference spectrum for the analysis presented below.

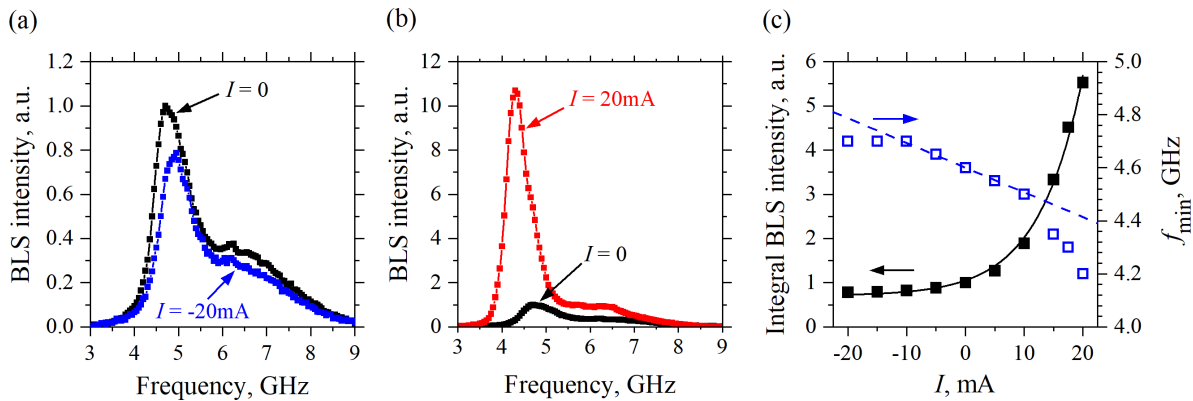


Figure 4.3 (a) and (b) Representative BLS spectra measured at $I = -20$ mA and 20 mA, respectively, together with the reference spectrum obtained at $I = 0$. (c) Current dependences of the BLS intensity integrated over the measured spectrum (solid squares) and of the frequency of the lowest-energy magnon state f_{\min} (open squares). Solid curve is a guide for the eye. Dashed line shows the calculated variation of f_{\min} due to the Oersted field of the current. The data were obtained at $H_0 = 200$ Oe.

The effects of the SOT on the magnon gas are illustrated in Figures 4.3(a) and 4.3(b) that show BLS spectra measured for $I = -20$ mA and 20 mA together with the reference thermal spectrum ($I = 0$). As can be seen from the data, at $I < 0$ the BLS intensity decreases and

the spectrum shifts to higher frequencies. In contrast, at $I > 0$ the BLS intensity increases, whereas the spectrum shifts to lower frequencies.

To quantify these changes, we plot the current dependence of the BLS intensity integrated over the measured spectrum and that of the lowest magnon frequency f_{\min} in Figure 4.3(c). The integral BLS intensity characterizes the total number of low energy magnons accessible to BLS, and its dependence on current is consistent with the expected reduction/increase of the magnon population by the SOT [121]. The dependence of f_{\min} on current can be attributed to the combination of the Oersted field of the current¹ and the nonlinear frequency shift (Section 2.5.1) due to the effect of the SOT and Joule heating on the magnon population. The calculated contribution of the Oersted field is shown in Figure 4.3(c) by the dashed curve. The experimental data closely follow this dependence at $|I| < 10$ mA, and deviate from it at larger current magnitudes. The deviation is larger at $I > 0$ than at $I < 0$. As Joule heating does not depend on the sign of current, we conclude that the total magnon population that determines the effective magnetization is significantly affected by the spin current.

To analyze the spectral distribution of spin current-driven magnon population, we compare the reference spectrum obtained at $I = 0$ with those obtained at finite currents. At $I = 0$, the magnon gas is in thermal equilibrium, with the temperature equal to the room temperature $T_0 = 295$ K and the chemical potential $\mu = 0$ (see discussion in Section 2.4). According to Equation 3.2, the measured BLS intensity is proportional to the reduced spectral density of magnons $\tilde{\rho}_0(f) = \tilde{D}(f)n_0(f)$, where $n_0(f)$ is the Bose-Einstein distribution (Equation 2.11). Since the energies of magnons studied in our experiment $hf \ll k_B T_0$, the Bose-Einstein distribution can be well approximated by the Rayleigh-Jeans law $n_0(f) = k_B T_0/hf$. At finite current, $\rho_I(f) = D(f)n_I(f)$ with a current-dependent distribution n_I . If the magnon gas is driven into a quasi-equilibrium state, this distribution can be written as $n_I = k_B T_{\text{eff}}/(hf - \mu)$, with effective temperature T_{eff} and chemical potential μ . The reduced density of states $\tilde{D}(f)$ is not expected to be influenced by the SOT, aside from the frequency shift discussed above. Therefore, the ratio of the BLS signals measured with and without current, or equivalently the frequency-dependent enhancement of the magnon population, is

$$R(f) = \frac{T_{\text{eff}}}{T_0} \frac{f}{f - \mu/h}. \quad (4.1)$$

This relation allows us to test whether the current-dependent magnon populations are well described by the quasi-equilibrium distribution, and extract the current-dependent values of T_{eff} and μ . Note that the roles of these parameters in Equation 4.1 are qualitatively different: variations of T_{eff} result in frequency-independent scaling of $R(f)$, whereas $\mu > 0$ produces a monotonically decreasing dependence $R(f)$ approaching 1 at large f .

¹The Oersted field produced by the driving current modulates H_0 and thus changes the Zeeman energy.

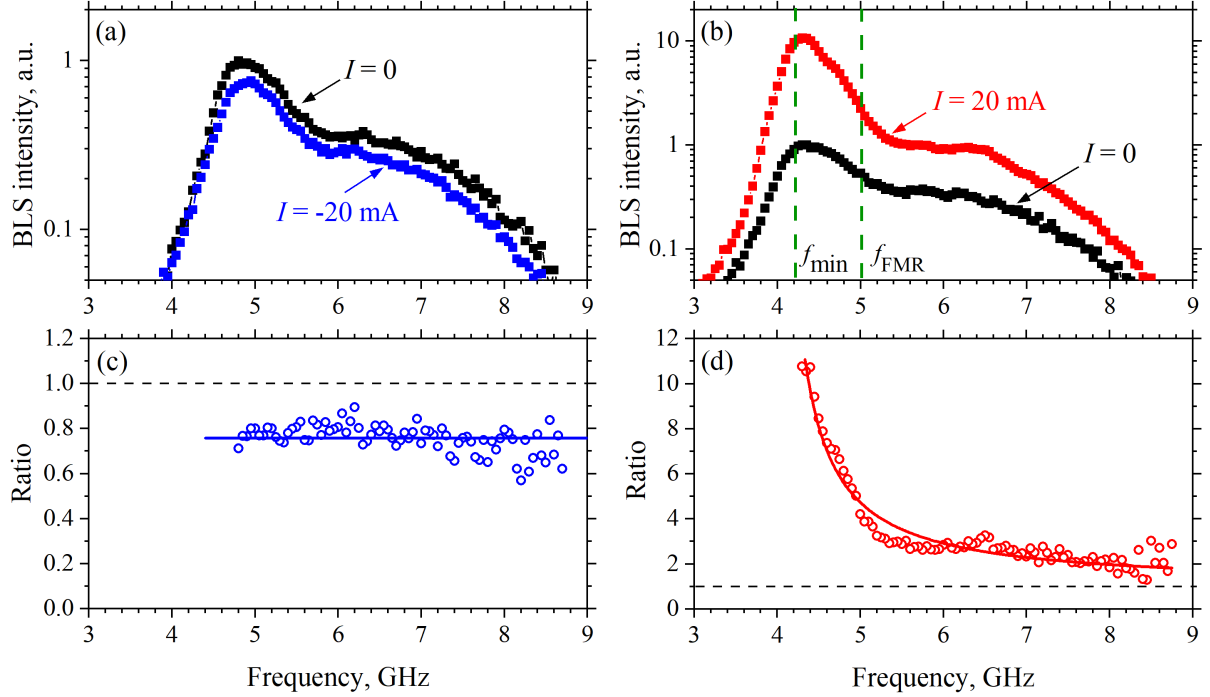


Figure 4.4 (a) and (b) BLS spectra recorded at $I = -20$ mA and 20 mA, respectively, together with the reference spectrum obtained at $I = 0$ shifted in frequency by the value determined from the data of Figure 4.3(c). Vertical dashed lines in (b) mark the frequency f_{\min} of the lowest-energy magnon state and the frequency f_{FMR} of the FMR mode. Note the logarithmic scale on the vertical axis. (c) The ratio of the spectra shown in (a). Solid line is the mean value of the ratio. (d) The ratio of the spectra shown in (b). Solid curve is the fit of the ratio by Equation 4.1, with $T = T_0$ and $\mu/h = 3.94$ GHz.

Figures 4.4(a) and 4.4(b) show on the log-linear scale the BLS spectra recorded at $I = -20$ and 20 mA, respectively, together with the reference spectrum obtained at $I = 0$ shifted in frequency by the value determined from the data in Figure 4.3(c). The data in Figure 4.4(a) illustrate that at $I < 0$, the magnon populations decrease approximately uniformly over the entire frequency range of the detected spectrum. In contrast, the increase of the population at $I > 0$ (Figure 4.4(b)) is most significant at the frequency f_{\min} of the lowest-energy magnon state, and it rapidly decreases with the increase in the frequency of magnons. We emphasize that the population increase at the frequency f_{FMR} of the FMR mode is smaller by more than a factor of two than that at f_{\min} .

Figures 4.4(c) and 4.4(d) show the ratio of the spectra obtained with and without current. For $I = -20$ mA (symbols in Figure 4.4(c)), this ratio is independent of frequency. According to Equation 4.1, this indicates that the dominant effect of spin current at $I < 0$ is the reduction of the effective temperature, $T_{\text{eff}} = (0.76 \pm 0.01) T_0 = 224 \pm 3$ K at $I = -20$ mA, whereas μ is zero within the measurement error. The frequency-dependent enhancement of the magnon population at $I = 20$ mA (symbols in Figure 4.4(d)) is also well described by Equation 4.1. In this case, a good fit is achieved with $T_{\text{eff}} \approx T_0$, and the effective chemical

potential in the frequency units $\mu/h = 3.94 \pm 0.02$ GHz (solid curve in Figure 4.4(d)).

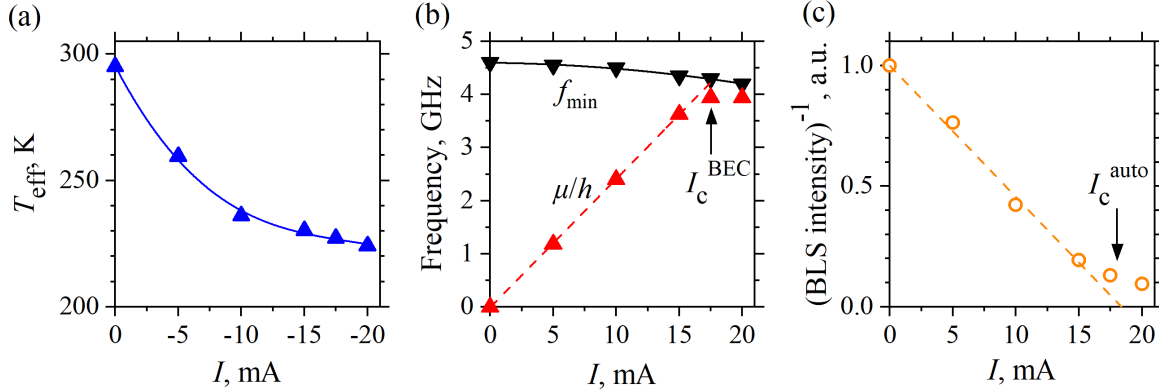


Figure 4.5 (a) Current dependence of the effective temperature of the magnon gas at $I < 0$. Curve is a guide for the eye. (b) Current dependence of μ/h (point-up triangles) and of the frequency of the lowest-energy magnon state f_{min} (point-down triangles) at $I > 0$. Solid curve is a guide for the eye. Dashed line is the linear fit at small currents, with I_C^{BEC} marking the extrapolated value of current, at which the formation of magnon BEC is expected. (c) The inverse BLS intensity at f_{min} vs current. Dashed line is the linear fit at small currents, with I_C^{auto} marking the extrapolated value of current, at which the onset of coherent magnetization auto-oscillations is expected.

Figures 4.5(a) and 4.5(b) summarize the results of the same analysis performed for different currents. The decrease of the effective temperature with increasing magnitude of $I < 0$ (Figure 4.5(a)) gradually saturates at large currents, which can be attributed to Joule heating that competes with the effects of spin current. At $I > 0$, the effective chemical potential increases linearly up to $I = 15$ mA (Figure 4.5(b)), reaching 80% of hf_{mA} at this current. Thus, our results show that, at $I < 0$, the dominant effect of the spin current is the variation of the effective temperature, while at $I > 0$, the dominant effect is the change of the chemical potential. We note that this does not indicate that the chemical potential is exactly equal to zero at negative currents or that the effective temperature remains exactly equal to the room temperature at positive currents. Instead, we can only ascertain that the variation of these parameters is too small to be reliably determined from the experimental data.

Extrapolating the linear dependence of the chemical potential (dashed line in Figure 4.5(b)) to larger currents, one would expect that it reaches the energy of the lowest magnon state at $I = I_C^{\text{BEC}} \approx 17.5$ mA, which should result in the formation of the BEC of magnons. Instead, the growth of μ rapidly saturates at $I > 15$ mA. This result is consistent with the previous studies (see discussion in Section 2.8), which showed that single-frequency current-driven magnetization dynamics cannot be achieved by injection of spin current into an extended region of the magnetic film, due to the onset of nonlinear damping that suppresses the population of low-energy magnon states [121]. Thus, this experimental observation suggests a relation between the current-induced variation of the effective chemical potential and the current-induced magnetic auto-oscillations.

To elucidate this relation further, we compare the critical current I_C^{BEC} determined from the condition $\mu/h = f_{\min}$ (Figure 4.5(b)) with the current I_C^{auto} corresponding to the onset of coherent magnetic auto-oscillations. According to Equations 2.15, the inverse of the magnon spectral density $\rho(f, I)$ should exhibit a linear dependence on current, extrapolating to zero at $I = I_C^{\text{auto}}$. Since the BLS intensity is proportional to $\rho(f, I)$, the value of I_C^{auto} can be determined from the analysis of the inverse BLS intensity. As expected, this quantity linearly depends on current (Figure 4.5(c)) with the extrapolated intercept at $I_C^{\text{auto}} \approx 18 \text{ mA}$ close to $I_C^{\text{BEC}} \approx 17.5 \text{ mA}$, confirming a connection between SOT-driven auto-oscillations and magnon BEC.

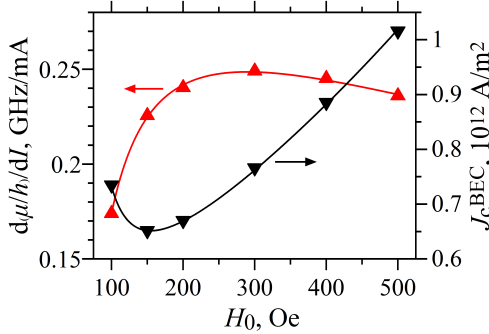


Figure 4.6 Static-field dependences of $d(\mu/h)/dI$, the efficiency of SOT-driven chemical potential variation in frequency units (point-up triangles), and of J_C , the critical current density in Pt at which the chemical potential is expected to reach the energy of the lowest magnon state (point-down triangles). Curves are guides for the eye.

Finally, we analyze the effects of the static magnetic field H_0 on the spin current-driven variations of the effective chemical potential. Measurements similar to those discussed above were performed at fields ranging between 100 and 500 Oe. While the observed behaviors remained similar over the entire field range, the efficiency of the chemical potential variation by the spin current strongly depended on field. Since the dependence $\mu(I)$ is linear at moderate $I > 0$ (dashed line in Figure 4.5(b)), the spin-current efficiency can be characterized by the slope $d(\mu/h)/dI$, as shown by the point-up triangles in Figure 4.6. It rapidly increases with increasing small field, plateaus at $H_0 = 300 \text{ Oe}$, and gradually decreases at larger fields. By extrapolating the linear dependence, we determine the critical electrical current density J_C^{BEC} in Pt, at which the chemical potential would reach the energy of the lowest magnon state in the absence of nonlinear damping and magnon BEC would form (point-down triangles in Figure 4.6). This dependence reaches a minimum at $H_0 = 150 \text{ Oe}$, and linearly increases at larger fields. We note that a similar dependence has been previously observed for the critical current densities J_C^{auto} corresponding to the onset of coherent auto-oscillations in SOT oscillators [68]. Moreover, the typical values of J_C^{auto} are very close to the values of J_C^{BEC} extrapolated from our measurements. These observations serve as additional

confirmation of a close relation between current-induced magnetization auto-oscillations and BEC of magnons.

4.1.4 Conclusions

In conclusion, our results provide answers to both questions posed in the motivation section:

- *What is the distribution of magnons excited by the SOT?* Figure 4.4(b) shows the spectral distribution of spin current-driven magnon population. The enhancement of the magnon population is most significant at low frequencies and rapidly decreases with the increase in the frequency of magnons. The data clearly demonstrate that the lowest-energy state is predominantly overpopulated due to the injection of the pure spin current, thus resolving the long-standing debate in the studies of spin current-induced effects.
- *Does the magnon distribution correspond to a quasi-equilibrium state that can be described by the effective thermodynamic characteristics?* Yes, our results provide direct spectroscopic evidence that the SOT drives a magnon gas into a quasi-equilibrium state that can be described by the Bose-Einstein statistics. The magnon population function is characterized either by an increased effective chemical potential or by a reduced effective temperature, depending on the spin current polarization (Figures 4.5(a) and 4.5(b)). In the former case, the chemical potential can closely approach, at large driving currents, the lowest-energy magnon state, indicating the possibility of spin current-driven Bose-Einstein condensation. Our findings also provide support for the theoretically proposed mechanism for formation of current-induced magnetization auto-oscillations via the Bose-Einstein condensation of magnons [157–159].

4.2 Instability of SOT-driven magnon condensates

4.2.1 Motivation

One of the results of the previous section is that SOT-driven Bose-Einstein condensation of magnons cannot be achieved when a spin current is injected into an extended region of a magnetic film. The reason is the onset of nonlinear damping at large currents, which suppresses the formation of a condensate. One way to reduce nonlinear damping is to utilize local injection of spin current that results in frequency-dependent magnon radiation losses (see Section 2.8). Therefore, we modify the design of the system discussed in the previous

section to enable radiation losses and study its SOT-induced magnetization dynamics. The results presented below were published in *Applied Physics Letters* 114, 042403 (2019).

4.2.2 Studied system

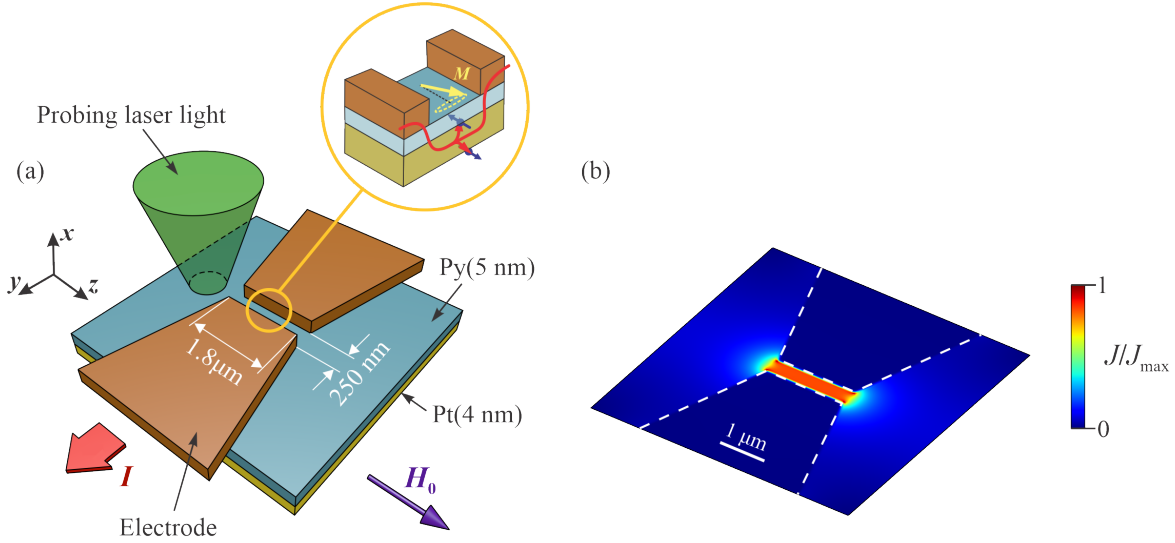


Figure 4.7 (a) Schematic of the experiment. The inset illustrates the local injection of the spin current into the Py layer in the nano-gap between the electrodes. (b) Normalized calculated distribution of the driving current density in the plane of the Pt layer.

Figure 4.7(a) shows the layout of the test devices. They are based on a bilayer formed by a 4 nm-thick Pt and a 5 nm-thick Py film, patterned into a square with the side of 5 μm. Two 80 nm-thick Au electrodes separated by a 250 nm-wide gap are fabricated on top of the bilayer. The electrodes are patterned into a trapezoidal shape converging to a 1.8 μm-wide base at the gap. A dc current I is applied between the electrodes. Because of the large difference between the sheet resistances of the electrodes and the Py/Pt bilayer, the electric current in the Py/Pt bilayer is confined predominantly to the region in the gap between the electrodes (Figure 4.7(b)). As a result, the spin current generated due to the SHE in Pt, is injected locally into the Py layer (inset in Figure 4.7(a)), defining the active device area.

The Py thickness was chosen to be 5 nm to prevent destruction of the samples due to electromigration and overheating, as current spreading in the device plane results in high operating current densities. However, we note that except for a reduced thickness of the Py layer and a modified geometry of the spin current injection, the system shown in Figure 4.7 is conceptually similar to that studied in the previous section (see Figure 4.1) because:

- The internal static magnetic field and the static magnetization are uniform in the active device area due to the large aspect ratio of the Py square.

- The driving current produces a relatively small and uniform Oersted field in the nano-gap region that results in negligibly small distortions of the spin-wave spectrum.

4.2.3 Results and discussion

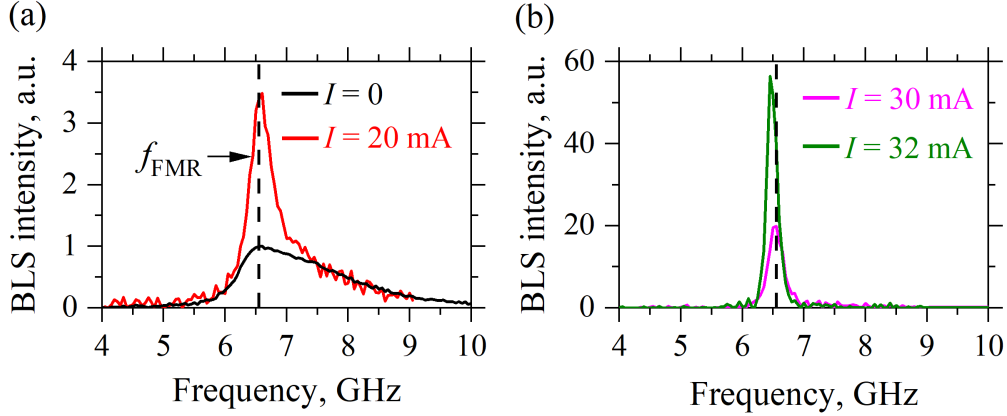


Figure 4.8 BLS spectra measured at the labeled values of the driving current. Vertical dashed lines mark the FMR frequency f_{FMR} . The data were obtained at $H_0 = 500 \text{ Oe}$.

Figures 4.8(a) and 4.8(b) show the BLS spectra recorded at different values of current I , with the probing spot positioned in the center of the gap between the electrodes. At $I = 0$, the BLS spectrum reflects incoherent thermal magnons in the Py film (Figure 4.8(a)). In the studied 5 nm-thick Py film, the lowest magnon frequency is only about 10 MHz lower than the FMR frequency f_{FMR} . Such a small spectral separation is below the frequency resolution of the BLS technique. Therefore, we assume that the thermal spectrum shown in Figure 4.8(a) has the maximum intensity at f_{FMR} . At $I > 0$, the thermal fluctuations are enhanced and a narrow peak gradually emerges in the spectrum (Figure 4.8(a)). This peak grows with increasing current, while its frequency slightly decreases due to the nonlinear frequency shift (Figure 4.8(b)).

Figure 4.9(a) shows the inverse of the measured BLS intensity as a function of driving current I . As expected (see discussion in Section 4.1), the data exhibit a linear dependence on current, extrapolating to zero at $I_C \approx 33 \text{ mA}$. Thus, at $I = I_C$, one can expect a transition to a single-mode auto-oscillation regime and, according to the results of the previous section, a formation of magnon BEC. Instead, as soon as the driving current reaches the critical value, a second peak with the frequency significantly below f_{FMR} appears in the spectrum (Figure 4.9(b)), indicating that the system actually makes a transition to a two-mode auto-oscillation regime. At $I > I_C$, the intensities of both the high-frequency (HF) and the low-frequency (LF) peaks increase, and the LF peak starts to dominate at large currents.

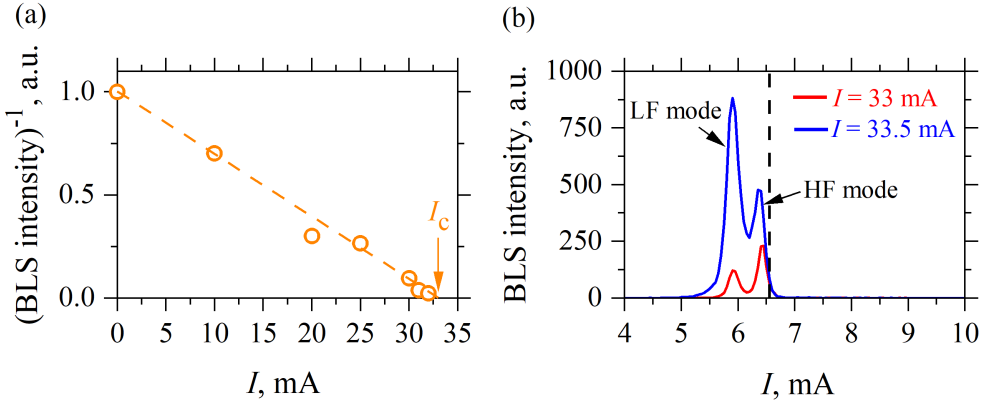


Figure 4.9 (a) Current dependence of the inverse BLS intensity at f_{FMR} . Dashed line is the linear fit of the data. I_C marks the extrapolated value of current, at which the onset of coherent magnetic auto-oscillations is expected. (b) BLS spectra measured at the labeled values of the driving current. Vertical dashed line marks the FMR frequency. The data were obtained at $H_0 = 500$ Oe.

To elucidate the nature of the observed modes, we analyze the dependences of their peak intensities and central frequencies on current (Figures 4.10(a) and (b)). The intensity of the LF mode (open symbols in Figure 4.10(a)) is significant even at the critical current, while its frequency (open symbols in Figure 4.10(b)) is far below the FMR frequency f_{FMR} . These results demonstrate that the LF mode does not have a counterpart in the linear spin-wave spectrum but is instead abruptly spontaneously formed at the auto-oscillation onset, which is one of the essential characteristics of a nonlinear spin-wave bullet.² Thus, we conclude that the LF mode is the bullet mode.

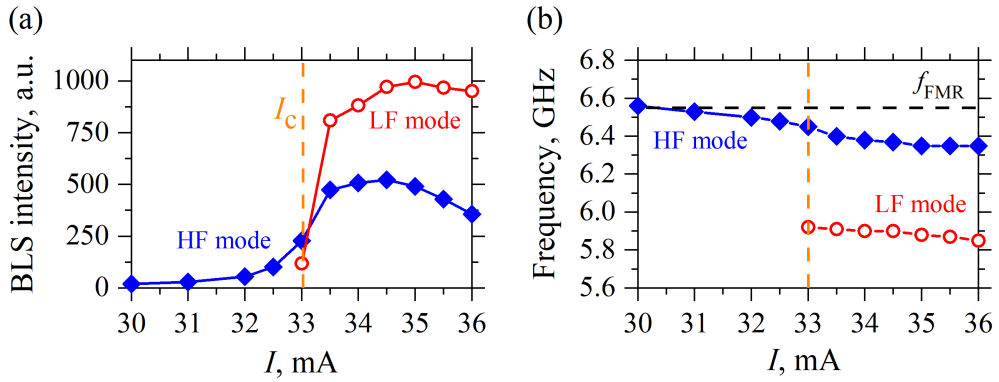


Figure 4.10 (a) Peak intensities and (b) center frequencies of the high-frequency (HF) and low-frequency (LF) modes vs current I . Vertical dashed lines marks the critical current I_C . Horizontal dashed line in (b) marks the FMR frequency f_{FMR} . The data were obtained at $H_0 = 500$ Oe.

After establishing the nature of the LF mode, we discuss the nature of the HF mode. As the current is increased, the intensity of the HF mode (solid symbols in Figure 4.10(a))

²Nonlinear spin-wave bullets are self-localized dynamical solitons existing in in-plane magnetized ferromagnetic films [160, 161].

continuously evolves from the fluctuation background, while its frequency (solid symbols in Figure 4.10(b)) remains close to f_{FMR} and varies smoothly in the vicinity of I_{C} . These observations, together with the results of the previous section, suggest that the HF mode originates from the accumulation of magnons in the lowest-frequency state and might be magnon BEC. But how can one unambiguously prove it? According to the established criteria, the spontaneous emergence of coherence is one of the most prominent properties of BEC, and the most convincing way to demonstrate it is an experiment showing interference between two condensates. For atomic condensates this can be done by preparing two separate condensates with different wavevectors and bringing them to spatial overlap [162]. However, in the case of magnon BEC, there is no need to create two condensates. Since the lowest-frequency magnon state is doubly degenerated, the condensation simultaneously occurs at two non-zero values of the wavevector $k = \pm k_{\text{min}}$ (Figure 4.11(a)). The interference of these two components results in the formation of a real-space standing wave, as it has been previously demonstrated for magnon BEC driven by parametric pumping [163]. Therefore, if the HF mode is a magnon BEC, one should observe a stable standing wave pattern at the frequencies of the HF modes in the gap region.

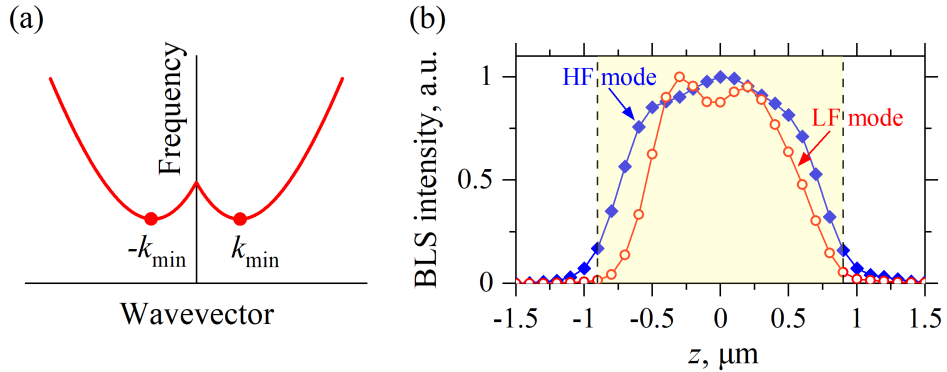


Figure 4.11 (a) Schematic of the spin-wave spectrum. Two magnon BECs are formed at two spectral minima with non-zero wavevectors $\pm k_{\text{min}}$. (b) Spatial profiles of the HF and LF modes, measured at $I = 34$ mA. The shadowed area shows the region of the nano-gap. $z = 0$ corresponds to the center of the gap. The data were obtained at $H_0 = 500$ Oe.

To test this hypothesis, we perform spatially resolved BLS measurements of the dynamic magnetization, by scanning the probing laser spot along the nano-gap. Figure 4.11(b) shows the normalized one-dimensional spatial profiles of the dynamic magnetization, recorded at the frequencies of the LF and the HF modes, at $I = 34$ mA. Both modes are localized in the nano-gap region, consistent with the data in Figure 4.10(b), which show that at finite currents their frequencies are always smaller than f_{FMR} in the surrounding extended Py film, preventing radiation of propagating spin waves away from the gap. We note that the LF mode is noticeably more localized than the HF mode. This can be associated with the nonlinear

self-localization of the bullet mode, reducing its dimensions below the size of spin current injection region.

The profile of the LF mode exhibits a local minimum in the center of the gap that can be attributed to the inversion of the static magnetization direction in the center of the bullet, which is a typical feature for this dynamical mode [164]. The profile of the HF mode has a cosine-like shape and exhibits no signs of the anticipated standing wave pattern. We associate this discrepancy with the fact that the intense magnetization precession in the bullet mode produces a strong, spatially inhomogeneous and time-varying dipolar field. This dipolar field modifies the internal magnetic field in the gap region, as a result of which the formation of a stable standing wave is not possible.

Finally, we note that, according to the previous studies, two auto-oscillation modes compete for the same source of the angular momentum provided by the spin current, and are thus mutually exclusive, unless they are spatially separated [165]. Therefore, the simultaneous presence of two spectral peaks in our experiments likely indicates random hopping of the system between them [166]. These behaviors can be also interpreted in terms of unstable magnon condensation. Because of the attractive magnon-magnon interaction, the initial condensation of magnons at the point of phase space corresponding to the lowest-frequency magnon state – the formation of the HF mode – is followed at sufficiently large magnon densities by the spatial collapse of the condensate, resulting in the formation of the LF bullet mode corresponding to the condensation in the real space. The latter also eventually collapses because of the significant mismatch between the size of the active area and the natural size of the self-localized bullet³. We also note that measurements similar to those discussed above were performed at fields ranging between 250 and 2000 Oe, and the results remained the same.

4.2.4 Conclusions

In conclusion, we have experimentally studied the SOT-driven magnetization dynamics in a specially designed system, whose geometry enables local injection of spin current without a significant current-induced distortion of the spin-wave spectrum. Since nonlinear damping is reduced in the studied system, the formation of magnon BEC can be expected based on the results of the previous section. However, the experimental data demonstrate that two auto-oscillation modes are simultaneously excited. By analyzing the oscillation characteristics of these modes, we find that one of them (the HF mode) evolves from the lowest-frequency

³The spatial characteristics of the stable bullet mode are generally determined by the nonlinear properties of the medium, and are expected to be almost independent of the size of spin current injection region [160]. Based on the results of [55], one expects that the bullet mode should shrink to dimensions below 100 nm, inconsistent with the experimental profile in Figure 4.11(b). This discrepancy indicates that the bullet mode is unstable in the studied devices.

magnon state, while the other one (the LF mode) is the nonlinear spin-wave bullet. Our results indicate that the HF mode is unstable and its spatial collapse results in the formation of the LF mode. This instability does not allow us to unambiguously conclude whether the HF mode is a magnon BEC or not. The observed behaviours provide an insight into mechanisms underlying the formation and the stability of nonlinear magnon condensates.

Chapter 5

Tailored PMA as a way to control nonlinear damping

5.1 Case of large PMA

5.1.1 Motivation

In the previous chapter we have experimentally demonstrated that that nonlinear damping suppresses the formation of SOT-driven magnon BEC. We emphasize that the same mechanism prevents excitation of coherent magnetization oscillation by the SOT in spatially extended systems (see discussion in Section 2.8), which drastically limit the generated power and coherence of SOT oscillators, as well as their geometries [68]. Note that the onset of nonlinear damping also does not allow one to achieve complete compensation for propagation losses of spin-waves [70]. Therefore nonlinear damping should be considered a fundamental phenomenon that strongly hinders further developments in the field of spin-orbit-torque magnonics.

As mentioned in Section 2.8, the standard approach for reducing nonlinear damping is based on the utilization of frequency-dependent radiation losses. However, this approach is clearly unable to resolve all the issues, since it requires that the active region of a SOT-based device is limited to nanoscale, and often leads to complex dynamic behaviors (see, e.g., Section 4.2). Consequently, new methods to overcome the adverse effects of nonlinear damping have to be developed.

One possible option is to magnetize the active magnetic layer perpendicular to its plane. In contrast to the in-plane magnetized configuration discussed in Section 2.2, in the out-of-plane geometry, the spin-wave dispersion is isotropic and does not show minima at $k \neq 0$ and therefore does not support the resonant four-magnon scattering [1]. However, large magnetic fields are required to overcome the demagnetizing field of the magnetic film and magnetize

it to saturation in the out-of-plane direction, which makes this approach technologically impractical. This challenge can be addressed by utilizing magnetic materials with sufficiently large PMA. PMA materials are of great technological importance and they have been intensively explored for various magnetic applications [167]. However, their suitability for the implementation of magnonic devices driven by the SOT remains largely untested. In this section, we experimentally study SOT oscillators based on magnetic multilayers with PMA. The results presented below were published in *Applied Physics Letters* 111, 032405 (2017) and *Physical Review B* 96, 224419 (2017).

5.1.2 Studied system

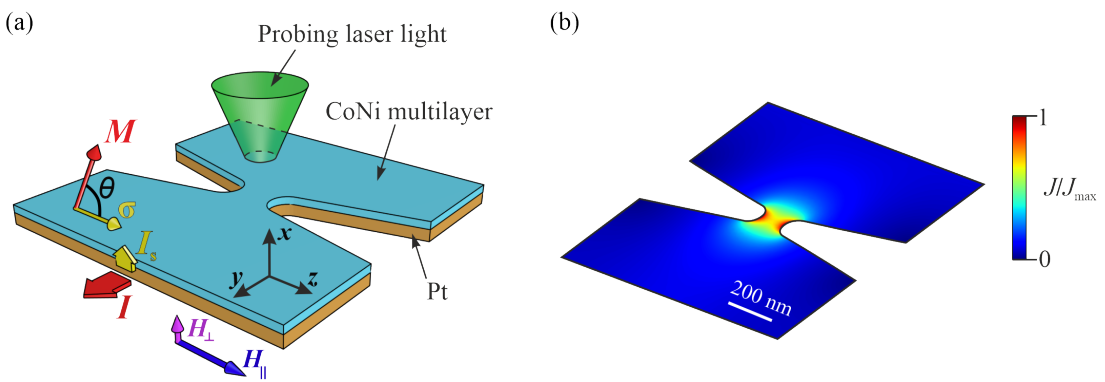


Figure 5.1 (a) Schematic of the experiment. (b) Normalized calculated distribution of the driving current density in the plane of the Pt layer.

The tested devices are based on a Pt(5)/[Co(0.2)/Ni(0.8)]₄ magnetic bilayer with PMA (Figure 5.1(a)). Here, thicknesses are in nanometers. The bilayer is patterned into the shape of a bow-tie nanoconstriction with the width of 100 nm, the opening angle of 22°, and the radius of curvature of about 50 nm. The dc electric current I flowing in the plane of the multilayer is converted by the SHE in Pt into an out-of-plane spin current I_s with spin polarization σ oriented in-plane, perpendicular to the direction of current I .

In the studied device geometry, the abrupt narrowing of the Pt layer in the nanoconstriction region causes a strong local increase of the electric current density J (Figure 5.1(b)). Since the spin current injected into the CoNi multilayer is proportional to the current density in Pt, this region of large current density defines the active device area, where the SOT is sufficiently strong to completely compensate the damping and cause the magnetization instability. While the current density rapidly decreases with increasing distance from the nanoconstriction, considerable SOT effects are expected outside the active device area. For instance, the current density at the distance of 0.5 μ m from the nanoconstriction center is about 5% - 7% of that at the center. Thus, at currents significantly above the instability

threshold, damping can be almost completely compensated for a relatively large region of the magnetic film.

The parameters of the multilayer - the saturation magnetization $4\pi M_s = 6150$ G and the out-of-plane magnetic anisotropy $K_a = 2.3$ Merg/cm³ - were determined from independent measurements utilizing vibrating-sample and magneto-optical Kerr-effect magnetometries. According to Equation 2.7, the effective PMA field is $H_{\text{PMA}} \approx 10$ kOe, which is much larger than the effective field associated with the dipolar anisotropy $H_{\text{dem}} = 4\pi M_s \approx 6$ kOe. Due to the dominance of PMA, the magnetization is oriented out-of-plane if no external magnetic field is applied.

As shown in Figure 5.1(a), the polarization σ of a spin current injected into CoNi is parallel to the z -direction. Under these conditions, the effects of the SOT vanish if M is exactly perpendicular to the plane of the magnetic multilayer (see Equation 2.13). Therefore, to achieve current-induced instability in the studied CoNi film with PMA, we apply an in-plane static magnetic field $H_{\parallel} = 1000 - 2000$ Oe to tilt the magnetization with respect to the film normal. Additionally, to prevent magnetization switching by the SOT, we apply a small constant out-of-plane magnetic field $H_{\perp} = 200$ Oe.

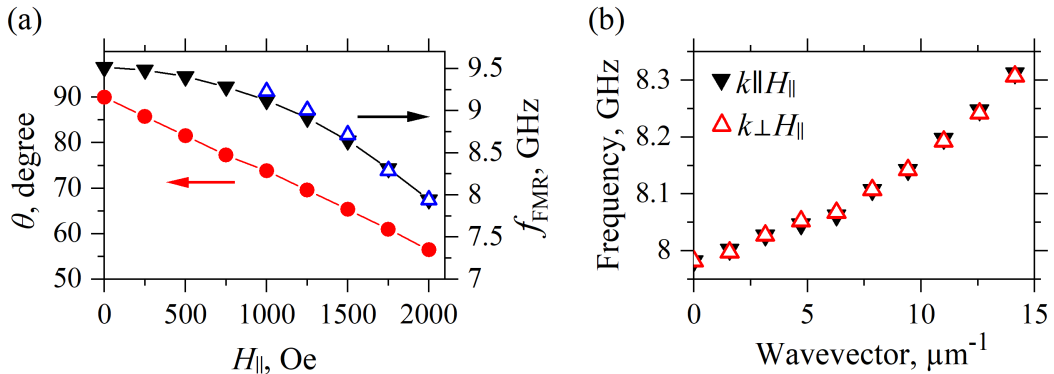


Figure 5.2 (a) Calculated static-field dependence of the out-of-plane angle of the equilibrium magnetization (circles) and of the FMR frequency f_{FMR} (point-down triangles). Point-up triangles show f_{FMR} determined from the BLS measurements of thermally excited magnons. Curves are guides to the eye. (b) Calculated spectrum of spin waves in the [Co/Ni] multilayer magnetized by the in-plane field of 2000 Oe.

Before studying the SOT-induced magnetization dynamics, we characterize the static and the dynamic magnetic properties of the CoNi multilayer by performing micromagnetic simulations using the Mumax3 software. As shown in Figure 5.2(a), increasing the in-plane field H_{\parallel} from 0 to 2000 Oe results in the reduction of the magnetization angle θ counted relative to the z -axis (circles) from 90° to 57° , while the FMR frequency f_{FMR} in the CoNi multilayer (point-down triangles) decreases from 9.5 GHz to about 8 GHz. The validity of the simulations is confirmed by the good agreement of the calculated FMR frequencies with those obtained from independent measurements (point-up triangles in Figure 5.2(a)).

Despite significant tilting of the magnetization, the form of the dispersion relation of spin waves remains similar to that for the out-of-plane magnetized films even at the largest applied in-plane field $H_{\parallel} = 2000$ Oe (Figure 5.2(b)). The dispersion is isotropic in the film plane. In contrast to ferromagnetic films with the in-plane magnetization discussed in Section 2.2, there are no finite- k spin wave modes that are degenerate with the uniform $k = 0$ mode. As mentioned above, this is particularly important for the SOT-induced auto-oscillations, since the spin-wave degeneracy is known to facilitate nonlinear magnetic damping.

5.1.3 Results and discussion

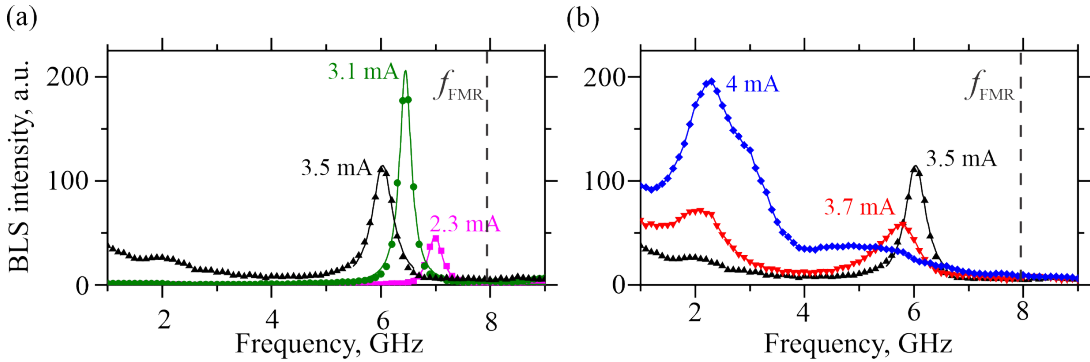


Figure 5.3 BLS spectra of current-induced magnetization oscillations, measured at the labeled values of the driving current. Curves are guides to the eye. Vertical dashed lines mark the FMR frequency f_{FMR} . The data were obtained at $H_{\parallel} = 2000$ Oe.

Figures 5.3(a) and 5.3(b) show the BLS spectra measured at $H_{\parallel} = 2000$ Oe, with the probing laser spot positioned at the center of the nanoconstriction. The onset of the SOT-induced auto-oscillations is signified by the emergence of an intense and narrow spectral peak at $I = I_C = 2.3$ mA. The oscillation frequency is close to the FMR frequency f_{FMR} . The auto-oscillation peak rapidly grows with increasing current, reaching a maximum intensity at $I = 3.1$ mA. At larger currents, the peak starts to broaden, while its intensity decreases. Simultaneously, broad noiselike spectral features emerge at frequencies below 3 GHz, indicating that the system transitions to a new regime characterized by complex magnetization dynamics. At currents above 3.5 mA, this broad spectrum evolves into a well-defined low-frequency (LF) oscillation peak with a center frequency of about 2 GHz, while the peak corresponding to the high-frequency (HF) mode gradually disappears.

Figure 5.4(a) show the current dependencies of the peak intensities for the HF and the LF modes. Both modes are characterized by a "soft" auto-oscillation onset - a gradual increase of intensity with increasing driving current [118]. The intensity of the HF mode saturates and starts to decrease around $I = 3.1$ mA, while the intensity of the LF mode exhibits a rapid increase. These behaviors can be attributed to the competition between the modes for the angular momentum supplied by the spin current.

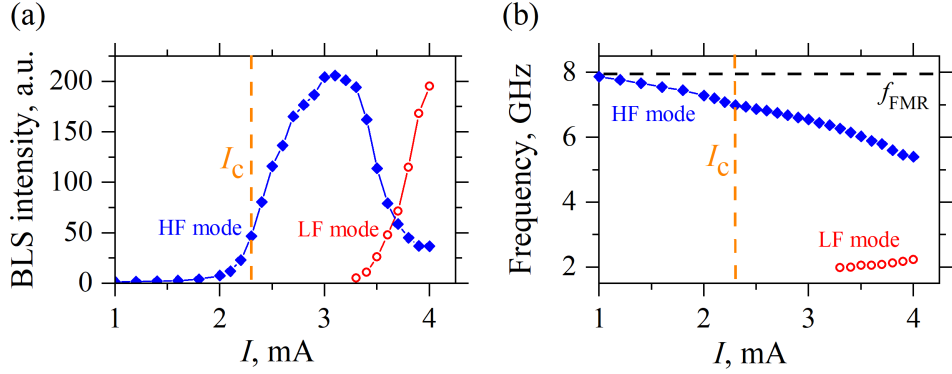


Figure 5.4 (a) Peak intensities and (b) center frequencies of the high-frequency (HF) and low-frequency (LF) modes vs current I . Curves are guides to the eye. Vertical dashed lines marks the critical current I_C . Horizontal dashed line marks in (b) marks the FMR frequency f_{FMR} . The data were obtained at $H_{\parallel} = 2000$ Oe.

The current dependencies of the central frequencies of the modes (Figure 5.4(b)) are completely different. The frequency of the HF mode (solid symbols in Figure 5.4(b)) is very close to the FMR frequency f_{FMR} at small currents $I < 1.5$ mA. According to the results of Section 4.1, the injection of pure spin current results in the accumulation of magnons in the state with the lowest frequency. Since, in contrast to films with in-plane magnetization, the FMR mode is the lowest-frequency spin-wave mode in the studied system (Figure 5.2(b)), we conclude that the HF mode evolves from the FMR mode of the CoNi multilayer.

It is important to note that the frequency of the HF mode decreases by 1.6 GHz when the driving current is increased from the critical current $I_C = 2.3$ mA to 4 mA. We emphasize that this decrease is about an order of magnitude larger than the current-dependent frequency variation typically observed in SOT devices with in-plane magnetization (see, e.g., Figure 4.10(b)). Since this frequency variation originates from the increase in the magnetization precession amplitude (Section 2.5.1), one can estimate the corresponding precession angle. Our micromagnetic simulations show that to achieve nonlinear frequency shift of 1.6 GHz, the precession angle must increase by more than 20°. Such large amplitudes of the magnetization precession cannot be achieved in the in-plane magnetized devices, because the nonlinear magnon scattering mechanism limits the precession amplitude (Section 2.5.2). We note that the observed strong variation of the auto-oscillation frequency with current is advantageous for applications requiring a large tunability of the frequency of the generated microwave signals.

In contrast to the HF mode, the frequency of the LF mode (open symbols in Figure 5.4(b)) is far below the FMR frequency and almost current-independent, which is one of the distinguishing characteristics of a magnetic droplet.¹ To elucidate the nature of the LF

¹Magnetic droplets are dynamical solitons existing in magnetic systems with large PMA [168–170]. Droplets have many characteristics similar to spin-wave bullets discussed in Section 4.2, but the essential

mode, we perform additional Mumax3 simulations taking into account the effects of SOT. The magnitude of SOT is assumed to be proportional to the current density in Pt (Figure 5.1(b)). We also take into account the nonuniform Oersted field of the current, determined from the calculated current distribution.

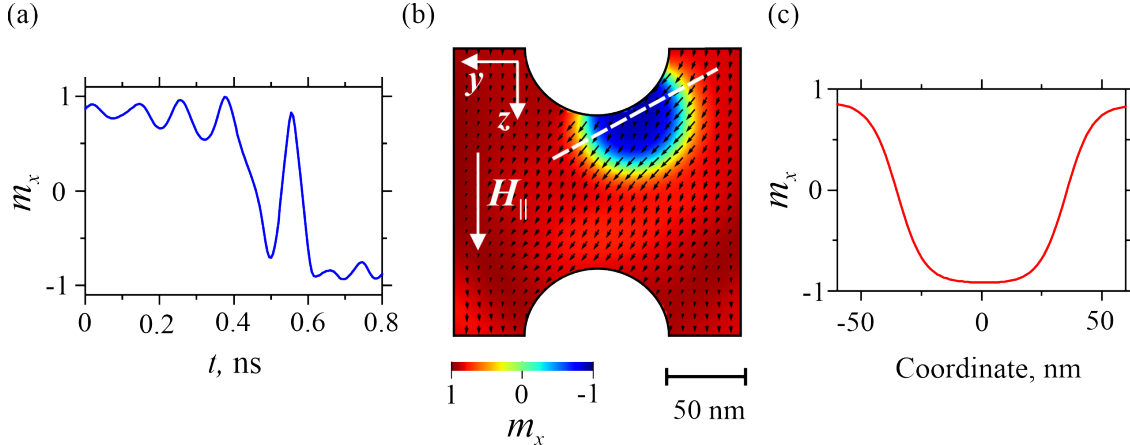


Figure 5.5 (a) Calculated time dependence of the normalized out-of-plane magnetization component m_x , demonstrating the development of the current-induced instability. The current is applied starting at $t = 0$. (b) Calculated spatial magnetization map at $t = 0.625$ ns, shortly after the droplet is nucleated. Arrows represent the in-plane magnetization component, and the colors represent its out-of-plane component m_x . (c) Profile of m_x along the dashed line in (b). Simulations were performed at $I = 5$ mA and $H_{\parallel} = 2000$ Oe.

Figure 5.5(a) illustrates the calculated time dependence of the normalized out-of-plane component of magnetization $m_x = M_x/M_s$ at $H_{\parallel} = 2000$ Oe, with current $I = 5$ mA applied starting at time $t = 0$. Under these conditions, the SOT-induced dynamical instability develops on the sub-nanosecond time scale. The component m_x initially starts to oscillate with the frequency close to the FMR frequency f_{FMR} and with a rapidly growing amplitude, and completely reverses at t slightly above 0.6 ns. This instability is observed at $I > I_C \approx 4.5$ mA, in a reasonable agreement with the characteristic currents in the experiment. As the current is reduced towards I_C , it takes an increasingly long time for the instability to develop, resulting in quasistable current-induced oscillations at frequencies close to f_{FMR} that resemble the HF mode observed in the experiment. However, since our task is to elucidate the nature of the LF mode, we limit our analysis to the large-current behaviors.

Figure 5.5(b) shows a snapshot of the spatial distribution of magnetization after its complete reversal, at $I = 5$ mA and $t = 0.625$ ns. Arrows in this map represent the projection of the magnetization on the film plane, while the color represents its out-of-plane component m_y . The magnetization distribution is typical for a droplet soliton [169]. The magnetization is nearly completely reversed in the droplet core, as can be also seen from Figure 5.5(c) showing the profile of m_x across the section indicated in Figure 5.5(b) by a dashed line. At

difference between them is that the magnetization in the droplet core can be nearly fully reversed.

the boundary of the core, all the magnetic moments are aligned in the same direction. The droplet is shifted to one of the edges of the nanoconstriction, due to the effect of the Oersted field of the driving current. A similar edge droplet was predicted for narrow magnetic nanowires [171].

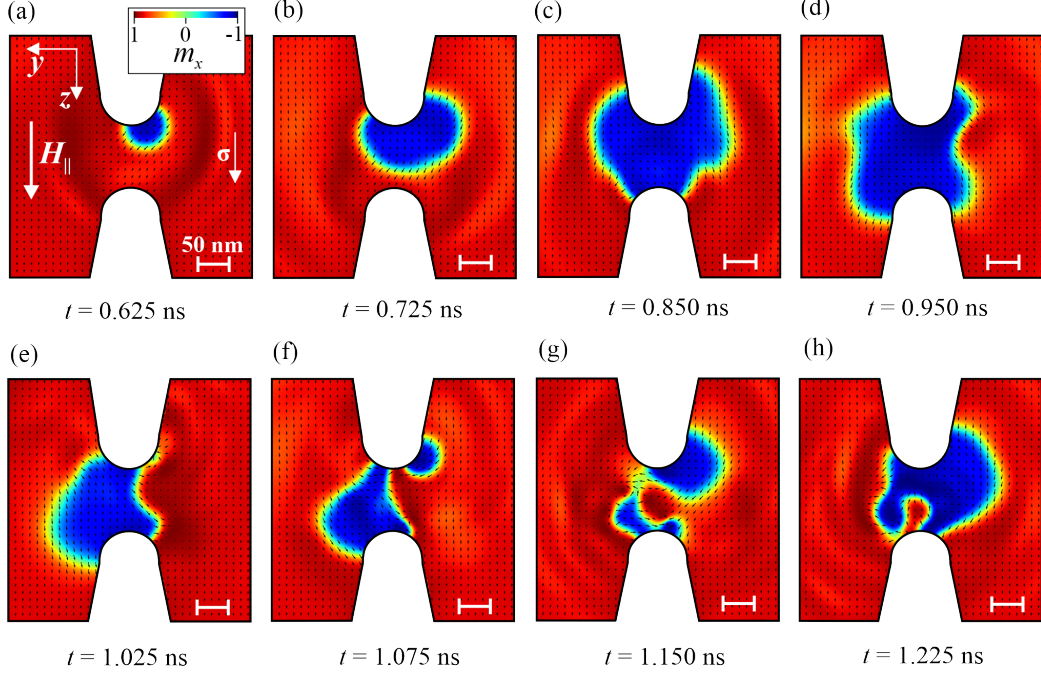


Figure 5.6 Temporal evolution of the nucleated droplet soliton, at the labeled instants of time t . The driving current is applied starting at $t = 0$. The arrows represent the in-plane magnetization component and the colors represent its out-of-plane component m_x . The simulations were performed at $I = 5$ mA and $H_{\parallel} = 2000$ Oe.

Snapshots obtained at different instants of time (Figure 5.6) illustrate the spatiotemporal dynamics of the nucleated droplet. As seen from Figures 5.6(a)-5.6(c), the droplet initially increases in size, while the magnetization at its boundary precesses in the counterclockwise direction. The expansion of the droplet is caused by the so-called effective spin-Hall field produced by STO [172]. This field is known to result in either expansion or shrinking of magnetic domains, depending on the orientation of the magnetization in the domain walls relative to the polarization σ of the spin current [173]. Therefore, the observed initial expansion of the droplet is produced by the same mechanism as the expansion of topologically trivial magnetic bubble domains driven by SOT [174]. The droplet is distinguished from the bubble domains by its dynamical nature. Because of the precession of the magnetic moments at the droplet boundary, the effective spin Hall field is time-dependent. As a result, the initial expansion of the droplet ends at $t \approx 0.850$ ns, when the magnetic moments at its boundary align approximately parallel to σ , and the effective spin-Hall field vanishes (Figure 5.6(c)). Further rotation of the magnetic moments leads to the inversion of the sign of the effective field, and the droplet starts to shrink (Figures 5.6(c)-5.6(e)). If the

magnetic moments in the droplet boundary precessed perfectly in-phase, the droplet would experience periodic “breathing” with a well-defined frequency, as observed in the previously demonstrated droplet oscillators [169]. In the studied nanoconstriction devices, the droplet dynamics is significantly more complex, as illustrated in Figures 5.6(e)-5.6(h). The dynamical complexity is associated with the inhomogeneous distribution of the effective field, which leads to the spatial variation of the precession phase, as can be clearly seen from the increasingly significant variations among the directions of arrows in Figures 5.6(c)-5.6(h). Because of these variations, different parts of the droplet experience different forces from the spin-Hall field, which perturbs the shape of the droplet, and results in complex spatiotemporal dynamics. This observation is in agreement with the experimental data, which show that at large driving currents, the spectra of the current-induced magnetization oscillations become very broad.

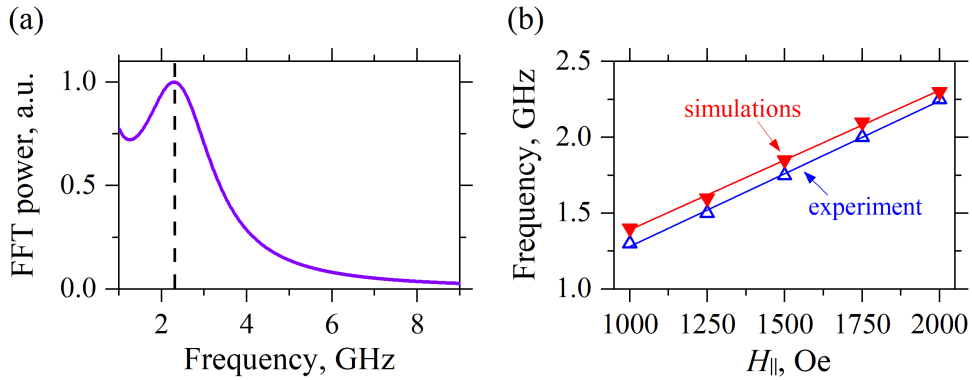


Figure 5.7 (a) Fourier spectrum of the time dependence of the spatially averaged out-of-plane magnetization component m_x , for the dynamics shown in Figure 5.6. Vertical dashed line indicates the central frequency of the spectral peak. (b) Dependence of the central frequency of the LF mode on H_{\parallel} , determined from the measurements (open symbols) and from the micromagnetic simulations (solid symbols). Lines are linear fits of the data.

To correlate the results of the simulation with the experiment, we calculate the Fourier spectrum² (Figure 5.7(a)) of the time dependence of the out-of-plane magnetization component m_x averaged over the $300 \times 300 \text{ nm}^2$ area³ shown in Figure 5.6. Despite the dynamical complexity, the calculated spectrum exhibits a pronounced peak, which is remarkably similar to the BLS spectrum measured at $I = 4 \text{ mA}$. In particular, its central frequency 2.30 GHz is very close to the experimental value 2.25 GHz. A good agreement of our simulations with the experimental observations allows us to unambiguously conclude that the observed LF mode is associated with the formation of a droplet soliton.

²To facilitate the comparison of the simulated spectrum with our measurements, we have convolved it with a Gaussian with the full width at half maximum of 100 MHz, corresponding to the frequency resolution of the measurement setup.

³The size of this area corresponds to the size of the area probed by μ BLS.

Analysis of the dependence of the frequency of the LF mode on the magnitude of the static in-plane magnetic field H_{\parallel} (Figure 5.7(b)) provides further support for this conclusion. The measured central frequency of the LF mode linearly increases from 1.3 GHz at $H_{\parallel} = 1000$ Oe to 2.25 GHz at $H_{\parallel} = 2000$ Oe. The observed linear dependence is consistent with the behaviors expected for the droplet soliton [169]. The dependence of the central peak frequency on field obtained from the simulations is in a good agreement with the experiment over the entire studied range of H_{\parallel} , supporting our interpretation of the LF mode as a magnetic droplet soliton.

Finally, we discuss the effects of the spatially extended injection of spin current produced by the SHE. Magnetic droplets are strongly dissipative excitations stabilized by the balance between anti-damping torque and natural damping [168]. In the studied nanoconstriction devices, the SOT magnitude does not abruptly vanish outside of the nanoconstriction area. The resulting spatial dimensions of the droplets can be as large as 200–300 nm in the nanoconstriction with the width of 100 nm used in our work. As shown above, this large size results in complex dynamics and an irregular shape of the droplet, which originate from the non-uniform distribution of the magnetization precession phase at its boundary. We emphasize that the spatial distribution of the precession phase can significantly affect the spatial characteristics of the droplet. For the uniform phase distribution, the effective spin-Hall field produces periodic expansion and shrinking of the droplet, as discussed above. However, if the precession phases are opposite at the opposing points at the droplet boundary, the spin-Hall field is expected to cause translational motion of the droplet, as was also shown for the magnetic skyrmions [174] where the direction of the magnetization rotates around the soliton boundary due to the Dzyaloshinskii-Moriya interaction (DMI) [52].

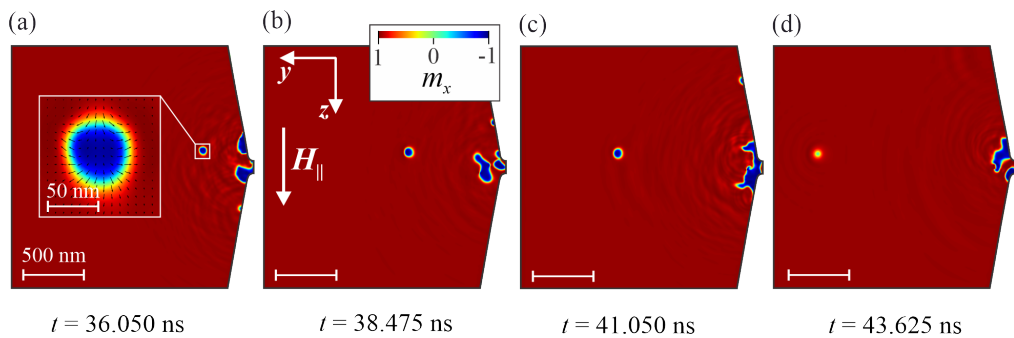


Figure 5.8 Calculated magnetization maps demonstrating the generation of a propagating droplet soliton, at the labeled instants of time t . The driving current is applied starting at $t = 0$. The colors represent the out-of-plane magnetization component m_x . Inset in (a) shows a magnified view of the propagating droplet. The simulations were performed at $I = 6$ mA and $H_{\parallel} = 1000$ Oe.

We do not expect sizable DMI effects for the studied system, because of the relatively large thickness of the CoNi multilayer. Nevertheless, our simulations indicate that nontrivial phase distributions enabling the SOT-induced translational motion of droplets can sponta-

neously form at sufficiently long times of the order of tens of nanoseconds. Figure 5.8(a) shows the spatial magnetization map obtained at $t = 36.050$ ns, with $I = 6$ mA applied starting at $t = 0$. In addition to the irregular-shaped droplet in the nanoconstriction region, a small circularly shaped droplet with dimensions of about 50 nm is located outside of the active area. The magnetization is pointing to the left at the left boundary of the small droplet, and to the right at its right boundary (inset in Figure 5.8(a)). Consequently, the droplet is expected to experience a net effective spin Hall field driving its directional motion, as confirmed by the snapshots in Figures 5.8(b)-5.8(d) for later instants of time. As seen from these data, the droplet is indeed moving to the left while shrinking in size, and is finally annihilated at the distance of more than 1.5 μ m from the nanoconstriction center. We emphasize that the moving droplet remains stable due to the non-vanishing SOT over its entire propagation path in the studied nanoconstriction device. While at large distances from the active area, the magnitude of SOT becomes too small to completely compensate the natural damping, it is still sufficiently large to maintain the stability of the nucleated droplet over a significant propagation distance. The generation of propagating droplets can be important for the implementation of novel devices for transmission and processing of information on the nanoscale. The controllability of the droplet generation process can be improved by utilizing nanopatterned material systems where a combination of DMI and geometric boundary effects favors the spatial variation of the precession phase necessary for the extraction of the droplet from the nucleation area, and for its directional motion. By optimizing the geometry of the samples, one can also control the magnitude and the distribution of the SOT outside of the active nanoconstriction area, to increase the propagation distance of the generated droplets.

5.1.4 Conclusions

In conclusion, we have experimentally demonstrated SOT oscillators based on magnetic multilayers with PMA that enable excitation of two dynamical modes at significantly different frequencies. The high-frequency (HF) mode is stable at low driving currents, while the low-frequency (LF) mode is additionally excited at larger currents and becomes increasingly dominant with increasing current. Due to large PMA in the studied system, the degeneracy of the spin-wave spectrum is lifted, enabling large magnetization precession amplitudes not limited by the nonlinear magnon scattering processes. This has following consequences:

- First, a very high tunability of the frequency of the HF mode by electrical current becomes possible, making the demonstrated devices promising for applications in high-speed integrated microwave circuits.
- Second, the absence of nonlinear limiting phenomena allows a complete local reversal of the magnetization necessary for the formation of a droplet soliton (the LF mode).

Moreover, our micromagnetic simulations indicate that in addition to the stationary droplets, propagating droplets can be also generated in the studied system, which can be utilized for the information transmission in magnonic applications.

5.2 Case of moderate PMA comparable with the dipolar anisotropy

5.2.1 Motivation

In the previous section, we have showed that SOT oscillators with strong PMA exhibit large magnetization precession amplitudes due to the reduced nonlinear damping. However, the absence of the limiting nonlinearity and large uniaxial magnetic anisotropy leads to the bistability of the system. As a result, the studied nanoconstriction devices exhibit erratic dynamical behavior at large driving currents, which is rather challenging to control experimentally. In this section, we demonstrate a different approach to minimizing the nonlinear damping that provides stable, large-amplitude SOT-induced auto-oscillations. The results presented below were published in *Nature Communications* 10, 5211 (2019).

5.2.2 Studied system

Our hypothesis is that nonlinear spin-wave coupling in in-plane magnetized films is predominantly determined by the ellipticity of magnetization precession. Since we have not discussed this feature of the magnetization dynamics so far, we do it now. As mentioned in Section 2.1, the discontinuity of the magnetization creates fictitious magnetic charges that produce the demagnetizing field resulting in the appearance of dipolar anisotropy. Therefore, in general, when one excites magnetization oscillations in an in-plane magnetized film, the precessing magnetization vector \mathbf{M} dynamically induces magnetic charges at the film surfaces. According to Equation 2.5, these charges generate a dynamic demagnetizing field \mathbf{h}_{dem} antiparallel to the out-of-plane component M_x as illustrated in Figure 5.9(a). Due to the influence of \mathbf{h}_{dem} , the precession trajectory becomes strongly elliptical with the long axis of the ellipse lying in the film plane. The elliptical precession is accompanied by the oscillation of the component of magnetization parallel to the precession axis m_z^{2f} , at twice the frequency of precession. We argue that, at large precession amplitudes, this oscillating component m_z^{2f} acts as a parametric pump that drives energy transfer from the dominant excited spin-wave mode into other modes, resulting in nonlinear damping of the former. In the presence of PMA, the out-of-plane deviation of \mathbf{M} additionally results in the appearance of the effective dynamical anisotropy field \mathbf{h}_{PMA} (Figure 5.9(b)). In contrast to \mathbf{h}_{dem} , \mathbf{h}_{PMA} is parallel to M_x (see Equation 2.7). If the magnitude of \mathbf{h}_{PMA} is close to that of \mathbf{h}_{dem} , the two fields

compensate each other, and precession becomes circular. As follows from these arguments, nonlinear damping is expected to become completely eliminated in films with moderate PMA compensating dipolar anisotropy.

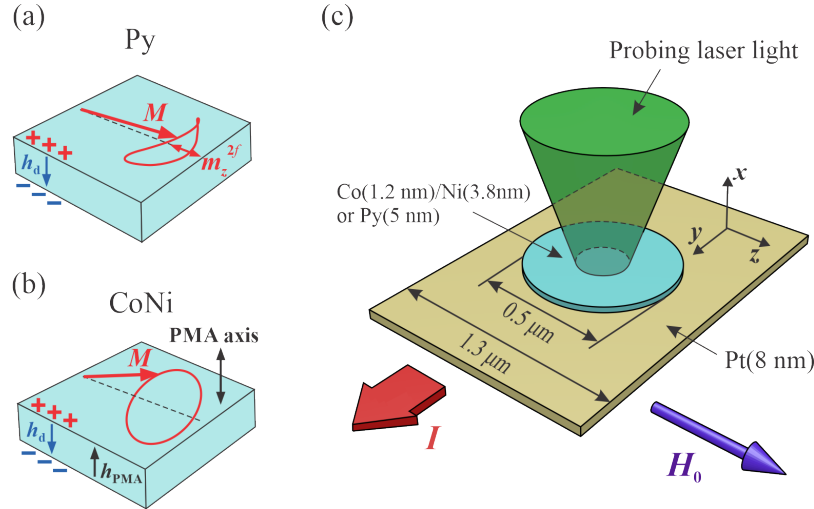


Figure 5.9 (a) The ellipticity of the magnetization precession in Py is caused by the dipolar anisotropy. (b) In CoNi, the ellipticity is minimized due to PMA compensating the dipolar anisotropy. (c) Layout of the test devices. Magnetic disks are fabricated on top of a Pt strip either from Py, or from the Co/Ni bilayer with PMA tailored to compensate the dipolar anisotropy of the film. Inset illustrates the device operation principle, based on the injection into the ferromagnetic disk of pure spin current generated due to the SHE in Pt.

To test this hypothesis, we fabricate devices based on a 8 nm-thick and 1.3 μm-wide Pt strip, and a 5 nm-thick CoNi bilayer disk with the diameter of 0.5 μm on top (Figure 5.9(c)). The parameters of the CoNi bilayer - the saturation magnetization $4\pi M_s = 6900$ G and the out-of-plane magnetic anisotropy $K_a = 1.81$ Merg/cm³ - were determined by separate magnetic characterization. According to Equation (2.7), the effective PMA field is $H_{\text{PMA}} \approx 6.6$ kOe, which is very close to the effective field associated with the dipolar anisotropy $H_d = 4\pi M_s = 6.9$ kOe. Thus, PMA in the studied system nearly compensates the dipolar anisotropy. To verify that the demonstrated effects originate from PMA, we have also studied a control sample utilizing a 5 nm-thick thick Permalloy (Py) disk with negligible PMA.

5.2.3 Results and discussion

Figures 5.10(a) and 5.10(b) show the BLS spectra of magnetic oscillations detected in Py and CoNi disks with current I close to the critical value I_C , at which SOT is expected to completely compensate magnetic damping.⁴ At $I < I_C$, both Py and CoNi exhibit similar

⁴The critical currents were determined from the analysis of the inverse BLS intensity as discussed in Section 4.1.

increases of the BLS intensity with current, as expected due to the enhancement of magnetic fluctuations by the SOT [121]. However, the behaviors diverge at $I > I_C$. In the Py disk, the intensity of fluctuations saturates, while their spectral width significantly increases (Figure 5.10(a)). In contrast, a narrow intense peak emerges in CoNi, marking a transition to the auto-oscillation regime (Figure 5.10(b)). These results indicate that the phenomena preventing the onset of auto-oscillations in the Py disk are suppressed in CoNi.

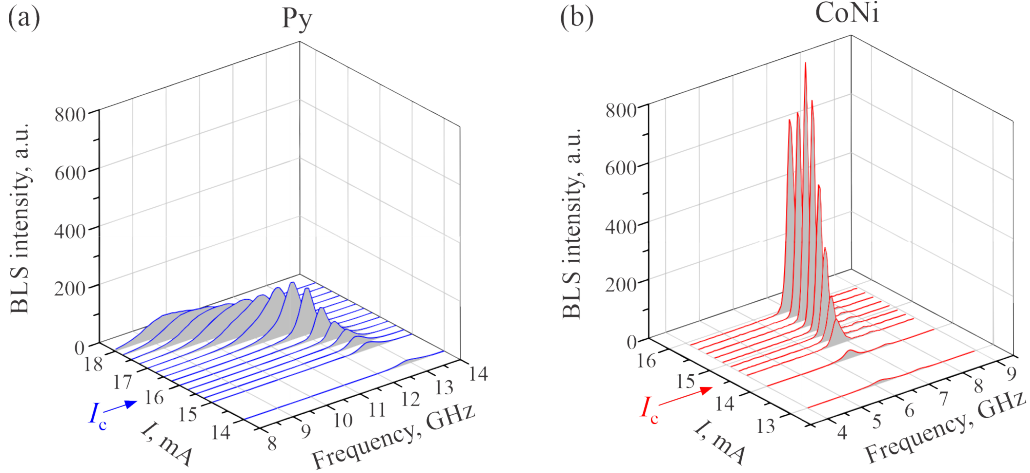


Figure 5.10 BLS spectra of magnetic oscillations vs current for Py and CoNi disks. I_C marks the critical current, at which the spin current is expected to completely compensate the natural linear magnetic damping. The data were recorded at $H_0 = 2000$ Oe.

The differences between the two systems are highlighted by the quantitative analysis of their characteristics (Figure 5.11). At $I < I_C$, the BLS intensity increases (Figure 5.11(a)), while the spectral width of fluctuations decreases due to the reduced effective damping (Figure 5.11(b)), following the same dependence for both Py and CoNi. In Py, the peak intensity starts to decrease at $I > I_C$, while the spectral width rapidly increases, indicating the onset of nonlinear damping. In contrast, in CoNi the intensity rapidly increases at $I > I_C$, while the spectral linewidth continues to decrease. We note that the BLS spectra are broadened by the finite frequency resolution of the technique, increasing the measured values particularly for small linewidths. At large currents, the BLS intensity in CoNi somewhat decreases and the spectral width increases, indicating an onset of higher-order nonlinear processes that cannot be completely avoided in real systems. The two systems also exhibit a qualitatively different dependence of the BLS peak frequency on current – the nonlinear frequency shift (Figure 5.11(c)). For CoNi, the frequency slightly increases with current, while for Py, it exhibits a redshift that becomes increasingly significant above I_C . The large frequency nonlinearity in Py is likely associated with the nonlinear excitation of a broad spectrum of spin-wave modes, which is directly related to the nonlinear suppression of the oscillations, as discussed in detail below.

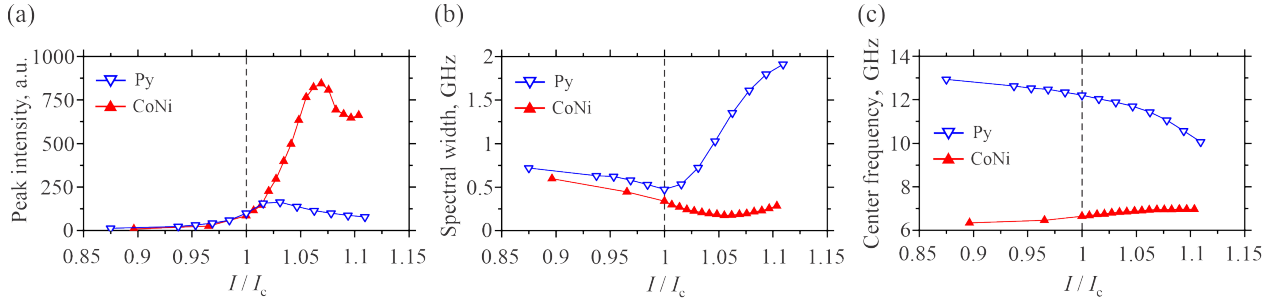


Figure 5.11 (a) Maximum intensities of the BLS spectra vs current. (b) Current dependencies of the spectral width of the BLS peaks at half the maximum intensity. (c) Center frequency of the detected spectral peaks vs current. Symbols are the experimental data, lines are guides for the eye. The data were recorded at $H_0 = 2000$ Oe.

The mechanisms underlying the observed behaviors are elucidated by the micromagnetic simulations, which were performed using the MuMax3 software. The linear spin wave dispersions, calculated using the small-amplitude limit $M_y^{\max}/M = 0.01$ (this corresponds to the precession angle of about 1°), are qualitatively similar for Py and CoNi (symbols in Figures 5.12(a) and 5.12(b)). The two branches corresponding to spin waves propagating perpendicular and parallel to the static field H_0 merge at the wavevector $k = 0$, at the FMR frequency f_{FMR} . The frequency of the branch with $k \perp H_0$ monotonically increases with k , while the branch with $k \parallel H_0$ exhibits a minimum f_{\min} at finite k due to the competition between the dipolar and the exchange interactions. The frequencies obtained from the simulations are in a good agreement with the results of calculations using Equation 2.8 (solid curves in Figures 5.12(a) and 5.12(b)).

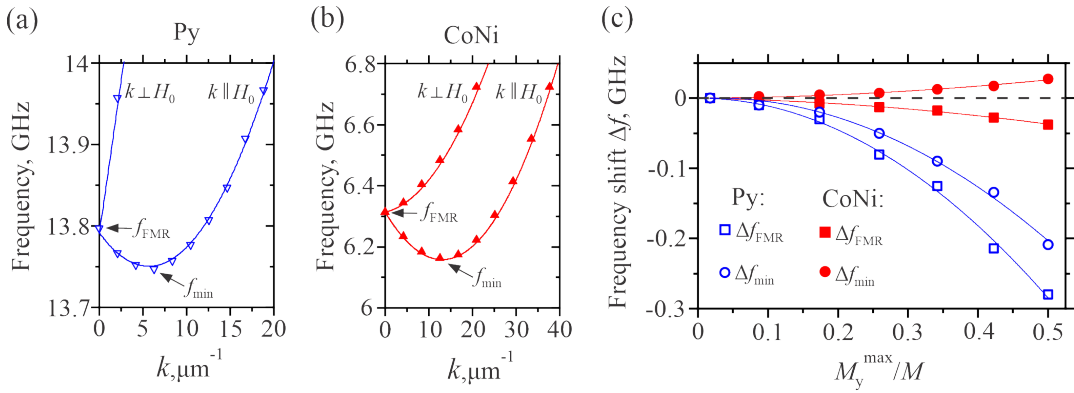


Figure 5.12 (a) and (b) Dispersion spectra for the Py and CoNi films, respectively, calculated in the small-amplitude linear regime. f_{FMR} and f_{\min} label the frequencies of the quasi-uniform FMR and of the lowest-frequency spin-wave mode, respectively. Symbols are the results of micromagnetic simulations, curves—calculations based on the analytical theory. (c) Dependences of the characteristic frequencies f_{FMR} and f_{\min} on the normalized precession amplitude. Symbols are the results of micromagnetic simulations, curves—guides for the eye. All calculations were performed at $H_0 = 2000$ Oe.

The qualitative differences between the nonlinear characteristics of the two systems are

revealed by the dependence of frequency on the amplitude of magnetization oscillations (Figure 5.12(c)). In the Py film, both f_{FMR} and f_{min} exhibit a strong negative nonlinear frequency shift. In contrast, in the CoNi film the frequency f_{FMR} slightly decreases, while the frequency f_{min} increases with increasing amplitude. The observed oscillation frequency for CoNi increases with increasing amplitude (Figure 5.11(c)). Thus, current-induced auto-oscillations correspond not to the quasi-uniform FMR mode, but rather to the lowest-frequency spin-wave mode. This conclusion is in agreement with the results of Section 4.1, which demonstrate that the SOT results in the accumulation of magnons in the state with the lowest frequency.

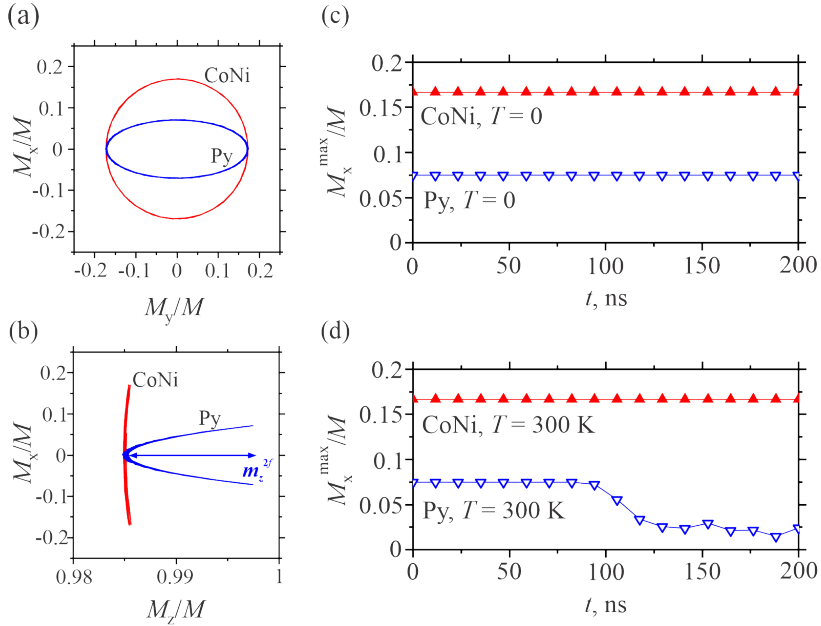


Figure 5.13 (a) and (b) Calculated magnetization trajectories for the lowest-frequency spin-wave states in Py and CoNi, as labeled. m_z^{2f} labels the double-frequency dynamic component of magnetization, which serves as a parametric pumping source for the nonlinear spin-wave excitation. (c) and (d) Temporal evolution of the free precession amplitude starting with a large initial amplitude at $t = 0$, at $T = 0$ (c) and $T = 300$ K (d). The simulations were performed with negligible linear damping, emulating the damping compensation by the spin current. All calculations were performed at $H_0 = 2000$ Oe.

We now analyze the relationship between the dispersion characteristics and the nonlinear damping effects. The lowest-frequency state at f_{min} is non-degenerate in both Py and CoNi (Figures 5.12(a) and 5.12(b)). The absence of degeneracy is commonly viewed as a sufficient condition for the suppression of nonlinear damping, since it prohibits resonant four-wave interactions [124]. However, this view is inconsistent with our experimental results (Figure 5.10) as also confirmed by the additional micromagnetic simulations illustrated in Figure 5.13. In these simulations, we use artificially small linear damping to emulate damping compensation by the spin current, and analyze the dynamics of the lowest-frequency mode excited at time $t = 0$. Figures 5.12(a) and 5.13(b) show the projections of the magnetization precession

trajectories on the $M_y - M_x$ and $M_z - M_x$ planes, respectively, for a relatively large precession amplitude $M_y^{\max}/M = 0.17$, which corresponds to the precession angle of about 10° . As expected, the precession is nearly circular in CoNi, and elliptical in Py. The ellipticity in Py results in the oscillation of the projection m_z^{2f} of magnetization on the equilibrium direction at twice the oscillation frequency, which plays the role of a parametric pump for other spin-wave modes. In simulations performed for zero temperature (Figure 5.13(c)), precession initiated at $t = 0$ continues indefinitely, i.e. energy is not transferred to other modes. This result is consistent with the parametric mechanism of mode coupling, which requires non-zero amplitudes of all the involved modes. In contrast to $T = 0$, at finite temperatures all the spin-wave modes have non-zero amplitudes due to thermal fluctuations, enabling their parametric excitation. In the simulations performed at $T = 300\text{K}$, the amplitude of precession excited in Py at $t = 0$ abruptly drops at about 100 ns and continues to decrease thereafter, indicating the onset of nonlinear damping (Figure 5.13(d)). In contrast, in CoNi, where the oscillations of the longitudinal magnetization component are negligibly small $m_z^{2f} \approx 0$, the precession amplitude remains constant. These results clearly show that the compensation of the precession ellipticity by the PMA enables suppression of the nonlinear damping, supporting our interpretation of the experimental findings.

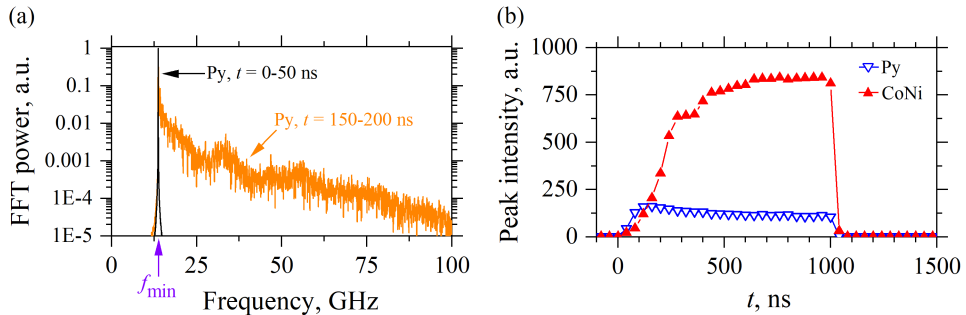


Figure 5.14 (a) Fourier spectra of magnetization oscillations in Py before ($t = 0 - 50\text{ ns}$) and after ($t = 150 - 200\text{ ns}$) the onset of nonlinear damping. (b) Evolution of the nonlinear damping in the time domain. Time dependence of the peak BLS intensity in response to the $1\text{ }\mu\text{s}$ long pulse of current obtained for the Py and CoNi disks, as labeled. The data were recorded at $H_0 = 2000\text{ Oe}$ and $I = 1.07I_C$.

Spectral analysis of the temporal evolution of the precession amplitude in Py at $T = 300\text{ K}$ confirms that the initially monochromatic oscillation at frequency f_{\min} transitions to a broad spectrum of spin-wave modes excited at longer times due to their nonlinear coupling to the initially excited mode (Figure 5.14(a)). Since the frequencies and, hence, the wavevectors of these secondary spin waves are large, we cannot detect them directly in the BLS measurements. However, the effects of the nonlinear damping can be clearly seen in the time-domain BLS measurements. In these measurements, the current was applied in pulses with the duration of $1\text{ }\mu\text{s}$ and period of $5\text{ }\mu\text{s}$, and the temporal evolution of the BLS

intensity was analyzed. Figure 5.14(b) shows the temporal traces of the intensity recorded for the Py and CoNi disks at $I = 1.07I_C$, corresponding to the maximum intensity achieved in CoNi sample [Figure 5.11(a)]. For the CoNi disk, the intensity monotonically increases and then saturates. In contrast, for the Py disk, the intensity saturates at a much lower level shortly after the start of the pulse, followed by a gradual decrease over the rest of the pulse duration, indicating the onset of energy flow into other spin-wave modes as predicted by our simulations (Figure 5.13(d)). We note that the observed decrease is not that abrupt, as it appears in simulations, because the flow into the other modes is counterbalanced by the continuous flow due to the injection of the spin current.

5.2.4 Conclusions

In conclusion, our experiments and simulations show that the adverse nonlinear damping can be efficiently suppressed by minimizing the ellipticity of magnetization precession, using magnetic materials where dipolar anisotropy is compensated by the PMA. This allows one to achieve complete compensation of the magnetic damping, and excitation of coherent magnetization auto-oscillations by the spin current without confining the spin current injection area to nanoscale. Our findings open a route for the implementation of SOT-oscillators capable of generating microwave signals with technologically relevant power levels and coherence, circumventing the challenges of phase locking a large number of oscillators with nanoscale dimensions [135]. They also provide a route for the implementation of spatially extended amplification of coherent propagating spin waves, which is vital for the emerging field of magnonics. The proposed approach can also facilitate the realization of stable SOT-driven Bose–Einstein condensation of magnons, which was not achieved in the experiment discussed in Section 4.1 due to the detrimental effects of nonlinear damping.

Chapter 6

Excitation and amplification of spin waves by the SOT

6.1 Motivation

In Chapters 4 and 5, we have studied various aspects of SOT-induced magnetic oscillations. Let us emphasize that, in all the considered systems, magnetization auto-oscillations are spatially confined mainly due to the negative nonlinear frequency shift, which drives the auto-oscillation frequency below the spin-wave spectrum (see Figures 4.10(b) and 5.4(b)). Consequently, none of them provide the possibility to generate coherent propagating spin waves by the SOT. However, as mentioned in Chapter 1, the excitation of propagating spin waves by the SOT is particularly important for magnonics, because this new method can become a high-efficiency nanoscale alternative to the traditional inductive excitation mechanism. It turned out to be challenging to find a suitable geometry that could convert spatially localized magnetic auto-oscillation into coherent propagating spin waves. In this chapter we experimentally demonstrate the first magnonic nanodevice capable of such a conversion. Moreover, in the demonstrated system, the same SOT mechanism not only generates propagating spin waves, but also simultaneously compensates their propagation losses over a spatially extended region. The results presented below were published in *Advanced Materials* 30, 1802837 (2018).

6.2 Studied system

Our test devices are based on a concept of nano-notch SOT-oscillator directly incorporated into a magnonic waveguide (Figure 6.1). The devices consist of 180 nm-wide and 4 μm -long nano-waveguides patterned from a Py(15 nm)/Pt(4 nm) bilayer. Ion milling was used to pattern a rectangular 200 nm-wide and 10 nm-deep notch in the top Py layer of the waveguide,

forming a nano-oscillator that serves as the spin-wave source. When electric current I flows through the device, the SHE in Pt injects pure spin current I_S into the Py layer, producing the SOT on its magnetization M that compensates the magnetic damping. Note that the magnitude of the SOT is inversely proportional to the thickness of the magnetic layer (see Equation 2.14). Thus, the effects of the SOT on the 5 nm-thick Py layer in the nano-notch area are significantly larger than on the 15 nm-thick Py waveguide. As the current I is increased, damping becomes completely compensated in the nano-notch region, resulting in the local excitation of magnetization auto-oscillations. Meanwhile, damping remains only partially compensated in the waveguide. The nano-notch oscillator can emit spin waves into the waveguide, provided that the latter supports propagating spin-waves at the frequency of auto-oscillation. Since the entire waveguide is subjected to the spin current I_S reducing the natural damping, the propagation of the emitted spin waves can become enhanced by the current-induced SOT.

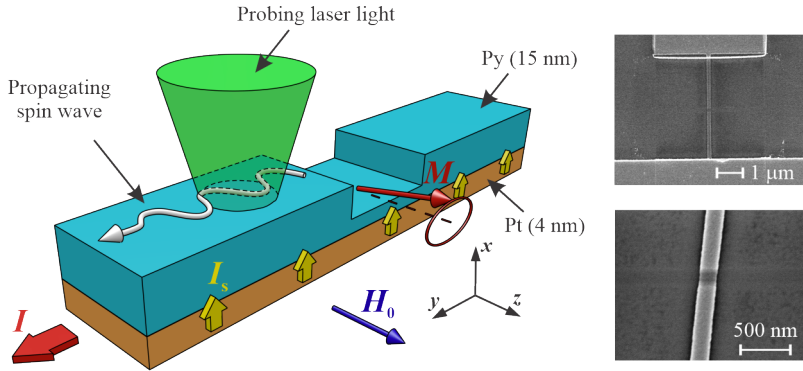


Figure 6.1 Schematic of the test device. The test devices are 180 nm-wide Py(15 nm)/Pt(4 nm) nanowaveguides with a 200 nm-wide wide and 10 nm-deep rectangular nanonotch in the center. The injected spin current I_S , excites magnetization auto-oscillations in the nano-notch, resulting in the spin wave emission into the waveguide. Insets show the scanning electron microscope images of the device and of the active nano-notch region.

6.3 Results and discussion

First, we characterize the auto-oscillation by analyzing the BLS spectra obtained with the laser spot positioned on the nano-notch region. A representative spectrum obtained at $I = 3.8$ mA exhibits two intense auto-oscillation peaks (Figure 6.2(a)). Micromagnetic simulations described below allow us to identify these peaks as the two fundamental dynamic modes of the nano-notch characterized by different frequencies and different distributions of the dynamic magnetization across the nanowire width (insets in Figure 6.2(a)). For the low-frequency (LF) mode, the dynamical magnetization amplitude is largest at the edges of the nanowire. For the high-frequency (HF) mode, the amplitude is largest at the center.

Therefore, we interpret the LF mode as the edge mode and the HF mode as the central mode (see Section 2.3.2).

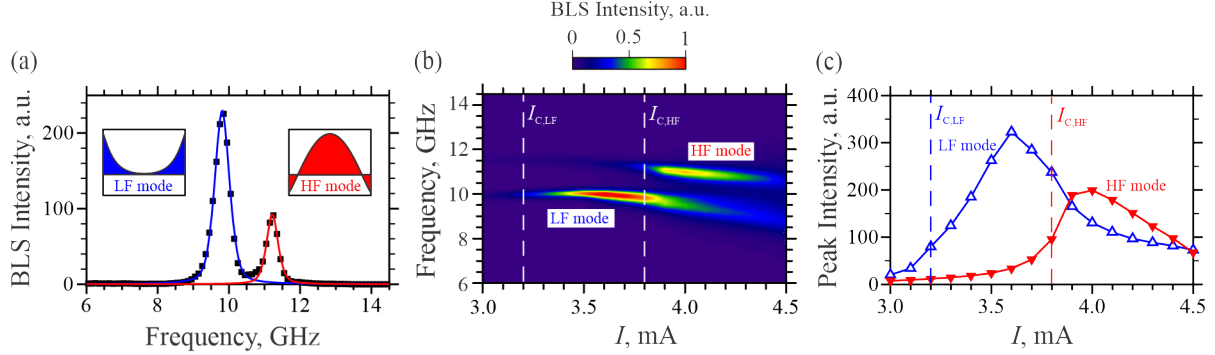


Figure 6.2 (a) Representative BLS spectrum of auto-oscillations measured at $I = 3.8$ mA with the probing spot positioned on the nano-notch. Symbols: experimental data, lines: Lorentzian fits of the spectral peaks. Insets schematically show the transverse profiles of the dynamic magnetization corresponding to the low-frequency (LF) and the high-frequency (HF) mode. (b) Normalized color-coded map of the BLS intensity in the frequency-current coordinates. (c) Current dependences of the peak intensity for the LF and the HF mode. Symbols: experimental data; lines: guides for the eye. The measurements were performed at $H_0 = 2000$ Oe.

The device exhibits stable auto-oscillations over a significant range of driving currents (Figure 6.2(b)). By using the spectroscopy of thermal magnetic fluctuations (see discussion in Section 4.1), we determine the critical currents $I_{C,LF} \approx 3.2$ mA for the LF mode and $I_{C,HF} \approx 3.8$ mA for the HF mode. The LF mode starts to auto-oscillate at smaller currents than the HF mode due to its smaller frequency, in agreement with the theory of STO-driven auto-oscillations (Equation 2.14). Both modes are characterized by a “soft” auto-oscillation onset - a gradual initial increase of intensity with increasing driving current (Figure 6.2(c)) [118]. The intensity of the LF mode saturates and starts to decrease around $I = 3.6$ mA, while the intensity of the HF mode exhibits a rapid increase, indicating that the two modes compete for the angular momentum delivered into the magnetic system by the spin current.

To analyze the oscillation-induced magnetization dynamics in the waveguide, we raster the probing BLS spot over the waveguide area. Figures 6.3(a) and 6.3(b) show representative maps of the dynamic magnetization at the LF and the HF mode frequency, respectively. Note that the measured maps represent a convolution of the actual distribution of the dynamic magnetization with the distribution of the light intensity in the probing spot with the diameter of about 0.3 μ m, which does not allow one to resolve the details of the transverse distribution of the dynamic magnetization in the nano-waveguide (insets in Figure 6.2(a)). Despite the limited resolution, the data of Figures 6.3(a) and 6.3(b) clearly show that the LF mode is localized in the nano-notch, and does not emit spin waves into the waveguide. In contrast, the HF mode emits spin waves, preferentially in the positive- y direction.

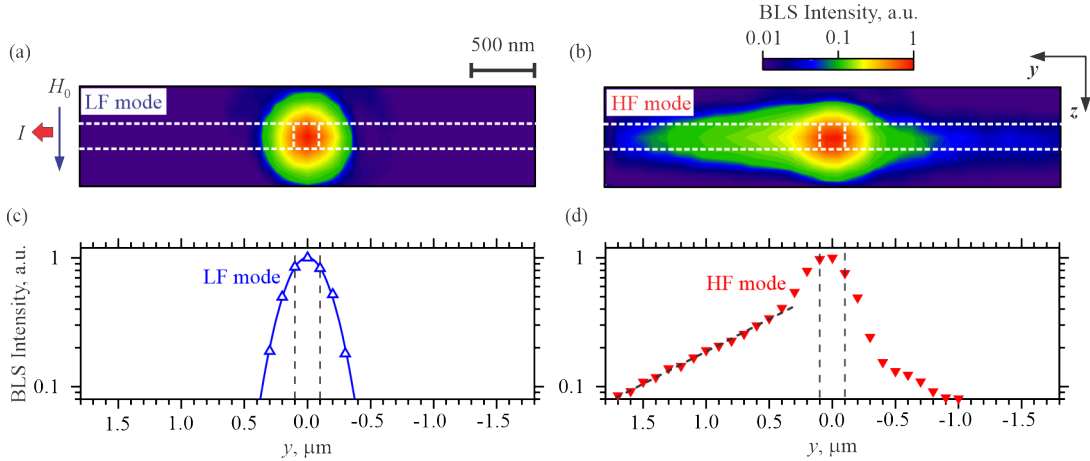


Figure 6.3 (a) and (b) Color-coded spatial maps of the BLS intensity measured at the frequency of the LF and the HF mode, as labeled. The maps were recorded at $I = 4$ mA and $H_0 = 2000$ Oe. Dashed lines on the maps show the outlines of the waveguide and of the nano-notch. (c) and (d) Symbols: dependence of the BLS intensity for LF and HF modes, as labeled, on the propagation coordinate. Note the logarithmic intensity scale. Solid curve in (c): Gaussian fit of the data for the LF mode. Dashed line in (d): exponential fit of the data for the HF mode at $y < -0.5$ μ m.

To characterize the emission and propagation quantitatively, in Figures 6.3(c) and 6.3(d) we plot on the log-linear scale the propagation-coordinate dependence of the BLS intensity. These data clearly demonstrate that the spin waves emitted by the HF mode exponentially decay away from the nano-notch. By fitting the data with the exponential function, we find the decay length $l = 1.5$ μ m, at which the amplitude of the wave decreases by a factor of e . By comparing the intensities of the waves emitted to the left and to the right, we also determine that the decay length is the same for the two directions, but the intensities differ by about a factor of 3.

To understand the mechanisms of spin-wave emission, one has to consider the effects of the demagnetizing field on the effective field in the nanowire. According to Equation 2.10, the magnitude of the demagnetizing field is proportional to the thickness of a magnetic layer d : thicker is the layer, larger are the demagnetizing effects. Thus, the total effective field in the waveguide is smaller compared to that in the nanonotch (Figure 6.4(a)). The reduction of the effective field results in a downshift of the spin-wave dispersion curve in the waveguide (Figure 6.4(b)). Therefore, the waveguide supports the propagation of spin waves at the frequency of the HF mode and does not support it at the frequency of the LF mode, as shown in Figure 6.4(b).

To confirm this interpretation, we have performed micromagnetic simulations by using the Mumax3 software. The oscillation of magnetization in the nano-notch area is simulated with a local monochromatic microwave field, applied perpendicular to the surface. Figure 6.4(c) shows snapshots of the dynamic magnetization in the waveguide produced by the excitation at the frequencies of the LF and the HF modes, as labeled. Oscillations excited

at the frequency of the LF mode remain localized in the notch area and do not generate propagating spin waves, in agreement with the experimental data. In contrast, excitation at the frequency of the HF mode results in the generation of spin waves propagating in both directions away from the notch.

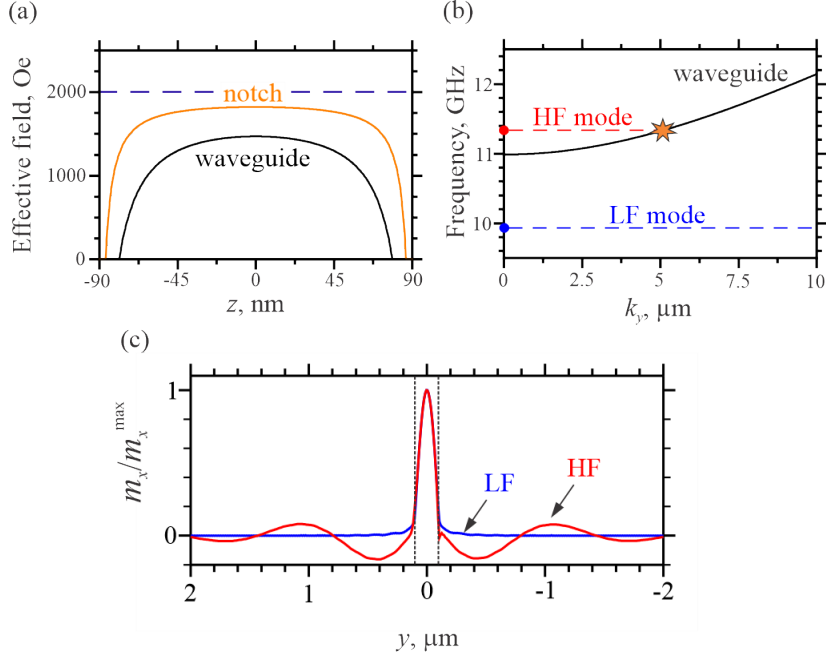


Figure 6.4 (a) Calculated distribution of the effective magnetic field in the nano-notch and the waveguide through the section transverse to the nanowire. The horizontal dashed line indicates the applied external magnetic field. (b) Curve is the dispersion for spin waves in the waveguide obtained from the micromagnetic simulations. Horizontal dashed lines show the auto-oscillation frequencies of the LF (9.97 GHz) and HF (11.36 GHz) mode, as labeled. (c) Snapshots of the dynamic magnetization in the waveguide for the excitation at the frequency of the LF (9.97 GHz) and of the HF (11.36 GHz) mode, as labeled, obtained from the micromagnetic simulations. Dashed vertical lines show the edges of the nanonotch.

Figure 6.5(a) shows the current-dependent values of the spin-wave decay length obtained in the experiment and from the simulations. For each value of I , the excitation frequency used in the simulations is determined from the experimental data (Figure 6.2(b)), and the damping constant is set to the standard value for Py, $\alpha = 0.01$. The simulations reproduce the experimentally observed reduction of the decay length with increasing current, which can be attributed to the smaller group velocity of lower-frequency spin waves excited at larger currents (see the spin-wave dispersion in Figure 6.4(b)). However, the magnitude of the decay length observed in the experiment is significantly larger than that obtained in the simulations using the natural damping constant. The ratio of the two lengths increases from 2 at $I = 3.6$ mA to 3 at $I = 4.5$ mA (symbols in Figure 6.5(b)).

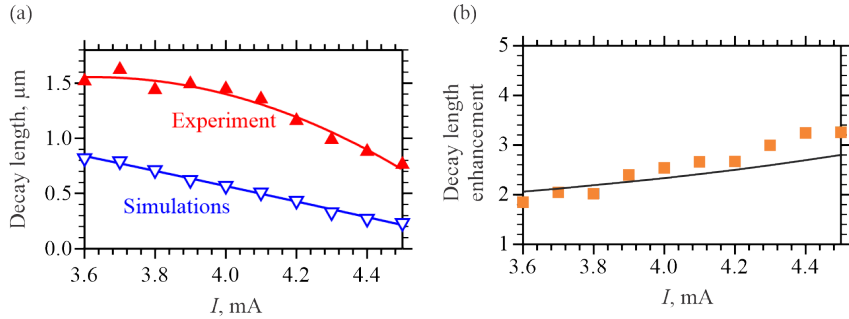


Figure 6.5 (a) Current dependence of the decay length of emitted spin waves. Point-up triangles: experimental data. Point-down triangles: results of simulations with the standard damping, i.e. neglecting the effects of current on the spin wave propagation. Curves: guides for the eye. (c) Symbols: ratio of the experimental to the simulated value of the decay length. Solid curve: enhancement of the decay length expected from the SOT-induced damping compensation.

We attribute the observed difference to the compensation of the magnetic damping in the waveguide by the spin current injected over the entire spin-wave propagation path (Figure 6.1). According to Equation 2.14, the current-dependent effective damping varies as $\alpha(I) = \alpha_0(1 - I/I_C)$, where α_0 is the effective damping constant at $I = 0$, and I_C is the critical current, at which the damping becomes completely compensated in the waveguide. By using the spectroscopy of thermal magnetic fluctuations, we determine $I_C \approx 7\text{ mA}$ for the 15 nm-thick Py waveguide, and calculate the enhancement of the decay length associated with the SOT-induced damping compensation (solid curve in Figure 6.5(c)). The obtained dependence is in a good agreement with the experimental data, demonstrating that the same SOT mechanism enables the generation of spin waves, and simultaneously a significant enhancement of their propagation.

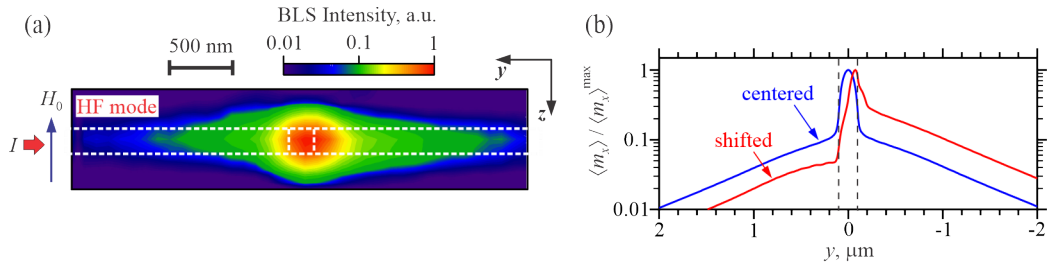


Figure 6.6 (a) Same as Figure 6.3(b), measured with reversed directions of the static magnetic field and of the driving current. (b) Emission asymmetry due to the spatial shift of the oscillation region. Calculated spatial dependences of the time-averaged amplitudes of the dynamic magnetization, for the oscillation region centered on the nano-notch, and for the oscillation region shifted to the edge of the notch, as labeled. Dashed vertical lines indicate the edges of the nano-notch.

Additional measurements show that the direction of the preferential emission can be reversed by reversing the direction of the static magnetic field (Figure 6.6(a)). Note that according to the symmetry of the SHE, reversing the field for a given current polarity changes the sign of the SOT (see Equation 2.13). Therefore, to achieve damping compensation and

auto-oscillations, the direction of the dc current must be also reversed. The data of Figure 6.6(a) demonstrate that the proposed devices provide the ability to control unidirectional emission of spin waves by the direction of the magnetic field. We emphasize that, however, our simulations predict symmetric bidirectional emission of spin waves (Figure 6.4(c)). Additionally, the simulated amplitude of the emitted waves amounts to about 10% of the maximum value in the center of the notch, significantly smaller than 60–70% observed in the experiment (Figure 6.3(d)). We explain these discrepancies by the asymmetric spatial profile of the SOT-driven auto-oscillation mode, whose maximum amplitude is shifted toward one of the edges of the nanonotch, similar to the spatial asymmetry of recently observed spin-wave solitons [175]. Indeed, the experimental profile of auto-oscillation is clearly shifted in the positive- y (Figure 6.3(b)) or negative- y (Figure 6.6(a)) direction, depending on the direction of the field. In the simulations, we model this effect by shifting the excitation area by half-width of the nanonotch, resulting in a strongly unidirectional emission, with the asymmetry and coupling efficiency close to those observed in the experiment (Figure 6.6(b)).

6.4 Conclusions

In conclusion, we have experimentally demonstrated a nanomagnonic system that combines all the advantages provided by the SOT to locally excite propagating spin waves, and to simultaneously enhance their propagation characteristics. This was accomplished by hybridizing two magnetic subsystems with different dynamic characteristics: the active subsystem (the nano-notch oscillator) in which a spatially confined dynamical mode (the HF mode) is excited by the SOT, and the spin-wave guiding subsystem that facilitates propagation and long-range enhancement of the generated spin waves. The system is amendable to modifications of structure and geometry, and can be easily incorporated as a building block in complex magnonic circuits with expanded functionalities.

Chapter 7

Summary and outlook

”As our circle of knowledge expands, so does the circumference of darkness surrounding it”. The authorship of this phrase is attributed to many people, but regardless of its author, it beautifully reflects the fact that any research not only provides answers to existing questions, but also raises new ones. Therefore, in this final chapter, we summarize the main results of the thesis and outline possible directions for future research.

The most important results of Chapter 4 are:

- We have experimentally demonstrated that the lowest-frequency magnon mode experience the strongest enhancement by the SOT. This demonstration resolved the long-standing debate in the studies of spin current-induced effects.
- We have provided the first direct evidence that the state of the magnon gas subjected to the SOT can be treated thermodynamically, supporting the theoretically suggested relationship between current-induced magnetization auto-oscillations and Bose–Einstein condensation of magnons.
- We have demonstrated that the chemical potential of the magnon gas driven by the SOT can closely approach the lowest-energy magnon state, indicating the possibility of spin current-driven Bose–Einstein condensation of magnons.

The following questions have arisen/future research directions:

- According to our data, for one polarization of the spin current, the effective temperature of the magnon gas becomes significantly reduced, whereas the chemical potential stays almost constant. In contrast, for the opposite polarization, the effective temperature remains nearly unaffected, whereas the chemical potential increases with current. However, it is natural to expect that both the effective temperature and the chemical

potential should increase/decrease for positive/negative currents. Therefore, the observed asymmetry between two directions of current is a puzzling aspect of our results, which is still waiting for explanation.

- Strictly speaking, our experimental data provide evidence for the quasi-equilibrium state only for the low-energy magnons, and it is currently not possible to make a unambiguous conclusion that the high-energy magnons are described by the same thermodynamic characteristics. It was recently demonstrated that one can increase the spectral range of the μ BLS technique by utilizing the sub-diffraction confinement of light by a metallic nanoantenna fabricated on top of a magnetic film [151]. Therefore, it would be interesting to use this approach to determine thermodynamic characteristics of high-energy magnons that are not accessible to the standard μ BLS.
- One can also optimize the thickness of the active magnetic layer in the system shown in Figure 4.1, so as to gain experimental access to perpendicular standing spin waves (PSSW) [1]. The PSSW modes are characterized by relatively high frequencies. Therefore, one can potentially use them to study thermodynamic properties of high-energy magnon states [93].

The most important results of Chapter 5 are:

- We have shown experimentally and by micromagnetic simulations that nonlinear damping is predominantly determined by the ellipticity of magnetization precession, which is controlled by the dipolar anisotropy.
- We have demonstrated that by using materials with suitably tailored PMA, one can compensate the dipolar anisotropy and achieve circular precession, resulting in an almost complete suppression of nonlinear damping.
- As a result, we were able to achieve complete damping compensation and excitation of coherent magnetization auto-oscillations by the SOT in a simple system with uniform spatially extended injection of spin current.

The following questions have arisen/future research directions:

- While the reported results are encouraging, little is currently known about the spectral coherence of the demonstrated devices, which is important for their technical applications. Therefore, one can integrate the device shown in Figure 5.9(c) with an inductive antenna to measure the generated power and the actual spectral linewidth of SOT-induced auto-oscillations in such systems [62, 176].

- We also emphasize that our micromagnetic simulations clearly show that, in a strongly nonequilibrium magnetic system, nonlinear interactions are mediated by complex non-resonant processes, which are poorly understood at the moment. Therefore, additional simulations and thoughtful theoretical analysis are highly desirable to gain further insight into the mechanisms of energy flow associated with the nonlinear damping.
- Last but not least, one can try to utilize the approach demonstrated in Chapter 5 to achieve decay-free propagation of spin waves, and perhaps even their true amplification. We note that it would resolve one of the main issues hindering the development nano-magnonics.

The most important results of Chapter 6 are:

- We have experimentally demonstrated the first SOT oscillator that provides the possibility to generate coherent propagating spin waves.
- Furthermore, the demonstrated system also enables simultaneous enhancement of propagation characteristics of the generated spin waves, thus combining all the advantage provided by the SOT.

The following questions have arisen/future research directions:

- As discussed in Chapter 6, the demonstrated device exhibits a controllable directional asymmetry of spin wave emission. We have associated this phenomenon with the asymmetric spatial profile of the SOT-driven auto-oscillation mode. While this interpretation is quite plausible, additional micromagnetic simulations are required to rule out other possible explanations.
- Since the proposed system has a simple and flexible layout, its characteristics can be easily improved by the material engineering and geometry optimization. For example, the system can be implemented with low-damping insulating magnetic materials [177], or one can optimize the topography of the nano-notch oscillator [178].
- It might also be interesting to try to synchronize the nano-notch oscillator to an external microwave signal [179], or to create a chain of nano-notch oscillators that are mutually synchronized via propagating spin waves [180–182].

To conclude, the results presented in this thesis provide valuable insights into many fundamental physical phenomena associated with the interaction between spin currents and the dynamic magnetization. Hopefully, they will serve as the basis for further discoveries that can eventually lead to a breakthrough in the technical applications of nanoscale spin-wave devices.

References

- [1] A. G. Gurevich and G. A. Melkov, *Magnetization oscillations and waves*. CRC press, 1996.
- [2] A. Prabhakar and D. D. Stancil, *Spin waves: Theory and applications*, vol. 5. Springer, 2009.
- [3] C. Kittel, P. McEuen, and P. McEuen, *Introduction to solid state physics*, vol. 8. Wiley New York, 1996.
- [4] F. Bloch, “Zur theorie des ferromagnetismus,” *Zeitschrift für Physik*, vol. 61, no. 3-4, pp. 206–219, 1930.
- [5] J. H. Griffiths, “Anomalous high-frequency resistance of ferromagnetic metals,” *Nature*, vol. 158, no. 4019, pp. 670–671, 1946.
- [6] J. D. Adam, “Analog signal processing with microwave magnetics,” *Proceedings of the IEEE*, vol. 76, no. 2, pp. 159–170, 1988.
- [7] W. S. Ishak, “Magnetostatic wave technology: A review,” *Proceedings of the IEEE*, vol. 76, no. 2, pp. 171–187, 1988.
- [8] P. Kabos and V. Stalmachov, *Magnetostatic Waves and Their Application*. Springer Science & Business Media, 2012.
- [9] H. How, “Magnetic microwave devices,” *Encyclopedia of RF and Microwave Engineering*, 2005.
- [10] J. M. Owens, J. H. Collins, and R. L. Carter, “System applications of magnetostatic wave devices,” *Circuits, Systems and signal processing*, vol. 4, no. 1-2, pp. 317–334, 1985.
- [11] A. V. Chumak, “Fundamentals of magnon-based computing,” *arXiv preprint arXiv:1901.08934*, 2019.

- [12] A. Mahmoud, F. Ciubotaru, F. Vanderveken, A. V. Chumak, S. Hamdioui, C. Adelmann, and S. Cotofana, “Introduction to spin wave computing,” *Journal of Applied Physics*, vol. 128, no. 16, p. 161101, 2020.
- [13] G. Csaba, Á. Papp, and W. Porod, “Perspectives of using spin waves for computing and signal processing,” *Physics Letters A*, vol. 381, no. 17, pp. 1471–1476, 2017.
- [14] V. Cherepanov, I. Kolokolov, and V. L’vov, “The saga of yig: spectra, thermodynamics, interaction and relaxation of magnons in a complex magnet,” *Physics reports*, vol. 229, no. 3, pp. 81–144, 1993.
- [15] J. Barker and G. E. Bauer, “Thermal spin dynamics of yttrium iron garnet,” *Physical review letters*, vol. 117, no. 21, p. 217201, 2016.
- [16] A. J. Princep, R. A. Ewings, S. Ward, S. Tóth, C. Dubs, D. Prabhakaran, and A. T. Boothroyd, “The full magnon spectrum of yttrium iron garnet,” *npj Quantum Materials*, vol. 2, no. 1, pp. 1–5, 2017.
- [17] C. Liu, J. Chen, T. Liu, F. Heimbach, H. Yu, Y. Xiao, J. Hu, M. Liu, H. Chang, T. Stueckler, *et al.*, “Long-distance propagation of short-wavelength spin waves,” *Nature communications*, vol. 9, no. 1, pp. 1–8, 2018.
- [18] V. Sluka, T. Schneider, R. A. Gallardo, A. Kákay, M. Weigand, T. Warnatz, R. Mattheis, A. Roldán-Molina, P. Landeros, V. Tiberkevich, *et al.*, “Emission and propagation of 1d and 2d spin waves with nanoscale wavelengths in anisotropic spin textures,” *Nature Nanotechnology*, vol. 14, no. 4, pp. 328–333, 2019.
- [19] P. Che, K. Baumgaertl, A. Kúkol’ová, C. Dubs, and D. Grundler, “Efficient wavelength conversion of exchange magnons below 100 nm by magnetic coplanar waveguides,” *Nature communications*, vol. 11, no. 1, pp. 1–9, 2020.
- [20] H. Yu, O. d. Kelly, V. Cros, R. Bernard, P. Bortolotti, A. Anane, F. Brandl, F. Heimbach, and D. Grundler, “Approaching soft x-ray wavelengths in nanomagnet-based microwave technology,” *Nature communications*, vol. 7, no. 1, pp. 1–7, 2016.
- [21] A. Chumak, A. Serga, and B. Hillebrands, “Magnonic crystals for data processing,” *Journal of Physics D: Applied Physics*, vol. 50, no. 24, p. 244001, 2017.
- [22] B. A. Kalinikos and A. B. Ustinov, “Nonlinear spin waves in magnetic films and structures: Physics and devices,” in *Solid State Physics*, vol. 64, pp. 193–235, Elsevier, 2013.

- [23] M. Cottam and A. Slavin, “Fundamentals of linear and nonlinear spin wave processes in bulk and finite magnetic samples,” 1994.
- [24] V. S. L’vov, *Wave turbulence under parametric excitation: applications to magnets*. Springer Science & Business Media, 2012.
- [25] P. E. Wigen, *Nonlinear phenomena and chaos in magnetic materials*. World scientific, 1994.
- [26] V. Kruglyak, S. Demokritov, and D. Grundler, “Magnonics,” *Journal of Physics D: Applied Physics*, vol. 43, no. 26, p. 264001, 2010.
- [27] B. Lenk, H. Ulrichs, F. Garbs, and M. Münzenberg, “The building blocks of magnonics,” *Physics Reports*, vol. 507, no. 4-5, pp. 107–136, 2011.
- [28] S. Neusser and D. Grundler, “Magnonics: Spin waves on the nanoscale,” *Advanced Materials*, vol. 21, no. 28, pp. 2927–2932, 2009.
- [29] S. O. Demokritov and A. N. Slavin, *Magnonics: From fundamentals to applications*, vol. 125. Springer Science & Business Media, 2012.
- [30] S. A. Nikitov, D. V. Kalyabin, I. V. Lisenkov, A. Slavin, Y. N. Barabanenkov, S. A. Osokin, A. V. Sadovnikov, E. N. Beginin, M. A. Morozova, Y. A. Filimonov, *et al.*, “Magnonics: a new research area in spintronics and spin wave electronics,” *Physics-Uspekhi*, vol. 58, no. 10, p. 1002, 2015.
- [31] A. V. Chumak, V. I. Vasyuchka, A. A. Serga, and B. Hillebrands, “Magnon spintronics,” *Nature Physics*, vol. 11, no. 6, pp. 453–461, 2015.
- [32] A. Khitun, M. Bao, and K. L. Wang, “Magnonic logic circuits,” *Journal of Physics D: Applied Physics*, vol. 43, no. 26, p. 264005, 2010.
- [33] K.-S. Lee and S.-K. Kim, “Conceptual design of spin wave logic gates based on a mach–zehnder-type spin wave interferometer for universal logic functions,” *Journal of Applied Physics*, vol. 104, no. 5, p. 053909, 2008.
- [34] T. Schneider, A. A. Serga, B. Leven, B. Hillebrands, R. L. Stamps, and M. P. Kostylev, “Realization of spin-wave logic gates,” *Applied Physics Letters*, vol. 92, no. 2, p. 022505, 2008.
- [35] Y. Khivintsev, A. Kozhevnikov, G. Dudko, V. Sakharov, Y. Filimonov, and A. Khitun, “Spin waves in yig-based networks: Logic and signal processing,” *Physics of Metals and Metallography*, vol. 120, no. 13, pp. 1318–1324, 2019.

- [36] T. Fischer, M. Kewenig, D. Bozhko, A. Serga, I. Syvorotka, F. Ciubotaru, C. Adelmann, B. Hillebrands, and A. Chumak, “Experimental prototype of a spin-wave majority gate,” *Applied Physics Letters*, vol. 110, no. 15, p. 152401, 2017.
- [37] G. Talmelli, T. Devolder, N. Träger, J. Förster, S. Wintz, M. Weigand, H. Stoll, M. Heyns, G. Schütz, I. Radu, *et al.*, “Reconfigurable nanoscale spin wave majority gate with frequency-division multiplexing,” *arXiv preprint arXiv:1908.02546*, 2019.
- [38] A. V. Chumak, A. A. Serga, and B. Hillebrands, “Magnon transistor for all-magnon data processing,” *Nature communications*, vol. 5, no. 1, pp. 1–8, 2014.
- [39] A. Sadovnikov, E. Beginin, S. Sheshukova, D. Romanenko, Y. P. Sharaevskii, and S. Nikitov, “Directional multimode coupler for planar magnonics: Side-coupled magnetic stripes,” *Applied Physics Letters*, vol. 107, no. 20, p. 202405, 2015.
- [40] Q. Wang, P. Pirro, R. Verba, A. Slavin, B. Hillebrands, and A. V. Chumak, “Reconfigurable nanoscale spin-wave directional coupler,” *Science advances*, vol. 4, no. 1, p. e1701517, 2018.
- [41] Q. Wang, M. Kewenig, M. Schneider, R. Verba, F. Kohl, B. Heinz, M. Geilen, M. Mohseni, B. Lägel, F. Ciubotaru, *et al.*, “A magnonic directional coupler for integrated magnonic half-adders,” *Nature Electronics*, pp. 1–10, 2020.
- [42] G. Csaba, A. Papp, W. Porod, and R. Yeniceri, “Non-boolean computing based on linear waves and oscillators,” in *2015 45th European Solid State Device Research Conference (ESSDERC)*, pp. 101–104, IEEE, 2015.
- [43] G. Csaba, A. Papp, and W. Porod, “Spin-wave based realization of optical computing primitives,” *Journal of Applied Physics*, vol. 115, no. 17, p. 17C741, 2014.
- [44] Á. Papp, W. Porod, Á. I. Csurgay, and G. Csaba, “Nanoscale spectrum analyzer based on spin-wave interference,” *Scientific Reports*, vol. 7, no. 1, pp. 1–9, 2017.
- [45] T. Brächer and P. Pirro, “An analog magnon adder for all-magnonic neurons,” *Journal of Applied Physics*, vol. 124, no. 15, p. 152119, 2018.
- [46] V. Vlaminck and M. Bailleul, “Spin-wave transduction at the submicrometer scale: Experiment and modeling,” *Physical Review B*, vol. 81, no. 1, p. 014425, 2010.
- [47] V. E. Demidov and S. O. Demokritov, “Magnonic waveguides studied by microfocus brillouin light scattering,” *IEEE Transactions on Magnetics*, vol. 51, no. 4, pp. 1–15, 2015.

- [48] A. Papp, G. Csaba, H. Dey, M. Madami, W. Porod, and G. Carlotti, “Waveguides as sources of short-wavelength spin waves for low-energy ict applications,” *The European Physical Journal B*, vol. 91, no. 6, p. 107, 2018.
- [49] S. Azzawi, A. Hindmarch, and D. Atkinson, “Magnetic damping phenomena in ferromagnetic thin-films and multilayers,” *Journal of Physics D: Applied Physics*, vol. 50, no. 47, p. 473001, 2017.
- [50] V. Krivoruchko, “Spin waves damping in nanometre-scale magnetic materials,” *Low Temperature Physics*, vol. 41, no. 9, pp. 670–681, 2015.
- [51] P. Gambardella and I. M. Miron, “Current-induced spin–orbit torques,” *Philosophical Transactions of the Royal Society A: Mathematical, Physical and Engineering Sciences*, vol. 369, no. 1948, pp. 3175–3197, 2011.
- [52] F. Hellman, A. Hoffmann, Y. Tserkovnyak, G. S. Beach, E. E. Fullerton, C. Leighton, A. H. MacDonald, D. C. Ralph, D. A. Arena, H. A. Dürr, *et al.*, “Interface-induced phenomena in magnetism,” *Reviews of modern physics*, vol. 89, no. 2, p. 025006, 2017.
- [53] A. Manchon, J. Železný, I. M. Miron, T. Jungwirth, J. Sinova, A. Thiaville, K. Garello, and P. Gambardella, “Current-induced spin-orbit torques in ferromagnetic and antiferromagnetic systems,” *Reviews of Modern Physics*, vol. 91, no. 3, p. 035004, 2019.
- [54] K. Ando, S. Takahashi, K. Harii, K. Sasage, J. Ieda, S. Maekawa, and E. Saitoh, “Electric manipulation of spin relaxation using the spin hall effect,” *Physical review letters*, vol. 101, no. 3, p. 036601, 2008.
- [55] V. E. Demidov, S. Urazhdin, H. Ulrichs, V. Tiberkevich, A. Slavin, D. Baither, G. Schmitz, and S. O. Demokritov, “Magnetic nano-oscillator driven by pure spin current,” *Nature materials*, vol. 11, no. 12, pp. 1028–1031, 2012.
- [56] Y. Kajiwara, K. Harii, S. Takahashi, J.-i. Ohe, K. Uchida, M. Mizuguchi, H. Umezawa, H. Kawai, K. Ando, K. Takanashi, *et al.*, “Transmission of electrical signals by spin-wave interconversion in a magnetic insulator,” *Nature*, vol. 464, no. 7286, pp. 262–266, 2010.
- [57] Z. Wang, Y. Sun, M. Wu, V. Tiberkevich, and A. Slavin, “Control of spin waves in a thin film ferromagnetic insulator through interfacial spin scattering,” *Physical review letters*, vol. 107, no. 14, p. 146602, 2011.
- [58] E. Padrón-Hernández, A. Azevedo, and S. Rezende, “Amplification of spin waves in yttrium iron garnet films through the spin hall effect,” *Applied Physics Letters*, vol. 99, no. 19, p. 192511, 2011.

- [59] V. Demidov, S. Urazhdin, A. Rinkevich, G. Reiss, and S. Demokritov, “Spin hall controlled magnonic microwaveguides,” *Applied Physics Letters*, vol. 104, no. 15, p. 152402, 2014.
- [60] T. Wimmer, M. Althammer, L. Liensberger, N. Vlietstra, S. Geprägs, M. Weiler, R. Gross, and H. Huebl, “Spin transport in a magnetic insulator with zero effective damping,” *Physical Review Letters*, vol. 123, no. 25, p. 257201, 2019.
- [61] L. Cornelissen, J. Liu, B. Van Wees, and R. Duine, “Spin-current-controlled modulation of the magnon spin conductance in a three-terminal magnon transistor,” *Physical review letters*, vol. 120, no. 9, p. 097702, 2018.
- [62] M. Collet, X. De Milly, O. d. Kelly, V. V. Naletov, R. Bernard, P. Bortolotti, J. B. Youssef, V. Demidov, S. Demokritov, J. Prieto, *et al.*, “Generation of coherent spin-wave modes in yttrium iron garnet microdisks by spin-orbit torque,” *Nature communications*, vol. 7, no. 1, pp. 1–8, 2016.
- [63] O. Gladil, M. Collet, K. Garcia-Hernandez, C. Cheng, S. Xavier, P. Bortolotti, V. Cros, Y. Henry, J.-V. Kim, A. Anane, *et al.*, “Spin wave amplification using the spin hall effect in permalloy/platinum bilayers,” *Applied Physics Letters*, vol. 108, no. 20, p. 202407, 2016.
- [64] L. Cornelissen, J. Liu, R. Duine, J. B. Youssef, and B. Van Wees, “Long-distance transport of magnon spin information in a magnetic insulator at room temperature,” *Nature Physics*, vol. 11, no. 12, pp. 1022–1026, 2015.
- [65] C. Zhang, Y. Pu, S. A. Manuilov, S. P. White, M. R. Page, E. C. Blomberg, D. V. Pelekhov, and P. C. Hammel, “Engineering the spectrum of dipole field-localized spin-wave modes to enable spin-torque antidamping,” *Physical Review Applied*, vol. 7, no. 5, p. 054019, 2017.
- [66] H. Fulara, M. Zahedinejad, R. Khymyn, M. Dvornik, S. Fukami, S. Kanai, H. Ohno, and J. Åkerman, “Giant voltage-controlled modulation of spin hall nano-oscillator damping,” *Nature communications*, vol. 11, no. 1, pp. 1–7, 2020.
- [67] H. Zhang, M. Ku, F. Casola, C. Du, T. van der Sar, M. Onbasli, C. Ross, Y. Tserkovnyak, A. Yacoby, and R. Walsworth, “Spin-torque oscillation in a magnetic insulator probed by a single-spin sensor,” *Physical Review B*, vol. 102, no. 2, p. 024404, 2020.

[68] V. Demidov, S. Urazhdin, G. De Loubens, O. Klein, V. Cros, A. Anane, and S. Demokritov, “Magnetization oscillations and waves driven by pure spin currents,” *Physics Reports*, vol. 673, pp. 1–31, 2017.

[69] T. Chen, R. K. Dumas, A. Eklund, P. K. Muduli, A. Houshang, A. A. Awad, P. Dürrenfeld, B. G. Malm, A. Rusu, and J. Åkerman, “Spin-torque and spin-hall nano-oscillators,” *Proceedings of the IEEE*, vol. 104, no. 10, pp. 1919–1945, 2016.

[70] M. Evelt, V. Demidov, V. Bessonov, S. Demokritov, J. Prieto, M. Muñoz, J. Ben Youssef, V. Naletov, G. De Loubens, O. Klein, *et al.*, “High-efficiency control of spin-wave propagation in ultra-thin yttrium iron garnet by the spin-orbit torque,” *Applied Physics Letters*, vol. 108, no. 17, p. 172406, 2016.

[71] V. Demidov, S. Urazhdin, A. Anane, V. Cros, and S. Demokritov, “Spin-orbit-torque magnonics,” *Journal of Applied Physics*, vol. 127, no. 17, p. 170901, 2020.

[72] A. Aharoni *et al.*, *Introduction to the Theory of Ferromagnetism*, vol. 109. Clarendon Press, 2000.

[73] J. Stöhr and H. C. Siegmann, “Magnetism,” *Solid-State Sciences. Springer, Berlin, Heidelberg*, vol. 5, 2006.

[74] T. L. Gilbert, “A phenomenological theory of damping in ferromagnetic materials,” *IEEE transactions on magnetics*, vol. 40, no. 6, pp. 3443–3449, 2004.

[75] A. Barman and J. Sinha, *Spin dynamics and damping in ferromagnetic thin films and nanostructures*, vol. 1. Springer, 2018.

[76] G. S. Abo, Y.-K. Hong, J. Park, J. Lee, W. Lee, and B.-C. Choi, “Definition of magnetic exchange length,” *IEEE Transactions on Magnetics*, vol. 49, no. 8, pp. 4937–4939, 2013.

[77] B. Kalinikos, “Excitation of propagating spin waves in ferromagnetic films,” in *IEE Proceedings H (Microwaves, Optics and Antennas)*, vol. 127, pp. 4–10, IET, 1980.

[78] B. Kalinikos and A. Slavin, “Theory of dipole-exchange spin wave spectrum for ferromagnetic films with mixed exchange boundary conditions,” *Journal of Physics C: Solid State Physics*, vol. 19, no. 35, p. 7013, 1986.

[79] B. Kalinikos, M. Kostylev, N. Kozhus, and A. Slavin, “The dipole-exchange spin wave spectrum for anisotropic ferromagnetic films with mixed exchange boundary conditions,” *Journal of Physics: Condensed Matter*, vol. 2, no. 49, p. 9861, 1990.

[80] J. Eshbach and R. Damon, “Surface magnetostatic modes and surface spin waves,” *Physical Review*, vol. 118, no. 5, p. 1208, 1960.

- [81] R. Joseph and E. Schlömann, “Demagnetizing field in nonellipsoidal bodies,” *Journal of Applied Physics*, vol. 36, no. 5, pp. 1579–1593, 1965.
- [82] S. O. Demokritov, *Spin wave confinement*. Pan Stanford Publishing, 2009.
- [83] C. Kittel and C.-y. Fong, *Quantum theory of solids*, vol. 5. Wiley New York, 1963.
- [84] L. D. Landau and E. M. Lifshitz, *Statistical Physics: Volume 5*, vol. 5. Elsevier, 2013.
- [85] S. N. Bose, “Plancks gesetz und lichtquantenhypothese,” 1924.
- [86] A. Einstein, “Quantentheorie des einatomigen idealen gases,” *SB Preuss. Akad. Wiss. phys.-math. Klasse*, 1924.
- [87] S. O. Demokritov, V. E. Demidov, O. Dzyapko, G. A. Melkov, A. A. Serga, B. Hillebrands, and A. N. Slavin, “Bose–einstein condensation of quasi-equilibrium magnons at room temperature under pumping,” *Nature*, vol. 443, no. 7110, pp. 430–433, 2006.
- [88] V. Demidov, O. Dzyapko, S. Demokritov, G. Melkov, and A. Slavin, “Observation of spontaneous coherence in bose–einstein condensate of magnons,” *Physical review letters*, vol. 100, no. 4, p. 047205, 2008.
- [89] V. Demidov, O. Dzyapko, S. Demokritov, G. Melkov, and A. Slavin, “Thermalization of a parametrically driven magnon gas leading to bose–einstein condensation,” *Physical review letters*, vol. 99, no. 3, p. 037205, 2007.
- [90] S. Demokritov, “Magnon bec at room temperature and its spatio-temporal dynamics,” *Journal of Experimental and Theoretical Physics*, vol. 131, no. 1, pp. 83–94, 2020.
- [91] V. Tiberkevich, I. Borisenko, P. Nowik-Boltyk, V. Demidov, A. Rinkevich, S. Demokritov, and A. Slavin, “Excitation of coherent second sound waves in a dense magnon gas,” *Scientific reports*, vol. 9, no. 1, pp. 1–9, 2019.
- [92] A. J. Kreil, A. Pomyalov, V. S. L’vov, H. Y. Musiienko-Shmarova, G. A. Melkov, A. A. Serga, and B. Hillebrands, “Josephson oscillations in a room-temperature bose–einstein magnon condensate,” *arXiv preprint arXiv:1911.07802*, 2019.
- [93] M. Schneider, T. Brächer, D. Breitbach, V. Lauer, P. Pirro, D. A. Bozhko, H. Y. Musiienko-Shmarova, B. Heinz, Q. Wang, T. Meyer, *et al.*, “Bose–einstein condensation of quasiparticles by rapid cooling,” *Nature Nanotechnology*, pp. 1–5, 2020.
- [94] D. A. Bozhko, A. A. Serga, P. Clausen, V. I. Vasyuchka, F. Heussner, G. A. Melkov, A. Pomyalov, V. S. L’vov, and B. Hillebrands, “Supercurrent in a room-temperature

bose-einstein magnon condensate,” *Nature Physics*, vol. 12, no. 11, pp. 1057–1062, 2016.

- [95] D. A. Bozhko, A. J. Kreil, H. Y. Musiienko-Shmarova, A. A. Serga, A. Pomyalov, V. S. L’vov, and B. Hillebrands, “Bogoliubov waves and distant transport of magnon condensate at room temperature,” *Nature communications*, vol. 10, no. 1, pp. 1–9, 2019.
- [96] A. A. Serga, V. S. Tiberkevich, C. W. Sandweg, V. I. Vasyuchka, D. A. Bozhko, A. V. Chumak, T. Neumann, B. Obry, G. A. Melkov, A. N. Slavin, *et al.*, “Bose-einstein condensation in an ultra-hot gas of pumped magnons,” *Nature communications*, vol. 5, no. 1, pp. 1–8, 2014.
- [97] A. M. Kosevich, B. Ivanov, and A. Kovalev, “Magnetic solitons,” *Physics Reports*, vol. 194, no. 3-4, pp. 117–238, 1990.
- [98] S. M. Rezende and F. M. de Aguiar, “Spin-wave instabilities, auto-oscillations, and chaos in yttrium-iron-garnet,” *Proceedings of the IEEE*, vol. 78, no. 6, pp. 893–908, 1990.
- [99] N. Bloembergen and R. Damon, “Relaxation effects in ferromagnetic resonance,” *Physical Review*, vol. 85, no. 4, p. 699, 1952.
- [100] N. Bloembergen and S. Wang, “Relaxation effects in para-and ferromagnetic resonance,” *Physical Review*, vol. 93, no. 1, p. 72, 1954.
- [101] H. Suhl, “The nonlinear behavior of ferrites at high microwave signal levels,” *Proceedings of the IRE*, vol. 44, no. 10, pp. 1270–1284, 1956.
- [102] H. Suhl, “The theory of ferromagnetic resonance at high signal powers,” *Journal of Physics and Chemistry of Solids*, vol. 1, no. 4, pp. 209–227, 1957.
- [103] C. Boone, J. Katine, J. Childress, V. Tiberkevich, A. Slavin, J. Zhu, X. Cheng, and I. Krivorotov, “Resonant nonlinear damping of quantized spin waves in ferromagnetic nanowires: A spin torque ferromagnetic resonance study,” *Physical review letters*, vol. 103, no. 16, p. 167601, 2009.
- [104] A. Y. Dobin and R. Victora, “Intrinsic nonlinear ferromagnetic relaxation in thin metallic films,” *Physical review letters*, vol. 90, no. 16, p. 167203, 2003.
- [105] I. Barsukov, H. Lee, A. Jara, Y.-J. Chen, A. Gonçalves, C. Sha, J. Katine, R. Arias, B. Ivanov, and I. Krivorotov, “Giant nonlinear damping in nanoscale ferromagnets,” *Science advances*, vol. 5, no. 10, p. eaav6943, 2019.

[106] V. E. Demidov, H. Ulrichs, S. O. Demokritov, and S. Urazhdin, “Nonlinear scattering in nanoscale magnetic elements: Overpopulation of the lowest-frequency magnon state,” *Physical Review B*, vol. 83, no. 2, p. 020404, 2011.

[107] G. Melkov, D. Slobodianiuk, V. Tiberkevich, G. De Loubens, O. Klein, and A. Slavin, “Nonlinear ferromagnetic resonance in nanostructures having discrete spectrum of spin-wave modes,” *IEEE Magnetics Letters*, vol. 4, pp. 4000504–4000504, 2013.

[108] H. G. Bauer, P. Majchrak, T. Kachel, C. H. Back, and G. Woltersdorf, “Nonlinear spin-wave excitations at low magnetic bias fields,” *Nature communications*, vol. 6, no. 1, pp. 1–7, 2015.

[109] B. A. McCullian, A. M. Thabt, B. A. Gray, A. L. Melendez, M. S. Wolf, V. L. Safonov, D. V. Pelekhov, V. P. Bhallamudi, M. R. Page, and P. C. Hammel, “Broadband multi-magnon relaxometry using a quantum spin sensor for high frequency ferromagnetic dynamics sensing,” *Nature communications*, vol. 11, no. 1, pp. 1–8, 2020.

[110] S. Maekawa, S. O. Valenzuela, T. Kimura, and E. Saitoh, *Spin current*. Oxford University Press, 2017.

[111] S. Huang, D. Qu, T. Chuang, C. Chiang, W. Lin, and C. Chien, “Pure spin current phenomena,” *Applied Physics Letters*, vol. 117, no. 19, p. 190501, 2020.

[112] J. Sinova, S. O. Valenzuela, J. Wunderlich, C. Back, and T. Jungwirth, “Spin hall effects,” *Reviews of Modern Physics*, vol. 87, no. 4, p. 1213, 2015.

[113] N. F. Mott, “The scattering of fast electrons by atomic nuclei,” *Proceedings of the Royal Society of London. Series A, Containing Papers of a Mathematical and Physical Character*, vol. 124, no. 794, pp. 425–442, 1929.

[114] M. I. D’Yakonov and V. Perel, “Possibility of orienting electron spins with current,” *JETPL*, vol. 13, p. 467, 1971.

[115] J. Hirsch, “Spin hall effect,” *Physical Review Letters*, vol. 83, no. 9, p. 1834, 1999.

[116] A. Hoffmann, “Spin hall effects in metals,” *IEEE transactions on magnetics*, vol. 49, no. 10, pp. 5172–5193, 2013.

[117] J. C. Slonczewski *et al.*, “Current-driven excitation of magnetic multilayers,” *Journal of Magnetism and Magnetic Materials*, vol. 159, no. 1, p. L1, 1996.

[118] A. Slavin and V. Tiberkevich, “Nonlinear auto-oscillator theory of microwave generation by spin-polarized current,” *IEEE Transactions on Magnetics*, vol. 45, no. 4, pp. 1875–1918, 2009.

- [119] A. Jenkins, “Self-oscillation,” *Physics Reports*, vol. 525, no. 2, pp. 167–222, 2013.
- [120] W. F. Brown Jr, “Thermal fluctuations of a single-domain particle,” *Physical review*, vol. 130, no. 5, p. 1677, 1963.
- [121] V. E. Demidov, S. Urazhdin, E. Edwards, M. D. Stiles, R. D. McMichael, and S. O. Demokritov, “Control of magnetic fluctuations by spin current,” *Physical review letters*, vol. 107, no. 10, p. 107204, 2011.
- [122] I. Borisenko, V. Demidov, S. Urazhdin, A. Rinkevich, and S. Demokritov, “Relation between unidirectional spin hall magnetoresistance and spin current-driven magnon generation,” *Applied Physics Letters*, vol. 113, no. 6, p. 062403, 2018.
- [123] V. Demidov, S. Urazhdin, A. Zholud, A. Sadovnikov, and S. Demokritov, “Nanoconstriction-based spin-hall nano-oscillator,” *Applied Physics Letters*, vol. 105, no. 17, p. 172410, 2014.
- [124] Z. Duan, A. Smith, L. Yang, B. Youngblood, J. Lindner, V. E. Demidov, S. O. Demokritov, and I. N. Krivorotov, “Nanowire spin torque oscillator driven by spin orbit torques,” *Nature communications*, vol. 5, no. 1, pp. 1–7, 2014.
- [125] N. Sato, K. Schultheiss, L. Körber, N. Puwenberg, T. Mühl, A. Awad, S. Arekapudi, O. Hellwig, J. Fassbender, and H. Schultheiss, “Domain wall based spin-hall nano-oscillators,” *Physical review letters*, vol. 123, no. 5, p. 057204, 2019.
- [126] K. Wagner, A. Smith, T. Hache, J.-R. Chen, L. Yang, E. Montoya, K. Schultheiss, J. Lindner, J. Fassbender, I. Krivorotov, *et al.*, “Injection locking of multiple auto-oscillation modes in a tapered nanowire spin hall oscillator,” *Scientific reports*, vol. 8, no. 1, pp. 1–9, 2018.
- [127] M. Evelt, C. Safranski, M. Aldosary, V. Demidov, I. Barsukov, A. Nosov, A. Rinkevich, K. Sobotkiewich, X. Li, J. Shi, *et al.*, “Spin hall-induced auto-oscillations in ultrathin yig grown on pt,” *Scientific reports*, vol. 8, no. 1, pp. 1–7, 2018.
- [128] T. Hache, Y. Li, T. Weinhold, B. Scheumann, F. Gonçalves, O. Hellwig, J. Fassbender, and H. Schultheiss, “Bipolar spin hall nano-oscillators,” *Applied Physics Letters*, vol. 116, no. 19, p. 192405, 2020.
- [129] R. Cheng, D. Xiao, and A. Brataas, “Terahertz antiferromagnetic spin hall nano-oscillator,” *Physical Review Letters*, vol. 116, no. 20, p. 207603, 2016.

- [130] O. Sulymenko, O. Prokopenko, V. Tiberkevich, A. Slavin, B. Ivanov, and R. Khymyn, “Thz-frequency spin-hall auto-oscillator based on a canted antiferromagnet,” *arXiv preprint arXiv:1707.07491*, 2017.
- [131] R. Khymyn, I. Lisenkov, V. Tiberkevich, B. A. Ivanov, and A. Slavin, “Antiferromagnetic thz-frequency josephson-like oscillator driven by spin current,” *Scientific reports*, vol. 7, p. 43705, 2017.
- [132] P. Dürrenfeld, A. A. Awad, A. Houshang, R. K. Dumas, and J. Åkerman, “A 20 nm spin hall nano-oscillator,” *Nanoscale*, vol. 9, no. 3, pp. 1285–1291, 2017.
- [133] R. Liu, W. Lim, and S. Urazhdin, “Spectral characteristics of the microwave emission by the spin hall nano-oscillator,” *Physical review letters*, vol. 110, no. 14, p. 147601, 2013.
- [134] A. Zholud and S. Urazhdin, “Microwave generation by spin hall nanooscillators with nanopatterned spin injector,” *Applied Physics Letters*, vol. 105, no. 11, p. 112404, 2014.
- [135] A. Awad, P. Dürrenfeld, A. Houshang, M. Dvornik, E. Iacocca, R. Dumas, and J. Åkerman, “Long-range mutual synchronization of spin hall nano-oscillators,” *Nature Physics*, vol. 13, no. 3, pp. 292–299, 2017.
- [136] M. Zahedinejad, H. Mazraati, H. Fulara, J. Yue, S. Jiang, A. Awad, and J. Åkerman, “Cmos compatible w/cofeb/mgo spin hall nano-oscillators with wide frequency tunability,” *Applied Physics Letters*, vol. 112, no. 13, p. 132404, 2018.
- [137] M. Zahedinejad, A. A. Awad, S. Muralidhar, R. Khymyn, H. Fulara, H. Mazraati, M. Dvornik, and J. Åkerman, “Two-dimensional mutually synchronized spin hall nano-oscillator arrays for neuromorphic computing,” *Nature Nanotechnology*, vol. 15, no. 1, pp. 47–52, 2020.
- [138] A. Houshang, M. Zahedinejad, S. Muralidhar, J. Checinski, A. A. Awad, and J. Åkerman, “A spin hall ising machine,” *arXiv preprint arXiv:2006.02236*, 2020.
- [139] R. Lowde, “Spin waves and neutron scattering,” *Journal of Applied Physics*, vol. 36, no. 3, pp. 884–892, 1965.
- [140] J. McCord, “Progress in magnetic domain observation by advanced magneto-optical microscopy,” *Journal of Physics D: Applied Physics*, vol. 48, no. 33, p. 333001, 2015.
- [141] S. Wintz, V. Tiberkevich, M. Weigand, J. Raabe, J. Lindner, A. Erbe, A. Slavin, and J. Fassbender, “Magnetic vortex cores as tunable spin-wave emitters,” *Nature nanotechnology*, vol. 11, no. 11, pp. 948–953, 2016.

- [142] F. Casola, T. van der Sar, and A. Yacoby, “Probing condensed matter physics with magnetometry based on nitrogen-vacancy centres in diamond,” *Nature Reviews Materials*, vol. 3, no. 1, pp. 1–13, 2018.
- [143] A. Borovik-Romanov and N. M. Kreines, “Brillouin-mandelstam scattering from thermal and excited magnons,” *Physics Reports*, vol. 81, no. 5, pp. 351–408, 1982.
- [144] M. G. Cottam and D. J. Lockwood, *Light scattering in magnetic solids*. Wiley New York, 1986.
- [145] S. Demokritov and E. Tsymbal, “Light scattering from spin waves in thin films and layered systems,” *Journal of Physics: Condensed Matter*, vol. 6, no. 36, p. 7145, 1994.
- [146] J. Sandercock and W. Wettling, “Light scattering from thermal acoustic magnons in yttrium iron garnet,” *Solid State Communications*, vol. 13, no. 10, pp. 1729–1732, 1973.
- [147] J. Sandercock, “Trends in brillouin scattering: studies of opaque materials, supported films, and central modes,” in *Light scattering in solids III*, pp. 173–206, Springer, 1982.
- [148] S. O. Demokritov and V. E. Demidov, “Micro-brillouin light scattering spectroscopy of magnetic nanostructures,” *IEEE transactions on magnetics*, vol. 44, no. 1, pp. 6–12, 2007.
- [149] T. Sebastian, K. Schultheiss, B. Obry, B. Hillebrands, and H. Schultheiss, “Micro-focused brillouin light scattering: imaging spin waves at the nanoscale,” *Frontiers in Physics*, vol. 3, p. 35, 2015.
- [150] M. Madami, G. Gubbiotti, S. Tacchi, and G. Carlotti, “Application of microfocused brillouin light scattering to the study of spin waves in low-dimensional magnetic systems,” in *Solid state physics*, vol. 63, pp. 79–150, Elsevier, 2012.
- [151] R. Freeman, R. Lemasters, T. Kalejaiye, F. Wang, G. Chen, J. Ding, M. Wu, V. E. Demidov, S. O. Demokritov, H. Harutyunyan, *et al.*, “Brillouin light scattering of spin waves inaccessible with free-space light,” *arXiv preprint arXiv:2004.05314*, 2020.
- [152] J. Fidler and T. Schrefl, “Micromagnetic modelling-the current state of the art,” *Journal of Physics D: Applied Physics*, vol. 33, no. 15, p. R135, 2000.
- [153] D. Kumar and A. Adeyeye, “Techniques in micromagnetic simulation and analysis,” *Journal of Physics D: Applied Physics*, vol. 50, no. 34, p. 343001, 2017.
- [154] C. Abert, “Micromagnetics and spintronics: models and numerical methods,” *The European Physical Journal B*, vol. 92, no. 6, p. 120, 2019.

- [155] A. Vansteenkiste, J. Leliaert, M. Dvornik, M. Helsen, F. Garcia-Sanchez, and B. Van Waeyenberge, “The design and verification of mumax3,” *AIP advances*, vol. 4, no. 10, p. 107133, 2014.
- [156] L. Berger, “Emission of spin waves by a magnetic multilayer traversed by a current,” *Physical Review B*, vol. 54, no. 13, p. 9353, 1996.
- [157] S. A. Bender, R. A. Duine, and Y. Tserkovnyak, “Electronic pumping of quasiequilibrium bose-einstein-condensed magnons,” *Physical review letters*, vol. 108, no. 24, p. 246601, 2012.
- [158] S. A. Bender, R. A. Duine, A. Brataas, and Y. Tserkovnyak, “Dynamic phase diagram of dc-pumped magnon condensates,” *Physical Review B*, vol. 90, no. 9, p. 094409, 2014.
- [159] R. Duine, A. Brataas, S. A. Bender, and Y. Tserkovnyak, “Spintronics and magnon bose-einstein condensation,” *arXiv preprint arXiv:1505.01329*, 2015.
- [160] A. Slavin and V. Tiberkevich, “Spin wave mode excited by spin-polarized current in a magnetic nanocontact is a standing self-localized wave bullet,” *Physical review letters*, vol. 95, no. 23, p. 237201, 2005.
- [161] O. Sulymenko, O. Prokopenko, V. Tyberkevych, A. Slavin, and A. Serga, “Bullets and droplets: Two-dimensional spin-wave solitons in modern magnonics,” *Low Temperature Physics*, vol. 44, no. 7, pp. 602–617, 2018.
- [162] M. Andrews, C. Townsend, H.-J. Miesner, D. Durfee, D. Kurn, and W. Ketterle, “Observation of interference between two bose condensates,” *Science*, vol. 275, no. 5300, pp. 637–641, 1997.
- [163] P. Nowik-Boltyk, O. Dzyapko, V. Demidov, N. Berloff, and S. Demokritov, “Spatially non-uniform ground state and quantized vortices in a two-component bose-einstein condensate of magnons,” *Scientific reports*, vol. 2, p. 482, 2012.
- [164] H. Ulrichs, V. Demidov, and S. Demokritov, “Micromagnetic study of auto-oscillation modes in spin-hall nano-oscillators,” *Applied Physics Letters*, vol. 104, no. 4, p. 042407, 2014.
- [165] R. K. Dumas, E. Iacocca, S. Bonetti, S. Sani, S. M. Mohseni, A. Eklund, J. Persson, O. Heinonen, and J. Åkerman, “Spin-wave-mode coexistence on the nanoscale: a consequence of the oersted-field-induced asymmetric energy landscape,” *Physical review letters*, vol. 110, no. 25, p. 257202, 2013.

- [166] S. Bonetti, V. Tiberkevich, G. Consolo, G. Finocchio, P. Muduli, F. Mancoff, A. Slavin, and J. Åkerman, “Experimental evidence of self-localized and propagating spin wave modes in obliquely magnetized current-driven nanocontacts,” *Physical review letters*, vol. 105, no. 21, p. 217204, 2010.
- [167] B. Dieny and M. Chshiev, “Perpendicular magnetic anisotropy at transition metal/oxide interfaces and applications,” *Reviews of Modern Physics*, vol. 89, no. 2, p. 025008, 2017.
- [168] M. Hoefer, T. J. Silva, and M. W. Keller, “Theory for a dissipative droplet soliton excited by a spin torque nanocontact,” *Physical Review B*, vol. 82, no. 5, p. 054432, 2010.
- [169] S. M. Mohseni, S. Sani, J. Persson, T. A. Nguyen, S. Chung, Y. Pogoryelov, P. Muduli, E. Iacocca, A. Eklund, R. Dumas, *et al.*, “Spin torque-generated magnetic droplet solitons,” *Science*, vol. 339, no. 6125, pp. 1295–1298, 2013.
- [170] F. Macià and A. D. Kent, “Magnetic droplet solitons,” *Journal of Applied Physics*, vol. 128, no. 10, p. 100901, 2020.
- [171] E. Iacocca, R. K. Dumas, L. Bookman, M. Mohseni, S. Chung, M. A. Hoefer, and J. Åkerman, “Confined dissipative droplet solitons in spin-valve nanowires with perpendicular magnetic anisotropy,” *Physical Review Letters*, vol. 112, no. 4, p. 047201, 2014.
- [172] A. Khvalkovskiy, V. Cros, D. Apalkov, V. Nikitin, M. Krounbi, K. Zvezdin, A. Anane, J. Grollier, and A. Fert, “Matching domain-wall configuration and spin-orbit torques for efficient domain-wall motion,” *Physical Review B*, vol. 87, no. 2, p. 020402, 2013.
- [173] S. Emori, U. Bauer, S.-M. Ahn, E. Martinez, and G. S. Beach, “Current-driven dynamics of chiral ferromagnetic domain walls,” *Nature materials*, vol. 12, no. 7, pp. 611–616, 2013.
- [174] W. Jiang, P. Upadhyaya, W. Zhang, G. Yu, M. B. Jungfleisch, F. Y. Fradin, J. E. Pearson, Y. Tserkovnyak, K. L. Wang, O. Heinonen, *et al.*, “Blowing magnetic skyrmion bubbles,” *Science*, vol. 349, no. 6245, pp. 283–286, 2015.
- [175] S. Bonetti, R. Kukreja, Z. Chen, F. Macià, J. Hernàndez, A. Eklund, D. Backes, J. Frisch, J. Katine, G. Malm, *et al.*, “Direct observation and imaging of a spin-wave soliton with p-like symmetry,” *Nature communications*, vol. 6, no. 1, pp. 1–6, 2015.

- [176] V. Demidov, S. Urazhdin, B. Divinskiy, A. Rinkevich, and S. Demokritov, “Spectral linewidth of spin-current nano-oscillators driven by nonlocal spin injection,” *Applied Physics Letters*, vol. 107, no. 20, p. 202402, 2015.
- [177] A. Brataas, B. van Wees, O. Klein, G. de Loubens, and M. Viret, “Spin insultronics,” *Physics Reports*, 2020.
- [178] V. E. Demidov, S. Urazhdin, R. Liu, B. Divinskiy, A. Telegin, and S. O. Demokritov, “Excitation of coherent propagating spin waves by pure spin currents,” *Nature communications*, vol. 7, no. 1, pp. 1–6, 2016.
- [179] V. Demidov, H. Ulrichs, S. Gurevich, S. Demokritov, V. Tiberkevich, A. Slavin, A. Zholud, and S. Urazhdin, “Synchronization of spin hall nano-oscillators to external microwave signals,” *Nature communications*, vol. 5, no. 1, pp. 1–6, 2014.
- [180] T. Kendziorczyk, S. Demokritov, and T. Kuhn, “Spin-wave-mediated mutual synchronization of spin-torque nano-oscillators: A micromagnetic study of multistable phase locking,” *Physical Review B*, vol. 90, no. 5, p. 054414, 2014.
- [181] A. Houshang, E. Iacocca, P. Dürrenfeld, S. R. Sani, J. Åkerman, and R. K. Dumas, “Spin-wave-beam driven synchronization of nanocontact spin-torque oscillators,” *Nature nanotechnology*, vol. 11, no. 3, pp. 280–286, 2016.
- [182] T. Kendziorczyk and T. Kuhn, “Mutual synchronization of nanoconstriction-based spin hall nano-oscillators through evanescent and propagating spin waves,” *Physical Review B*, vol. 93, no. 13, p. 134413, 2016.

List of publications

Publications included in this thesis:

1. **B. Divinskiy**, S. Urazhdin, S. O. Demokritov, and V. E. Demidov, "Controlled non-linear magnetic damping in spin-Hall nano-devices", *Nature Communications* 10, 5211 (2019).
2. **B. Divinskiy**, V. E. Demidov, S. Urazhdin, R. Freeman, A. B. Rinkevich, and S. O. Demokritov, "Controllable excitation of quasi-linear and bullet modes in a spin-Hall nano-oscillator", *Applied Physics Letters* 114, 042403 (2019).
3. **B. Divinskiy**, V. E. Demidov, S. Urazhdin, R. Freeman, A. B. Rinkevich, and S. O. Demokritov, "Excitation and amplification of spin waves by spin-orbit torque", *Advanced Materials* 30, 1802837 (2018).
4. **B. Divinskiy**, S. Urazhdin, V. E. Demidov, A. Kozhanov, A. P. Nosov, A. B. Rinkevich, and S. O. Demokritov, "Magnetic droplet solitons generated by pure spin currents", *Physical Review B* 96, 224419 (2017).
5. **B. Divinskiy**, V. E. Demidov, A. Kozhanov, A. B. Rinkevich, S. O. Demokritov, and S. Urazhdin, "Nanoconstriction spin-Hall oscillator with perpendicular magnetic anisotropy", *Applied Physics Letters* 111, 032405 (2017).
6. V. E. Demidov, S. Urazhdin, **B. Divinskiy**, V. D. Bessonov, A. B. Rinkevich, V. V. Ustinov, and S. O. Demokritov, "Chemical potential of quasi-equilibrium magnon gas driven by pure spin current", *Nature Communications* 8, 1579 (2017).

Publications related to, but not included in this thesis:

7. **B. Divinskiy**, G. Chen, S. Urazhdin, S. O. Demokritov, and V. E. Demidov, "Effects of spin-orbit torque on the ferromagnetic and exchange spin-wave modes in ferrimagnetic Co-Gd alloy", *Physical Review Applied* 14, 044016 (2020).
8. I. V. Borisenko, **B. Divinskiy**, V. E. Demidov, G. Li, T. Nattermann, V. L. Pokrovsky, and S. O. Demokritov, "Direct evidence of spatial stability of Bose-Einstein condensate of magnons", *Nature Communications* 11, 1691 (2020).
9. **B. Divinskiy**, N. Thiery, L. Viva, O. Klein, N. Beaulieu, J. Ben Youssef, S. O. Demokritov, and V. E. Demidov, "Sub-micrometer near-field focusing of spin waves in ultrathin YIG films", *Applied Physics Letters* 116, 062401 (2020).

10. N. Thiery, V. V. Naletov, L. Vila, A. Marty, A. Brenac, J.-F. Jacquot, G. de Loubens, M. Viret, A. Anane, V. Cros, J. Ben Youssef, N. Beaulieu, V. E. Demidov, **B. Divinskiy**, S. O. Demokritov, and O. Klein, "Electrical properties of epitaxial yttrium iron garnet ultrathin films at high temperatures", *Physical Review B* 97, 064422 (2018).
11. **B. Divinskiy**, V. E. Demidov, S. O. Demokritov, A. B. Rinkevich, and S. Urazhdin, "Route toward high-speed nano-magnonics provided by pure spin currents", *Applied Physics Letters* 109, 252401 (2016).
12. S. Urazhdin, V. E. Demidov, R. Cao, **B. Divinskiy**, V. Tyberkevych, A. Slavin, A. B. Rinkevich, and S. O. Demokritov, "Mutual synchronization of nano-oscillators driven by pure spin current", *Applied Physics Letters* 109, 162402 (2016).
13. V. E. Demidov, S. Urazhdin, R. Liu, **B. Divinskiy**, A. Telegin, and S. O. Demokritov, "Excitation of coherent propagating spin waves by pure spin currents", *Nature Communications* 7, 10446 (2016).
14. V. E. Demidov, S. Urazhdin, **B. Divinskiy**, A. B. Rinkevich, and S. O. Demokritov, "Spectral linewidth of spin-current nano-oscillators driven by nonlocal spin injection", *Applied Physics Letters* 107, 202402 (2015).

Publications not related to this thesis:

15. N. A. Volkov, **B. Divinskiy**, P. N. Vorontsov-Velyaminov, and A. K. Shchekin, "Diffusivities of species in ionic micellar solutions: Molecular dynamic simulation", *Colloids and Surfaces A* 480, 165-170 (2015).
16. E. V. Aksanova, **B. Divinskiy**, A. A. Karetnikov, N. A. Karetnikov, A. P. Kovshik, E. V. Kryukov, and V. P. Romanov, "Peculiarities of light propagation in chiral liquid crystal cells in an external electric field", *Journal of Experimental and Theoretical Physics* 118, 323–332 (2014).

Acknowledgments

Throughout the thesis, I, Boris Divinskiy, used the pronoun "we", and this was not accidental. None of the results presented here could have been obtained without the help of very special people in my life to whom I would like to express my sincere gratitude.

I would like to thank my scientific supervisor Prof. Dr. Sergej O. Demokritov for general guidance and always very helpful feedback on my work. Sergej's remarkable physical intuition, breadth of knowledge and graciousness make him a truly great advisor, and it was a real privilege for me to work in his group.

I am very grateful to my day-to-day supervisor, Dr. Vladislav E. Demidov, for mentoring me over the past years. Countless hours of our discussions have largely shaped me both personally and professionally. I deeply appreciate the amount of time and energy that Vlad has spent helping me in and outside the lab, as well as his endless patience in answering my, most of the time, not the brightest questions. Vlad's troubleshooting skills and strong work ethic never cease to amaze me, and I am very fortunate to be his "apprentice".

I would like to thank Prof. Dr. Sergei Urazhdin from Emory University, who fabricated all the samples studied in this thesis. I am thankful to Sergei not only for the excellent quality of the samples, but also for his enthusiasm and creative approach to doing physics, which greatly influenced me.

I am infinitely grateful to my parents, sister and grandparents for all the years of encouragement and love. I am also very thankful to the "Dodelido family" for their kindness and support during my stay in Germany. Finally, I would like to sincerely thank Zhops for all the special and non-special sandwiches and the rest of the "Münchezhops family" for all the good times we have spent together. Zenok.

Lebenslauf

Name: Boris Divinskiy
Geburtsdatum: 17.01.1994
Geburtsort: Gelendschik, Russland
Staatsangehörigkeit: russisch

Schulausbildung:

09/2000 - 06/2010 Schule №5, Gelendschik, Russland

Studium:

09/2010 - 07/2014 Studium der Physik an der Staatliche Universität
Sankt Petersburg, Russland (Bachelor)
10/2014 - 08/2016 Studium der Physik an der WWU Münster (Master)

Promotionsstudium:

10/2016 Beginn der Dissertation am Institut für Angewandte Physik
unter der Betreuung von Prof. Dr. Sergej O. Demokritov.
Während dieser Zeit als wissenschaftlicher Mitarbeiter dort angestellt.

